Setup and Operation of a Spectroscopic Imaging STM for the Study of Iron-Based Superconductors

THÈSE N^{O} 5948 (2014)

PRÉSENTÉE LE 12 FÉVRIER 2014
À LA FACULTÉ DES SCIENCES DE BASE
LABORATOIRE DE SCIENCE À L'ÉCHELLE NANOMÉTRIQUE
PROGRAMME DOCTORAL EN PHYSIQUE

ÉCOLE POLYTECHNIQUE FÉDÉRALE DE LAUSANNE

POUR L'OBTENTION DU GRADE DE DOCTEUR ÈS SCIENCES

PAR

Seth Cullen WHITE

acceptée sur proposition du jury:

Prof. N. Grandjean, président du jury
Prof. K. Kern, directeur de thèse
Prof. F. Baumberger, rapporteur
Prof. D. Pavuna, rapporteur
Prof. W. Wulfhekel, rapporteur

ÉCOLE POLYTECHNIQUE
FÉDÉRALE DE LAUSANNE

Suisse
2014

Therefore he seems to me a very foolish man, and truly wretched, who will not increase his understanding while he is in the world, and ever wish and long to reach that endless life where all shall be made clear.

- Ælfred Æþelwulfsson, Anglorum Saxonum rex (*849-†899)

Abstract

The field of high temperature superconductivity promises many future technological applications, including, ultimately, major improvements to world energy infrastructure – just what is needed at a time of global energy insecurity. However, despite having been studied for years in the cuprates, high T_c superconductivity remains an unsolved problem. Against a backdrop of decelerating progress in the field, the recent discovery of high T_c superconductivity in iron-based compounds has helped to renew a sense of hope for the future.

Prior to its discovery, superconductivity in iron-based compounds seemed unintuitive due to the strong association of Fe with magnetism. Indeed, compared with superconductivity in previously known materials, iron-based superconductivity appears to be fundamentally different – and likely has a different origin. For example, experimental evidence suggests that the order parameter in iron-based superconductors is neither s-wave, as in conventional superconductors, nor d-wave, as in the cuprates. The pairing mechanism in the iron-based superconductors, which is certainly unconventional, is believed to be related to magnetism.

In this work, I use the scanning tunneling microscopy (STM) technique known as spectroscopic imaging (SI-STM) to investigate the iron-based superconductors. SI-STM, which involves the recording of tunneling spectroscopy (STS) data as a function of position, is a powerful tool in solid state physics. It can be used to measure electronic structure in both real and reciprocal space, and provides a higher energy resolution than is achievable with angle-resolved photoemission spectroscopy (ARPES). However, as a surface technique, distinguishing bulk properties from surface effects can be a challenge.

In order to perform the experiments, a scanning tunneling microscope with a sapphire measurement head was constructed. The instrument has been optimized for maximum stability at low temperatures and in high magnetic fields by choice of material. In the body of this work, I begin by describing the construction of the instrument and continue by presenting several studies of the iron-based superconductor families $Fe_{1+\delta}Te_xSe_{1-x}$ and $Ba_xK_{1-x}Fe_2As_2$. In the first study, the role of monoatomic Fe impurities in one material family is reviewed and found to be significant. In the second study, the origin, prevalence and role of nanoscale electronic / superconducting inhomogeneity, and possible correlations with chemical inhomogeneity, are discussed for both compound families. In the third study, evidence is presented which suggests the existence of a nematic electronic state in multiple materials, representing a C4 → C2 symmetry breaking in the nominal absence of a corresponding structural symmetry breaking. In the last study, the formation and behavior of Abrikosov vortices is investigated in one material.

Keywords: *scanning tunneling microscopy, spectroscopic imaging, sapphire, low temperature, high magnetic field, unconventional superconductivity, iron-based superconductors*

Zusammenfassung

Die Hochtemperatursupraleitung verspricht viele neue technologischen Anwendungen, letztlich auch bedeutende Verbesserungen der Weltenergieinfrastruktur – just das was in einer Zeit globaler Energieunsicherheit hilfreich wäre. Doch, trotz jahrelange Erforschung der Kupraten bleibt das Problem der Hochtemperatursupraleitung weiterhin ungelöst. Vor dem Hintergrund eher langsames Fortschritts hat die jüngste Entdeckung der Hochtemperatursupraleitung in eisenbasierten Materialien dazu beigetragen, eine Hoffnung für die Zukunft zu erneuern. Vor seiner Entdeckung war Supraleitung in eisenbasierten Materialien auf Grund der Assoziation Eisens mit dem Magnetismus nicht intuitiv. Gewiss, verglichen mit der Supraleitung in anderen bekannten Materialien scheint die eisenbasierte Supraleitung grundlegend anderes zu sein – und hat vermutlich auch einen anderen Ursprung. Zum Beispiel, experimentelle Befunde liegen nahe, dass der Ordnungsparameter weder konventionell s-Welle sei, noch, wie im Falle der Kupraten, d-Welle. Der Paarungsmechanismus, der sicher unkonvenionell ist, wird vermutet mit dem Magnetismus in Verbindung zu stehen.
In dieser Arbeit verwende ich eine Technik der Rastertunnelmikroskopie (STM), die spektroskopische Kartographie (SI-STM), um die eisenbasierten Supraleitern zu erforschen. SI-STM, welches das Aufnehmen tunnelspektroskopische (STS) Daten mit einer räumlichen Auflösung beinhaltet, ist ein mächtiges Werkzeug der Festkörperphysik. Es kann verwendet werden um elektronische Struktur sowohl im realen als auch im reziproken Raum aufzunehmen, und hat eine höhere energetische Auflösung als winkelaufgelöster Photoelektronenspektroskopie (ARPES). Als Oberflächenmethode kann es allerdings auch herausfordernd sein, interne Eigenschaften der Probe von Oberflächeneffekten zu unterscheiden.
Um die Durchführung der Experimente zu ermöglichen ist ein Rastertunnelmikroskop mit einem Meßkopf aus Saphir gebaut worden. Das Instrument ist optimiert worden durch die Materialauswahl für maximale Stabilität bei tiefen Temperaturen und unter hohem magnetischen Feld. Im Hauptteil dieser Arbeit werde ich mit einer Beschreibung des gebauten Instrumentes anfangen, und fortfahren mit der Vorstellung einiger Studien der eisenbasierten Supraleiterfamilien $Fe_{1+\delta}Te_xSe_{1-x}$ und $Ba_xK_{1-x}Fe_2As_2$. In der ersten Studie wird die Rolle atomarischer Fe Defekte in einem eisenbasierten Supraleiter untersucht und für signifikant befunden. In der zweiten Studie werden der Ursprung, die Verbreitung und die Rolle nanoskaliger Inhomogenitäten der elektronischen Anregungen und der Supraleitung, und

mögliche Korrelationen mit chemischen Inhomogenitäten, erkundet. In der dritten Studie werden Hinweise in mehreren Materialien gefunden, die die Existenz eines nematischen Zustandes suggerieren. Die beschriebene elektronische Nematizität zeichnet sich durch eine elektronische C4 → C2 Symmetriebrechung aus, im nominalen Fehlen einer entsprechenden strukturellen Symmetriebrechung. In der letzten Studie werden die Evolution und das Verhalten von Abrikosovvortices in eisenbasierten Supraleitern erforscht.

Stichworte: *Rastertunnelmikroskopie, spektroskopische Kartographie, Saphir, tieftemperatur, hochfeld, unkonventionelle Supraleitung, eisenbasierte Supraleiter*

Contents

Chapter 1

Introduction

The quantum mechanical state known as superconductivity has captivated the physics community for more than a century. Though our understanding of this remarkable phenomenon remains incomplete, significant progress has been made over the years in its scientific characterization. At times, breakthroughs have been achieved, but for the most part knowledge has accumulated slowly and through the combined efforts of many contributors. By now, progress in this field has resulted in the development of a multitude of novel technologies. In contemporary experimental science, for example, there are now many applications which require or benefit from superconducting components – especially superconducting magnets – including particle accelerators, particle detectors, and high-resolution instruments such as the superconducting quantum interference device (SQUID) magnetometer. Perhaps the most important technologies are those which have been adopted into medical practice, such as magnetic resonance imaging (MRI), which represents a potentially life-saving diagnostic tool. Outside of scientific, unlimited budget, or niche applications, however, adoption has been slower. For example, in the transportation sector there is a glamorous technology which has long been a proven concept but which has not yet been widely implemented: the maglev train. Although uneconomical with normal conducting technology, the use of superconducting magnets could lead to massively reduced costs and the rapid adoption of this concept.

In the past, technological and scientific progress in the field of superconductivity has been driven in large part by the discovery, at regular intervals, of new superconducting materials. This can be seen in the historical trend, plotted in fig. 1.1, of highest known transition temperature (T_c) over time. Specifically, for the first sixty-odd years after the initial discovery of superconductivity in mercury, the highest known T_c increased in a near-linear fashion, at an average rate of about 0.4K per year. (Of course, from a technological point of view it is important to note that increases were not limited to T_c, but that other important parameters

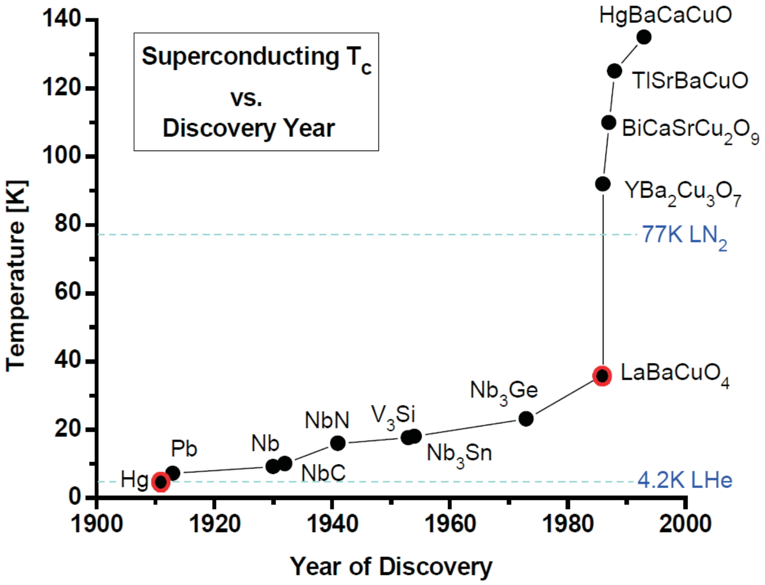

Figure 1.1: [1] Highest known T_c over time. Nobel prizes were awarded for the discoveries of superconductivity in Hg [2] (Heike Kamerlingh Onnes, 1913) and $LaBaCuO_4$ [3] (Johannes Bednorz and Karl Müller, 1987).

such as critical field and critical current density were increasing as well.) Clearly though, the still very low transition temperatures and impracticality of refrigeration technology were preventing the adoption of superconductivity in a large number of highly beneficial applications. Finally, in the mid 1980s, a major step was taken towards the overcoming of this problem with the discovery of the so-called high T_c superconductors. In just a few years after this discovery, materials were found which increased the highest known T_c by more than a factor of 3. Importantly, some of these high T_c "cuprate" superconductors had transition temperatures which exceeded the $\sim$ 77K boiling point of liquid nitrogen, which is much more economical and convenient to work with than the lower temperature liquid helium. However, superconductivity in these compounds remains poorly understood. As a consequence, finding new high T_c superconductors has been no easy task and, in the more than two decades since their discovery, no new materials have been found which would challenge the records set by the cuprates.

Nevertheless, progress has been made despite the mostly blind nature of the search. Most spectacularly, high T_c superconductivity has recently been discovered in layered iron-based materials. Although the transition temperatures of the so-called iron-based superconductors are not nearly as high as those of the cuprates, they are nevertheless significantly higher than would be expected for conventional (i.e., electron-phonon coupling driven) superconductors of similar composition. Strong similarities of the phase diagram of the iron-based superconductors with that of the cuprates suggest that a better understanding of the one class of materials will help in understanding the other. It may be hoped, therefore, that a more in-depth understanding of unconventional, high T_c superconductivity in iron-based materials will lead eventually to a predictive theory of high T_c generally, and ultimately to the discovery of more superconductors with technologically useful properties. The vision, finding an economic material with a T_c above room temperature, would lead to vastly improved efficiencies in the generation, transportation, and distribution of electrical power, effecting a paradigm shift in our society.

With this work then, I wish to contribute towards a future with widespread and economical superconductivity by presenting a study of several recently discovered iron-based superconductors. Like the cuprates, the iron-based superconductors are layered, but in contrast show significantly less electronic anisotropy. The parent compounds of the iron-based superconductors are metallic, unlike the parent compounds of the cuprates, which are antiferromagnetic Mott insulators. The smaller anisotropy and metallic properties of the parent compounds of the iron-based superconductors suggest that they may be better suited for practical applications such as wire production than the cuprates. As a material class, I would argue that the iron-based superconductors are well-suited for investigation with scanning tunneling microscopy (STM), especially when used in conjunction with scanning tunneling spectroscopy (STS). For one thing, as non-stoichiometric and spatially inhomogenous materials, the investigation of the iron-based superconductors can clearly benefit from a spatially resolved technique. Further reasons include their complex, anisotropic and inhomogeneous electronic structure, their scissile layered crystal structure, and in some cases non-polar cleaved surface.

With the technique known as spectroscopic imaging STM (SI-STM), data can be taken in both real and reciprical space simultaneously. In STS, the local density of states (LDOS) of a material can be imaged by measuring the differential tunneling conductance (dI/dV). In SI-STM, an STS spectrum is taken at each pixel of an STM image, resulting in a map of the LDOS over the entire field of view ($g(\mathbf{r}, E)$). After collecting STS data with sufficiently high spatial and energy resolution, one can reconstruct many aspects of the material's electronic structure. In this way, SI-STM can be used, for example, to correlate nanoscopic topographic features with various electronic features, or to directly measure electronic inhomogeneity. Indirectly, SI-STM allows for the imaging of quasiparticle interference patterns, from which dominant scattering vectors can be extracted. This is done via analysis of the Fourier components of constant energy cuts (layers) in a spectroscopic map. Through comparison with theoretical models, scattering vectors can ultimately reveal deeper information about the symmetry of the pairing wave function and the origin of superconductivity in the material. In comparison to standard STM techniques, SI-STM has high stability requirements, but is also among the more powerful analytical tools available in condensed matter physics, particularly for the investigation of materials with unusual electronic structure such as strongly correlated materials. Also, SI-STM has several (potential) advantages over its main competitor, angle-resolved photoemission spectroscopy (ARPES), such as higher energy resolution (resulting from operation at lower temperatures), a much higher spatial resolution, the ability to measure unoccupied states, and the ability to operate in a magnetic field.

In the years since the discovery of the iron-based superconductors, STM and SI-STM studies by groups around the world have already helped achieve meaningful progress in their characterization. For example, complex, anisotropic pairing symmetry has been demonstrated with phase-sensitive quasiparticle interference (QPI) imaging and low temperature STS measurements, showing for instance that pairing symmetry can vary from nodal to nodeless $s_{\pm}$-wave within a single family, the iron chalcogenides ($Fe_{1+\delta}Se_xTe_{1-x}$). In another study, $C4 \rightarrow C2$ symmetry breaking in electronic states has been observed in both superconducting iron-based materials and their non-superconducting parent compounds. The relationship between the symmetry-broken states and superconductivity in these materials is an interesting question, and SI-STM, as a spatially resolved technique, is in a good position to contribute towards its resolution. In several studies, the vortex state has been imaged, giving insight into vortex pinning (with relevance for technical applications) and the competing states introduced where superconductivity is locally quenched by a magnetic field. As full technical utilization of these materials will require a good knowledge of the vortex state, the quick pace of progress in this area is encouraging. Despite these achievements, however, at the present time much remains unknown about the iron-based superconductors, including most critically the mechanism of superconductivity. Pairing mediation is certainly unconventional (i.e., not primarily driven by electron-phonon coupling) and, so far, evidence points towards a mechanism related to magnetism, such as spin fluctuations. Still, definitive proof has yet to be offered. Indeed, it is worth mentioning that the connection (and possible coexistence) of superconductivity and magnetism in these materials is surprising. Due to the historically antagonistic relationship between magnetism (especially ferromagnetism) and superconductivity, and the strong magnetic moment of atomic iron, few would have expected to find superconductivity in iron-based materials. In this regard, the discovery of superconductivity in iron-based materials requires us to re-evaluate the old assumptions as to what constituent elements ought to be, or ought not to be, found in a superconductor.

In this work, my objective has been to help shed some light on the properties and nature of high T_c superconductivity in iron-based materials. To this end, I have conducted several SI-STM studies of compounds belonging to two families of iron-based superconductors, the iron chalcogenides and the iron pnictides. In order to carry out the studies, it was necessary to gain access to an STM with SI-STM capability and, in this case, an all-new device was constructed. The features of this home-built STM include customized software, electronics, and vibration isolation, and a measurement head which has been machined out of crystalline Al_2O_3 (sapphire). Sapphire was chosen due to pre-construction analysis which indicated that a sapphire head would have superior mechanical and thermal properties, i.e. higher stiffness and higher thermal conductivity, as compared with a head made of alternative materials. Throughout the design and construction process, the device was optimized for the high stability, low noise conditions needed for SI-STM experimentation. A 1K-pot refrigerator and high performance superconducting magnet integrated in the setup allow measurements at temperatures down to about 1.6K and in fields of up to 14T (16T with λ-stage cooling).

The studies presented in the body of this work focus on the spatially resolved characterization of superconductivity at the sample surface. In one study, the relationship between impurities and superconductivity is investigated for two iron chalcogenide samples, one with many impurities and one with few impurities. The relationship between impurities and superconductivity is an important aspect for crystal growers to consider, and may provide clues helpful in uncovering the underlying mechanism of superconductivity in iron-based materials. In another study, the origin and consequences of nanoscale inhomogeneity of the superconducting gap is examined for one iron chalcogenide and one iron pnictide. Study of electronic inhomogeneity may help to quantify important parameters such as superconducting coherence length, and may likewise lead to a better understanding of the origin of high T_c superconductivity in iron-based materials. Previously, nematic electronic states have been reported in the iron chalcogenides; in this work, I image these states and consider their relationship with iron-based superconductivity. Whether symmetry-broken electronic states simply coexist with, or perhaps actively compete with, superconductivity is an intriguing question which may provide insights into the nature of pair formation in these materials. Finally, the vortex state, its energy evolution, and the formation of a vortex lattice are characterized for one iron chalcogenide superconductor. As previously mentioned, a better understanding of the vortex state in iron-based materials will have important implications for practical considerations such as technological utilization.

Chapter 2

Spectroscopic Imaging as an STM Technique

In which I introduce the technique and instrument used to carry out the several studies.

2.1 Theory

2.1.1 STM

A scanning tunneling microscope (STM) is a device which exploits the strong distance dependence of quantum tunneling of electrons in order to probe the surface of a conducting or semi-conducting material. The components of an STM are shown schematically in fig. 2.1. In order to induce tunneling, a bias is applied across the junction between tip and sample and the resulting current is then maintained with the help of a feedback loop. The tip is scanned over the sample and topographic information is recorded. In the vacuum tunneling regime the distance dependence of the tunneling current is such that a change in separation between tip and sample of roughly 1 Å equates to a change in current by 1 order of magnitude. In contrast to some other scanning probe techniques, STM has the advantage that all of the signals needed for operation are electronic, leading to superior speed, sensitivity and resilience, especially at low temperatures. Moreover, with STM one can probe the electronic structure of a material with tunneling spectroscopy (STS).

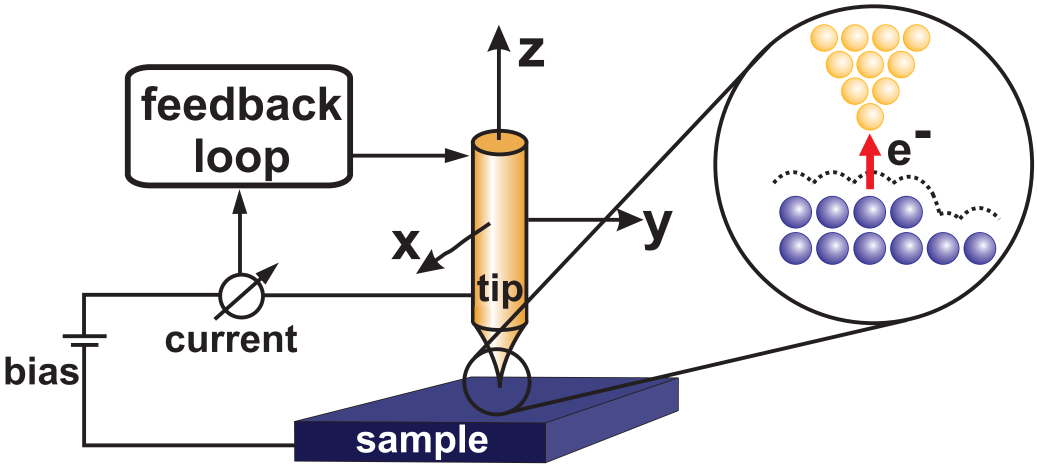

Figure 2.1: Schematic representation of an STM. To induce a tunneling current, a bias is applied across the junction between tip and sample. The tunneling current is maintained at the desired value by the feedback loop.

The first functional STM was built by Gerd Binnig and Heinrich Rohrer (†2013) in 1981 [4], soon after the emergence of modern signal processing and control technology, i.e. modern computers. However, Russell Young is credited with developing the original idea. He and his colleagues built a similar device almost ten years earlier, the “topografiner” [5], which, however, did not rely on vacuum tunneling for operation but rather on field emission.

In the following, a conceptual summary of the quantum tunneling of electrons in scanning tunneling microscopy / spectroscopy is given. An exhaustive treatise of this topic can be found, e.g., in ref. [6], edited by Joseph Stroscio and William Kaiser. For a more concise treatment see ref. [1], by Jennifer Hoffman.

In general, when two electrodes, such as the tip and sample in STM, are brought sufficiently close together, quantum tunneling of electrons occurs. Under equilibrium conditions – with no voltage applied – electrons will cross the vacuum barrier in both directions equally, from filled states into empty states of equal energy, resulting in zero net current. In order to induce a net electric current, a bias voltage is applied across the junction, which shifts the Fermi levels of the two electrodes relative to one another and, as the system attempts to re-establish energy equilibrium, results in a net flow of electrons from the negative electrode to the positive electrode. Of course, if it is convenient to do so we may also speak of missing electrons, or holes, traveling in the opposite direction, from the positive eletrode to the negative. In fig. 2.2, the basic concept is illustrated.

In STM, there are two basic modes of operation for imaging. In the constant-current mode, the tunneling current is kept at a constant level with the help of a feedback loop and the distance between the tip and sample (i.e. the voltage ap-

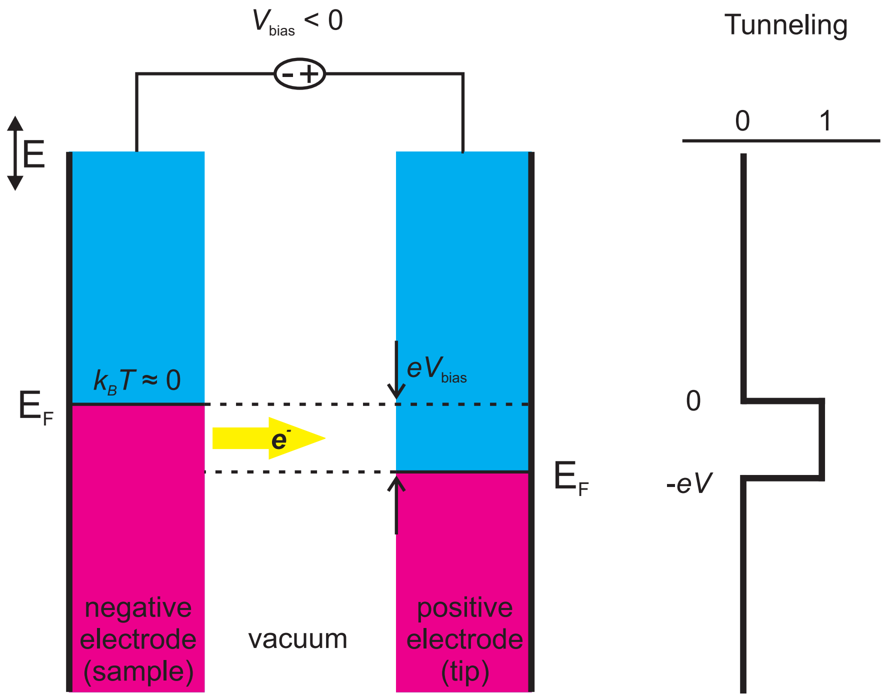

Figure 2.2: Schematic representation of the energy bands of a tip and a sample in STM. In the illustrated case, a negative bias has been applied with respect to the sample, so that its Fermi level has been raised by an amount equal to eV with respect to the Fermi level of the tip. At finite temperature, we would see a smearing of the Fermi levels of size k_BT. Here, we assume low temperature conditions with negligible smearing, in which case all tunneling occurs between the Fermi energies 0 and $-eV$.

plied to the z-axis of the scanning element) is recorded. In the constant-height mode, the arrangement is inverted so that the tip-sample distance is kept constant while the current is recorded.

We can describe the current flowing between tip and sample with perturbation theory. If $\rho_n(\epsilon)$ is the density of states (DOS) of the negative electrode and $\rho_p(\epsilon)$ is the DOS of the positive electrode, $f(\epsilon) = (1 + e^{\epsilon/k_BT})^{-1}$ is the Fermi distribution and $|M|^2$ is the matrix element, then we can express the current of elastic electrons flowing from the negative electrode to the positive electrode with the following expression:

$$I(\epsilon)_{\text{negative}\rightarrow\text{positive}} = -2e \cdot \frac{2\pi}{\hbar}|M|^2 \underbrace{(\rho_n(\epsilon) \cdot f(\epsilon))}_{\text{filled states}} \underbrace{(\rho_p(\epsilon + eV) \cdot [1 - f(\epsilon + eV)])}_{\text{empty states}}, \tag{2.1}$$

We can further express the smaller current of electrons tunneling against the voltage, from the positive electrode to the negative electrode:

$$I(\epsilon)_{\text{positive}\rightarrow\text{negative}} = -2e \cdot \frac{2\pi}{\hbar}|M|^2 \underbrace{(\rho_p(\epsilon + eV) \cdot f(\epsilon + eV))}_{\text{filled states}} \underbrace{(\rho_n(\epsilon) \cdot [1 - f(\epsilon)])}_{\text{empty states}}, \tag{2.2}$$

To calculate the net tunneling current from the negative to the positive electrode, we can now sum eqs. 2.1 and 2.2 and integrate over all ϵ:

$$I(eV)_{\text{net}} = -\frac{4\pi e}{\hbar} \int_{-\infty}^{\infty} |M|^2 \rho_n(\epsilon)\rho_p(\epsilon + eV) \underbrace{\{f(\epsilon)[1 - f(\epsilon + eV)] - [1 - f(\epsilon)]f(\epsilon + eV)\}}_{f(\epsilon)-f(\epsilon+eV)} d\epsilon, \tag{2.3}$$

With eq. 2.3 as a starting point, we can now make some reasonable approximations to simplify the integral.

First, SI-STM is a tool for imaging electronic structure, and we want to maximize our energy resolution. This is accomplished by making the Fermi energies of both the tip and sample as sharp as possible, which in practice means operating at low temperatures. At 1.6K, the base temperature of our instrument, the cut-off width of the Fermi function is $k_B T = 0.14$meV, which is already quite small compared to some of the other energy scales in the equation (e.g. a typical bias voltage of -100mV). We can therefore approximate an ideal, infinitely abrupt Fermi level for both the tip and sample and break the integral in eq. 2.3 into three non-overlapping parts.

If we define the Fermi energy of the negative electrode as 0 and the Fermi energy of the positive electrode is $-eV$, then the energy ϵ can be either greater than 0, less than $-eV$, or somewhere between the two values. If $\epsilon > 0$, then both $f(\epsilon)$ and $f(\epsilon + eV)$ in eq. 2.3 return 0, and $f(\epsilon) - f(\epsilon + eV)$ is 0. If $\epsilon < -eV$, then both $f(\epsilon)$ and $f(\epsilon + eV)$ return 1 and $f(\epsilon) - f(\epsilon + eV)$ is likewise 0. Finally, if $-eV < \epsilon < 0$, then $f(\epsilon)$ returns 1 and $f(\epsilon + eV)$ returns 0, in which case $f(\epsilon) - f(\epsilon + eV)$ returns 1. Thus, in this approximation, all tunneling occurs between the two Fermi energies $-eV$ and 0.

For operation at low temperatures, then, we can write down a simplified integral:

$$I(eV)_{k_B T \ll V} \approx -\frac{4\pi e}{\hbar} \int_{-eV}^{0} |M|^2 \rho_n(\epsilon)\rho_p(\epsilon + eV) d\epsilon, \tag{2.4}$$

Another simplification can be made if we assume that, of the two electrodes, only the sample's density of states is of interest. In tunneling spectroscopy the recorded signal will be (proportional to) a convolution of the density of states of both the tip and the sample. Since we are only interested in the sample, we want to choose a tip material with a DOS that is well known and as flat as possible. Many typical tip materials such as W, Pt, or $Pt_{0.9}Ir_{0.1}$ do in fact have a reasonably flat DOS within the relevant energy range (±100meV from the Fermi energy). Also, it is common practice to coat the tip in Au before use, which can also help to flatten the tip's DOS.

If we assume a perfectly flat DOS in the tip, ρ_{tip} will be constant and we can take it out of the integral. To do this, we will have to break the generality of eq. 2.4 and assign a polarity to the tip-sample junction. In the following, we will bias the sample negatively against the tip and take the DOS of the positive electrode $\rho_p(\epsilon + eV)$ out of the integral:

$$I(eV)_{\text{flat DOS in tip}} \approx -\frac{4\pi e}{\hbar}\rho_{p(tip)}(0)\int_{-eV}^{0}|M|^2\rho_{n(sample)}(\epsilon)d\epsilon, \tag{2.5}$$

Next, we consider the matrix element ($|M|^2$). In the theory of vacuum tunneling, first developed by Bardeen in 1961 [7] and restated by Cohen in 1962 [8], the matrix element expresses the probability that an electron will tunnel through the vacuum between two wave functions. Bardeen showed in his original theory that under ordinary circumstances the matrix element is independent of the energy differential between the tip and the sample. Specifically, those ordinary circumstances are that the tip and sample have independent DOS, that the considered wave functions fall off exponentially in the vacuum, and that they do not overlap significantly. If we make these assumptions, then the matrix element becomes independent of energy and can be taken out of the integral:

$$I(eV)_{\text{well separated electrodes}} \approx -\frac{4\pi e}{\hbar}|M|^2\rho_{p(tip)}(0)\int_{-eV}^{0}\rho_{n(sample)}(\epsilon)d\epsilon, \tag{2.6}$$

In order to calculate a value for $|M|^2$ we make two further approximations. First, we assume a square tunneling barrier between the two electrodes. This is reasonable because the "tilt" of the barrier is determined by the applied voltage ($\sim$ 100meV), whereas the height of the barrier will be closer to the work functions of the electrodes, which are much greater ($\sim$several eV). Second, we apply the WKB approximation, which assumes that the two wave functions decay exponentially into the vacuum. According to WKB, if m is the mass of an electron, s is the size (width) of a square vacuum barrier and ϕ is the height of the barrier, then the probability $|M|^2$ of an electron tunneling through the barrier will be given by the following expression:

$$|M|^2 = \exp(-2\int_0^s \sqrt{\frac{2m\phi}{\hbar^2}}dx) = \exp(-2\frac{s}{\hbar}\sqrt{2m\phi}) \propto I(eV), \tag{2.7}$$

Since the current is proportional to the matrix element ($I(\epsilon) \propto |M|^2$) and the matrix element is a function of the tip-sample distance (s) and the gap height (ϕ), we can determine the value of ϕ by measuring $I(\epsilon)$ as a function of s. The physical value of ϕ is determined by the work functions of the tip and the sample. From eq. 2.7, one can see that a higher value of ϕ will produce a higher sensitivity of $I(\epsilon, s)$ to a change in s. Therefore, choosing a tip with a larger work function will increase the sensitivity of the instrument to changes in tip-sample distance, increasing its spatial resolution in the z direction.

In order to make the approximations leading to eqs. 2.6 and 2.7 we have assumed that s is large enough that the wavefunctions of the tip and the sample do not overlap. Between the vacuum tunneling regime, where our equations are valid, and contact, where classical conductance channels dominate, there is a cross-over regime. In calculations published by Lang in 1987 [9] for the simple case of one Na atom at the tip, this regime was found to exist with a nuclear separation of between 5 − 8Å. SI-STM is typically performed well ouside the cross-over regime, in the exponential regime, so that our assumptions are valid.

Finally, we can replace $|M|^2$ in eq. 2.6 with eq. 2.7 and express the tunneling currents in SI-STM with the following approximation:

$$I(eV)_{\text{SI-STM}} \approx \frac{4\pi e}{\hbar} \exp(-s\sqrt{\frac{8m\phi}{\hbar^2}})\rho_{p(tip)}(0)\int_{-eV}^{0}\rho_{n(sample)}(\epsilon)d\epsilon, \tag{2.8}$$

2.1.2 Spectroscopic imaging

Spectroscopic imaging (SI-STM) is an STM technique that focuses on the characterization of electronic structure. The idea behind SI-STM is that mapping tunneling spectroscopy (STS) data to a topographic region with high spatial and energy resolution allows a detailed investigation of the relationship between electronic structure and topography.

In SI-STM, the tip is scanned over the sample surface as if taking a standard STM topography, with the difference that at each pixel of the image a tunneling spectrum (STS) is taken. As in standard STS, the feedback loop must be switched off before each spectrum. Since much more time is spent taking spectra than moving between pixels, the feedback loop is typically switched off most of the time, which increases vulnerability to external shocks, loud noises, etc. For this reason, and because of very long typical measurement times, a persistantly quiet environment is necessary for SI-STM.

The dataset gathered in SI-STM, a differential tunneling conductance ($g(\mathbf{r}, E)$) map, is three-dimensional, bounded in x and y by the size of the topographic region and in z by the energy (voltage). The resolution of x and y is given in pixels while that of z is given in layers. For calculating the time needed to take a map, reasonable accuracy can be achieved by knowing the total number of data points and the integration time per point. A typical map of resolution $x = 256$pxl, $y = 256$pxl, and $z = 21$ layers contains a total of $1,376,256$ data points. With a minimal integration time of $\tau = 0.1$s, the map would take just under 40 hours to complete. With a more typical integration time of $\tau = 0.25$s, the map would take around 4 days.

One of the strengths of SI-STM lies in its ability to measure local density of states (LDOS) in a fairly direct way. We can see how this works by rewriting eq. 2.8 to include a constant tip-sample distance and barrier height and leaving energy as the only variable:

$$I(eV)_{s,\phi=\text{const.}} = I_0 \int_{-eV}^{0} \rho_{n(sample)}(\epsilon) d\epsilon, \tag{2.9}$$

It is implied in eq. 2.9 that by sweeping the bias voltage V we can measure the integral of the density of states in the energy range $e\Delta V$. In fact, if we turn off the feedback loop and sweep the voltage in the appropriate energy range we can actually measure (the integral of) both the occupied states below the Fermi level and the unoccupied states above the Fermi level. ARPES, in contrast, is limited to the occupied states.

If we sweep the voltage and measure the current in a straightforward way we will end up with a physical quantity called the integrated density of states (IDOS). From the IDOS data, it is possible to simply take a numerical derivative to get a picture of the underlying LDOS. However, there is a better way to measure the LDOS which can improve the efficiency of the technique (because of the lower noise levels found at higher frequencies). This is to sweep the voltage V with a small modulation dV, provided by a lock-in amplifier. If we then record the corresponding modulation in current, dI, we can directly measure the quantity dI/dV, which is proportional to the LDOS and is called differential tunneling conductance, $g(\mathbf{r}, E)$:

$$g(\mathbf{r}, E) \equiv \frac{dI}{dV} \propto \text{DOS}(eV), \tag{2.10}$$

By sweeping dV and measuring dI we can therefore directly map out (a quantity proportional to) the LDOS. The energy resolution of this technique is limited by the amplitude of the modulation and by the temperature ($\approx 3.5 k_B T$). Ideally, in order to optimize resolution one would therefore set the modulation to the resolution limit set by the temperature (e.g. 0.14meV at 1.6K). In practice, the modulation voltage is often set higher than this in order to achieve an acceptable signal-to-noise ratio.

2.2 Instrumentation

2.2.1 Overview

In the following, the design, construction, and operation of a custom-built, low temperature and high magnetic field compatible scanning tunneling microscope (STM) is described. For a peer reviewed account of some aspects of the instrument, particularly the sapphire measurement head, please see ref. [10].

The core of the STM design consists of a sapphire measurement head which is situated at the bottom of a cryogenic insert. The insert is modular and during operation is connected to several supporting systems, such as a vibration isolation table, temperature regulation system and a superconducting magnet. The insert is an elongated stainless steel construction, containing, besides the measurement head, elements such as temperature sensors, a resistive heater, a 1-K pot refrigerator and an *in-situ* sample cleaving mechanism. The vibration isolation table is filled with around 1 ton of lead and is supported by a Newport passive isolation system. The Newport system itself rests upon a 7t concrete block which is supported from the building foundation by heavy duty steel springs. The temperature regulation system includes both heating and cooling capability and is designed to maintain a stable measurement temperature between $\approx 1.6 - 40$K. The temperature is controlled with a Lakeshore PID controller. The superconducting magnet can produce a field strength of up to 14T in normal operation or up to 16T with the help of a λ-point refrigerator. The scanning element is a 5-pole piezo tube [11] controlled by a home-built, high voltage amplifier. The sample transfer system allows pre-thermalization before cleaving in cryogenic vacuum and insertion into the measurement head.

2.2.2 STM measurement head

The instrument's measurement head has been optimized for high mechanical stiffness and thermal conductivity by choice of material (sapphire). A high stability measurement head is important for SI-STM due to the long continuous measurements characteristic of the technique. A CAD rendering and photograph of the assembled measurement head are shown in fig. 2.3 (a) and (b), respectively. The relevant structural and functional components are labeled.

Increasing the onset frequency of fundamental modes (ω_r) is an effective strategy for improving the intrinsic stability of an STM because of the damping imposed on external disruptions to the tunneling junction due to mechanical vibrations. The disruptions caused by external vibrations (which are typically < 100Hz) with frequencies lower than resonance ($\omega < \omega_r$) are strongly suppressed because the tip

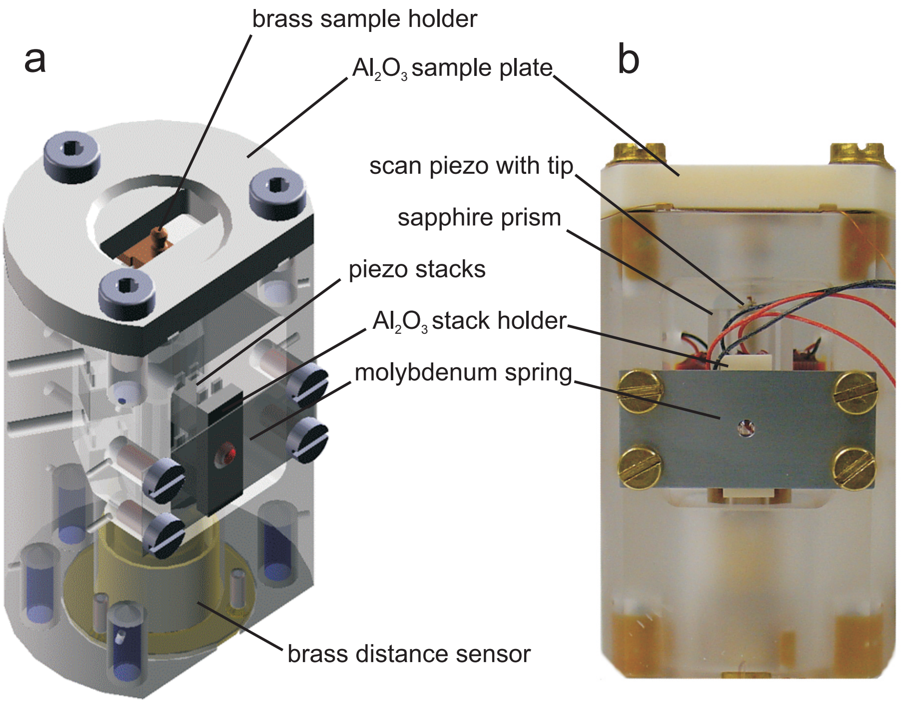

Figure 2.3: Sapphire STM measurement head. (a) A perspective view CAD rendering. (b) A front view fotograph.

and sample move in phase, while disruptions caused by frequencies greater than the resonance frequency ($\omega > \omega_r$) are fully transmitted to the tunneling junction. Therefore, it is helpful to increase the frequency of the instrument's fundamental resonant modes as much as possible. An increase of the resonance frequency of the measurement head by a factor of two reduces the transmission of perturbations in the low frequency range ($\omega \ll \omega_r$) by a factor of four. One way to increase the frequency of resonant modes is to optimize the geometry [12]. In this design, a further increase in mechanical stiffness has been achieved by optimizing the choice of materials, while the geometric architecture [13] has not been significantly altered from previous designs.

During the design process, a finite element analysis was carried out in which the four lowest-frequency resonant vibrational modes of the measurement head were calculated for three potential materials [15]. Preference was given to non-conducting materials in order to reduce the risk from electrical shorts, as well as to make the head less susceptible to heating from eddy currents (while ramping the magnetic field). The mesh used as well as the resulting displacement and stress patterns are depicted in fig. 2.4. The results for MACOR, amorphous aluminum

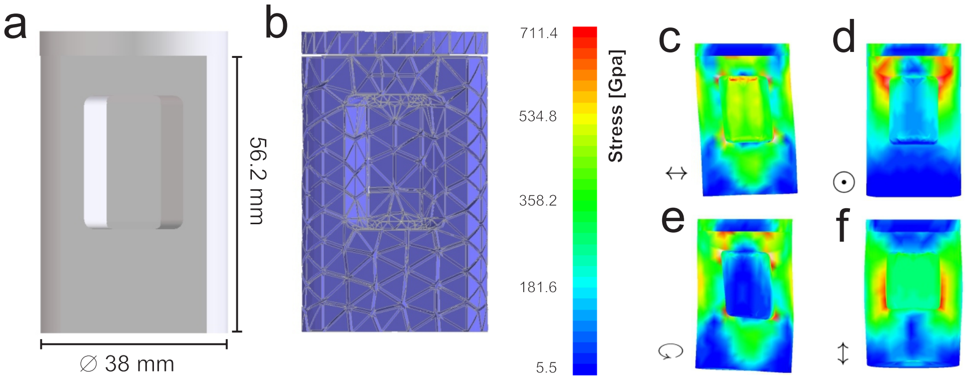

Figure 2.4: (a) 3D rendering of the measurement head. (b) Mesh used for finite element analysis. (c)-(f) Fundamental modes of the measurement head, modeled with the upper end of the STM head rigidly fixed, as it is in the experimental setup. (c) and (d) correspond to bending modes (↔ and ⊙), (e) to a torsional mode (↻) and (f) to a longitudinal mode along the long axis of the body (↕), which causes the strongest stress around the edges of the central cavity, as indicated by the color scale.

	Materials		
Modes[Hz]	MACOR	Al_2O_3	Sapphire
ν_1	5264	7055	8488
ν_2	5541	7323	8737
ν_3	10982	14962	17987
ν_4	19239	26036	31530
$\rho[\mathrm{g/cm^3}]$	2.5	3.9	3.98
G[GPa]	25.9	84.8	148.0
E[GPa]	66.9	206.8	335.0
$\kappa(300\mathrm{K})[\frac{\mathrm{W}}{\mathrm{m\cdot K}}]$	1.46	23	34-35.1

Table 2.1: Comparison of the four resonant modes for different materials. Listed are the four lowest-frequency modes, obtained via the methodology described in fig. 2.4. In addition, the materials' density (ρ), shear modulus (G), Young's modulus (E) and the thermal conductivity at room temperature (κ(300K)) are listed (values for MACOR from ref. [14], Al_2O_3 from ref. [15], sapphire from ref. [16]; isotropic averages were used which do not account for material anisotropy).

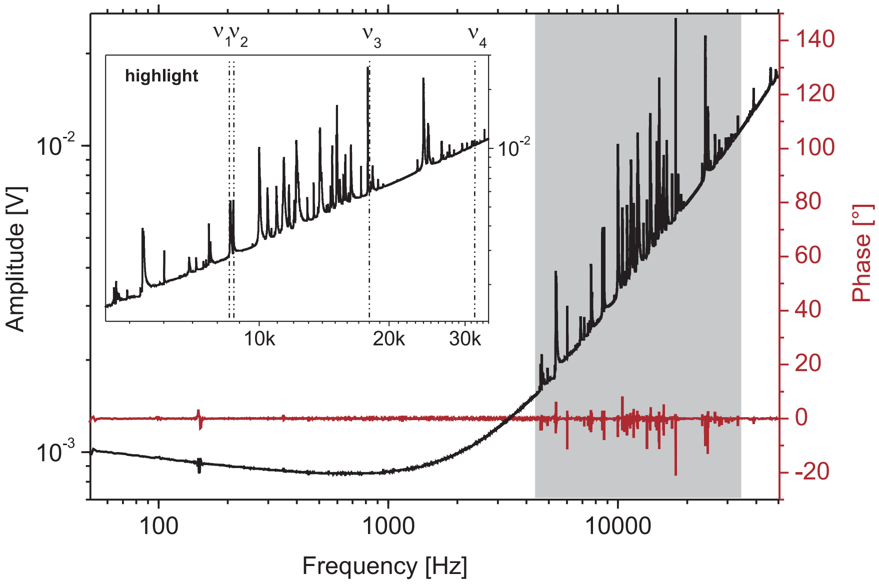

Figure 2.5: Sapphire measurement head modes, measured *in-situ* with a lock-in amplifier. Coarse approach piezo stacks are used for excitation (1V) and response detection. The highlighted area is zoomed for a more detailed view; calculated positions of the four primary modes of the body (as listed in tab. 2.1) are marked.

oxide, and sapphire are summarized in tab. 2.1. We found that, among the different materials, the resonant mode frequencies of the simulated measurement head (which scale with $\sqrt{G/\rho}$) vary by almost a factor of two. Based on the calculations, oriented single-crystalline sapphire was chosen as the building material. In addition to having the highest stiffness, sapphire also has a very good thermal conductivity [17], e.g. much better than that of MACOR, meaning that shorter thermalization times and cessation of related drift effects can be acheived. Furthermore, by using the same material (sapphire) for both of the main body components (the slider and the frame) and molybdenum for other structural components, stress effects due to differing coefficients of thermal expansion are minimized.

After constructing the sapphire head, the resonant modes were then measured *in situ* for comparison with the calculations. In fig. 2.5, the response of the measurement head is plotted as a function of the frequency of vibrational excitation (applied via one of the piezo stacks). The measurements were performed on the fully assembled, mounted head at low temperature. The abberations at 50, 100, and 150Hz are artifacts due to the AC line frequency. Resonant modes begin to appear at frequencies higher than ~ 4.6kHz, with the first large peak appearing at 4.659kHz. Other parts within the measurement head such as the tip, scan piezo and wiring may have resonances at lower frequencies which affect the stability of the tunneling junction, but these modes may not show up in the measurement since they would not necessarily be expected to excite the massive sapphire of the body. In order to minimize vibrational coupling to the tunnel junction through the wiring, a thin tip wire was chosen which has also been tightly bound to the sapphire body with Teflon tape.

In this design, the coarse approach of the tip towards the sample (from below) is realized through a flattened V-shaped cavity in which a prism is clamped between six piezo stacks [18]. By laterally actuating the piezo stacks, the central prism can be moved up or down. Due to its compact and rigid form, this design provides a high level of stability [19]. The design of the sapphire body is optimized to reduce the required number of processing steps, so that machining the raw material becomes more practical. In particular, in order to avoid difficult and expensive machining of threads in bulk sapphire we have instead glued threaded sleeves made of molybdenum into corresponding smooth bores.

Features of the measurement head include a coarse-approach motor built according to the design by S.-H. Pan [13], a capacitive distance sensor [1], and a sample exchange mechanism. The coarse approach piezos [20] are driven individually by a home-built piezo motor controller (PMC). This PMC drives slider movement in a frictional walking mode in which the six piezo stacks are fired synchronously during the slow ramp, while the fast ramp is performed asynchronously (i.e. the piezos are actuated one at a time). This mode contrasts with inertial operation, or jumping mode, in which the six piezo stacks are always actuated synchronously. While the inertial mode simplifies the wiring – reducing the seven wires needed to connect the piezo motor to the electronics to two – it moves the slider less reliably. Operating the piezos in frictional or walking mode can increase the step size for the same driving voltage by up to a factor of two [21].

2.2.3 Scanning element

The scanning element is a 5-pole piezo tube [11] controlled by a home-built, high voltage amplifier with digitally controlled gain for independent movement in the x,y, and z directions. Each direction is further subdivided into offset and scan channels, again each with its own gain. The separation of offset and scan channels allows permanent access to the full scanning range, even for small scan-channel gain settings.

The tip itself is a $\oslash = 0.2$mm wire of $\sim$ 5mm in length, affixed to the end of the scan element, which has been prepared by cutting with wire cutters. Over the course of this work, various tip materials such as W, Pt, Ir, $Pt_{0.9}Ir_{0.1}$, and V were tried with varying degrees of success. $Pt_{0.9}Ir_{0.1}$ and V were eventually determined to be the best tip materials as they represent the most favorable compromise between mechanical stiffness, malleability, and perceived performance. Each tip used in experiments was also coated with Au in a field emission procedure in order to create an electronically neutral probe with a flat DOS.

2.2.4 Sample preparation

Samples are transferred with a long stainless steel rod from the top of the insert straight into the measurement head. An *in-situ* cleaving mechanism anchored about half way down the insert on the 4K-plate allows pre-thermalization of the sample before cleaving in cryogenic vacuum and insertion into the measurement head. Cleaving is done by knocking off a ∼ 7mm long brass rod which has been glued to the top of the sample with silver epoxy prior to transfer. The diameter of the rod is chosen based on the size of the sample.

Pre-thermalization and *in-situ* cleaving is a strong point of this design as it removes the possibility of sample contaimination prior to transfer. Of course, the price paid for this is the partial destruction of the sample after each cleaving.

2.2.5 Cryogenic insert

The cryogenic insert, depicted in fig. 2.6, houses most of the active components of the STM and acts as the integration node for the measurement head and the vibration isolation, temperature control and magnetic field control systems. The insert operates at a base temperature of down to ∼ 1.2K (1K plate) and 1.6K (base plate), as measured by Cernox temperature sensors installed at those locations [22, 23]. When the 1K pot is not in operation, the temperature of the insert stabilizes at 4.2K – the 1K plate is then coupled via helium gas in the 1K pot pump line to the helium bath.

2.2.6 Vibration isolation

The cryostat is mounted on a two-stage vibration isolation system, a CAD rendering of the system is shown in fig. 2.7. The outer stage consists of a 7t concrete block, supported by steel springs, while the inner stage consists of a 1t vibration isolation table supported by passive pneumatic air springs [24]. The cryostat is supported by the vibration table, but its center of mass and most of its length rests within a $\oslash = 60$cm full-length bore in the concrete block.

The system is designed to offer the tunneling junction protection from external

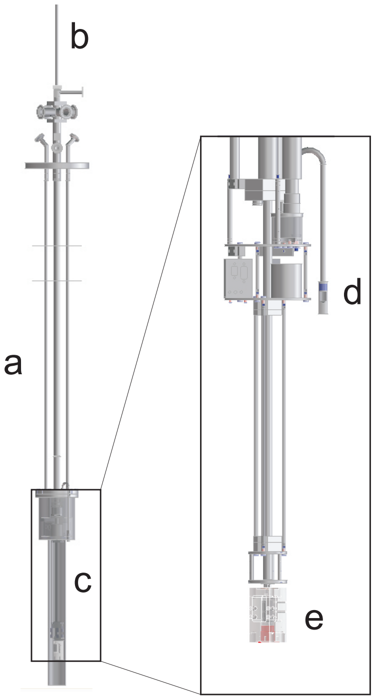

Figure 2.6: CAD rendering of the cryogenic insert. (a) The transfer tube. (b) The sample transfer rod. (c) The vacuum can. (d) The 1-K pot refrigerator siphon. (e) The sapphire STM measurement head.

mechanical disturbances over the full range of frequencies. While the building foundation, concrete block and vibration isolation table tend to act most effectively in reducing high frequency noise (i.e. as a low-pass filter) due to their large mass and moment of inertia, the sapphire measurement head itself tends to act as an effective high-pass filter due to its lack of low-frequency resonances. In combination, these elements attenuate the final noise level in the tunneling current by several orders of magnitude. In fig. 2.8, the noise amplitude at several stages in the vibration isolation system is plotted. Compared to the background noise prevalent at the laboratory floor, the amplitude measured at the tunneling junction is lower by a factor of ten million.

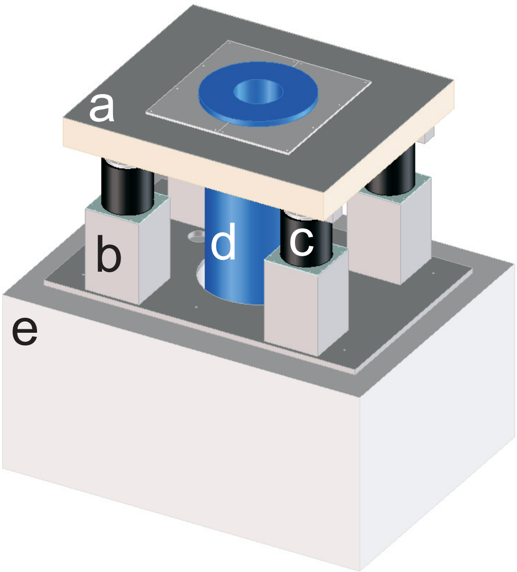

Figure 2.7: CAD rendering of the isolation table. (a) The wooden table filled with 1000kg of lead. (b) Sand filled wooden boxes. (c) Newport passive isolation system. (d) The cryostat. (e) 7000kg concrete block resting on iron springs on the foundation of the building.

2.2.7 Temperature control

The temperature at the STM measurement head can be controlled by a combination of resistive heater (100Ω) and 1K-pot refrigerator, and monitored at three nearby locations via Cernox temperature sensors (two 1030SD and one 1050SD). The heater and the temperature sensors are under proportional integral derivative (PID) control through a Lakeshore model 336 temperature controller, while the 1K-pot refrigerator is manually set to *on* or *off* by adjusting a valve. Operation of the 1K-pot has been found to not increase LHe consumption by a detectable amount compared to the natural boil-off rate.

The LHe in the cryostat (maximum 100L) represents a thermal reservoir which pulls the temperature of the insert towards thermodynamic equilibrium at the boiling point of LHe (4.22K). According to the law of heat conduction (Fourier's law), the heat flux between the insert and the LHe reservoir is proportional to the negative temperature gradient:

$$\overrightarrow{q} = -k\nabla T, \tag{2.11}$$

where $\overrightarrow{q}$ is the heat flux density, k is the thermal conductivity, and ∇T is the temperature gradient. In the context of the temperature control system, eq. 2.11

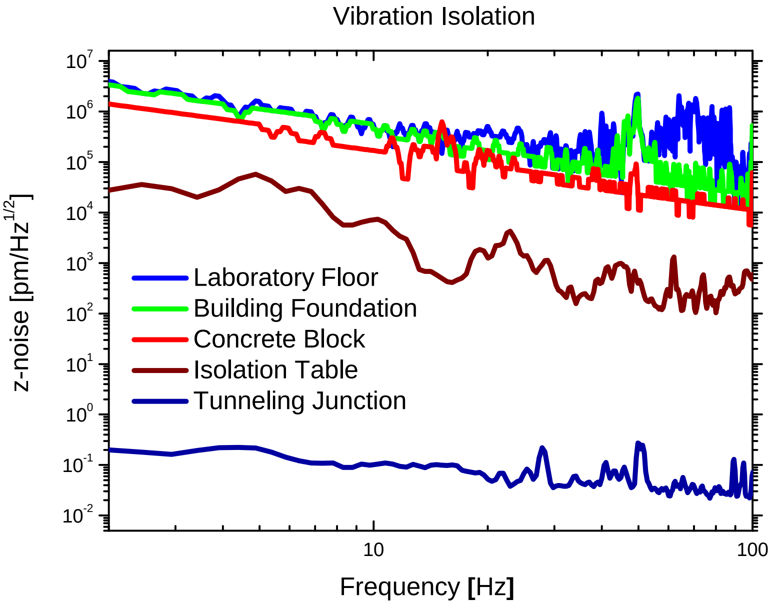

Figure 2.8: Noise level (vertical component) at various stages between the laboratory floor and the tunneling junction. The tunneling junction noise was measured via the feedback loop control voltage applied to the scan piezo during tunneling. All other noise levels were measured with a commercial geophone [25].

represents a proportional regulator which sets an effective lower bound to our temperature control range. Since the only thermally conducting pathway from the LHe reservoir to the STM measurement head leads through the 1K-pot refrigerator, and the cooling power of the refrigerator is constant, the lower limit of achievable temperature is reached at the point at which the heating power from the reservoir exactly equals the cooling power from the refrigerator. The lower limit in this construction has been empirically determined to be about $T \approx 1.2$K. However, the minimum achievable temperature at the measurement head is further moderated by the effects of radiative heat transfer from the inner wall of the vacuum can, which can bypass the 1K-pot refrigerator. The thermal power emitted by an object with a constant emissivity factor is given by the Stefan-Boltzmann law:

$$P = \epsilon \sigma A T^4, \tag{2.12}$$

where P is the radiated power, ϵ is the emissivity factor of the object, σ is its proportionality constant, A is its surface area, and T is its temperature. Since the relative thermal power emission between the STM measurement head and the

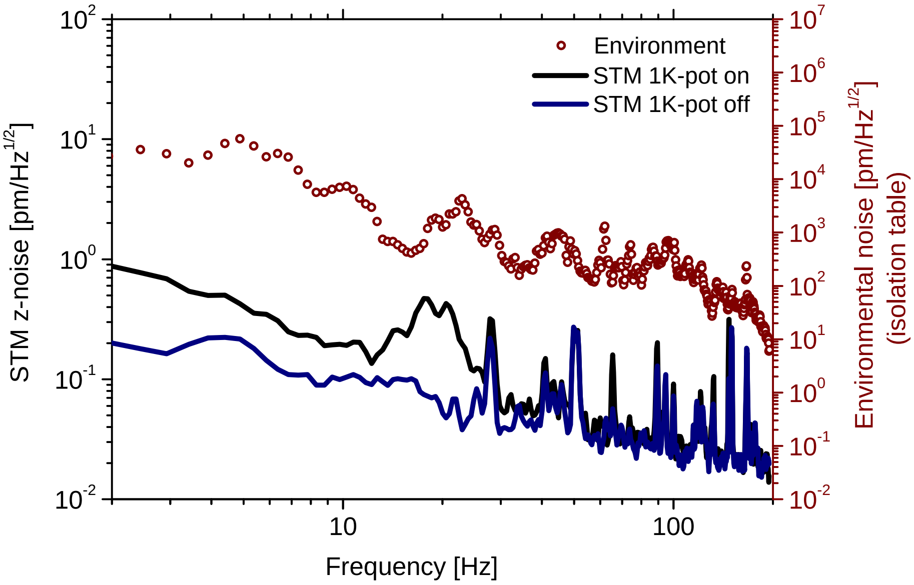

Figure 2.9: Tunnel junction noise at 1.7K, with the 1K-pot turned on and off (i.e. being pumped or not pumped), as measured via the feedback loop control voltage applied to the scan piezo during tunneling. For comparison, the environmental noise on top of the isolation table was measured with a commercial geophone [25] and plotted alongside.

inner wall of the insert depends on T^4, a small difference in temperature can potentially lead to a large transfer of thermal energy per unit time. In this case, radiative heat transfer is enough to increase the minimum temperature at the STM measurement head to about $T \approx 1.6$K.

At the upper limit of the temperature range, the mentioned thermodynamic processes do not pose the same constraints because there is no strong limit to the amount of resistive heat energy that can be introduced into the system. Insofar as the LHe reservoir continues to regulate the temperature in the cryostat, the limiting factors become the tolerable boil off rate and problems caused by the increasingly steep temperature gradients, as well as by the general instability characteristic of STM operation at higher temperatures. Operation of this instrument has been demonstrated up to $T \approx 40$K.

Due to LHe boil-off, the dewar must be refilled once every five days. Combined with waiting times to allow for thermalization and the subsidence of drift effects, this constraint limits the length of a single measurement to around four days.

A measurement of tunneling junction noise up to 200Hz, with and without operation of the 1K pot, is shown in fig. 2.9. For frequencies above 30Hz, the curves with and without pumping of the 1K-pot appear to coincide, while clear differences emerge for lower frequencies. For comparison, the environmental noise, as measured on the vibration table with a geophone, is also plotted. It should be noted that we do not observe a degradation in the tunneling signal (either in topographies or in spectra) due to operation of the 1K pot.

2.2.8 Magnetic field control

The superconducting magnet is a single-coil Nb_3Sn with a stated homogeneity of $1{:}10^3$ over a spherical center volume of $\oslash = 10$mm. It has a cylindrical central bore of $\oslash = 52$mm. The power supply is an IPS120-10 (120A, 10V). Both the magnet and the power supply are from Oxford Instruments.

The magnetic field encountered at the sample can be tuned from the level of the natural Earth field (less than 100μT), up to 14T at standard LHe temperature, or up to 16T while pumping a λ-point refrigerator to cool the magnet.

2.2.9 Software and electronics

The STM is controlled with the open source software GXSM [26, 27] and an Open Source SPM Controller from Soft dB [28]. The software has been modified for spectroscopic imaging functionality. The tunneling current is sampled with a variable-gain commercial current amplifier [29], which is controlled with the integrated STM software.

The sensitive electronic signals (most critically the pre-amplification current signal) are carefully shielded from radiofrequency (RF) and other electromagnetic noise. The centerpiece of the electronic isolation system are several filter boxes carved out of solid brass with a 5-axis CNC. The boxes are hermetically sealed and each wire is filtered individually with an RF filter of appropriate specifications.

2.2.10 Calibration

In fig. 2.10 (a), first results obtained (without operation of the 1K-pot) on *in-situ* cleaved $NbSe_2$ are shown. Atomic resolution and the charge density wave (CDW) order [30] can be seen easily. In fig. 2.10 (b), an image recorded (with a different STM tip) with operation of the 1K-pot is shown. The line cuts in fig. 2.10 (c) and (d) show that the residual vertical noise at the tunneling junction can be brought

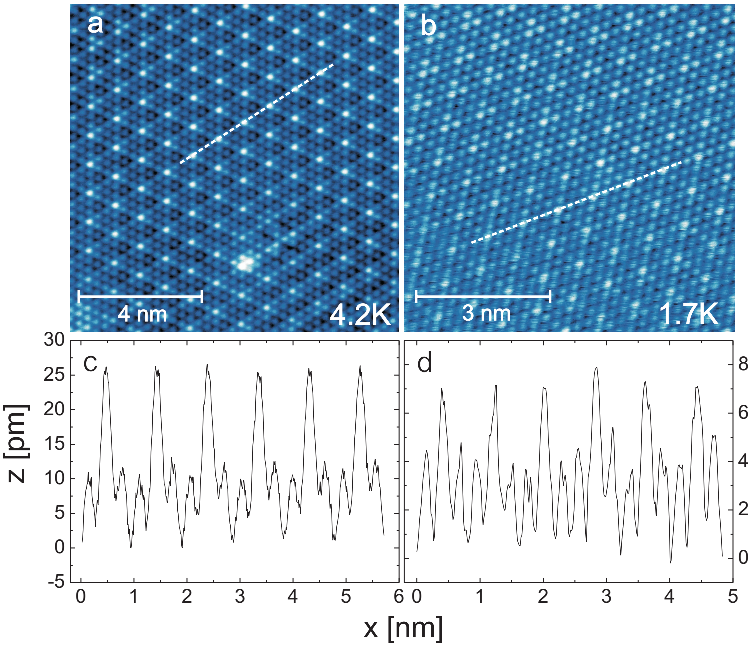

Figure 2.10: Topographic images (raw data) of $NbSe_2$ at (a) 4.2K (without operation of the 1K-pot) and (b) 1.7K (with operation of the 1K-pot) acquired with $V = 100$mV and $I = 0.5$nA, taken with different tips on different samples. (c) and (d) show line cuts through the topographic images in (a) and (b) along the indicated paths, demonstrating the vertical stability of the system.

below 1pm under optimal conditions, as suggested in section 2.2.6. The known lattice constants of $NbSe_2$ have been used to calibrate the scanning element.

In order to estimate the energy resolution of the instrument, we have recorded tunneling spectra on $NbSe_2$ as a function of temperature. The superconducting gap of $NbSe_2$ is well known and was first measured with tunneling spectroscopy by Hess *et al.* [31]. However, due to the anisotropic band structure and coexistence with CDW order, the precise shape of the expected gap is not entirely clear (see, e.g., refs. [32, 33] and references therein).

In fig. 2.11 (a), tunneling spectra acquired on $NbSe_2$ at 4.2K, 3K, and 1.7K are shown. The superconducting gap can be seen clearly. The temperature dependence indicates that the achieved energy resolution is sufficient to clearly differentiate gap features at 1.7K from those measured at 4.2K. In fig. 2.11 (b), calculated spectra are shown for comparison. The calculated spectra were obtained by assuming that the superconducting gap in $NbSe_2$ can be described by the Dynes gap equation [34],

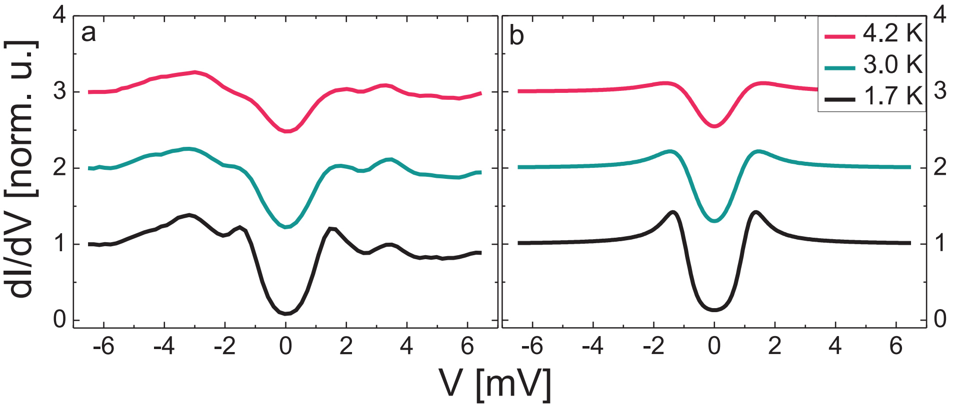

Figure 2.11: Tunneling spectroscopy characterization of $NbSe_2$, showing the superconducting gap. (a) Superconducting gap as a function of temperature (lock-in modulation: 0.5mV, 405Hz, 30ms lock-in averaging); spectra are averaged from small maps. (b) Spectra calculated with eq. 2.13 with the lock-in broadening used in the experiment. Spectra in (a) and (b) have been normalized and offset vertically for clarity.

$$\rho(E) = \mathrm{Re}\frac{E - i\Gamma}{\sqrt{(E - i\Gamma)^2 - \Delta^2}}, \tag{2.13}$$

using values for the quasiparticle-lifetime broadening $\Gamma = 120\mu\mathrm{V}$ and superconducting gap $\Delta = 1.2\mathrm{mV}$. The spectra were obtained by first calculating the current [35], taking into account the broadening due to the Fermi-Dirac-distribution (in the tip). Thereafter, the differential conductance was obtained by calculating the lock-in derivative. It should be noted that the real structure of the superconducting gap in $NbSe_2$ is more complex than this model, due to the aforementioned coexistence of CDW order with superconductivity and possible multiple gaps. This comparison can therefore only serve as an indication for the energy resolution of the instrument.

Chapter 3

Superconductivity in Iron Chalcogenides and Iron Pnictides

In which I introduce the object of study, beginning with a timeline of superconductivity research, continuing with a brief review of BCS theory, the cuprates, and the iron-based superconductors, and ending with a description of the investigated compounds.

3.1 Introduction

More than one hundred years ago, the condensed matter phenomenon known as superconductivity was observed for the first time. The story begins early in the last century with a major technological breakthough, the liquefaction of helium, achieved by Dutch physicist Heike Kamerlingh Onnes. With this breakthrough, the temperature scale available for physical experimentation was at once lowered by more than one order of magnitude, and Onnes set to work straight away conducting experiments in the new frontier. Just three years after the initial breakthrough, in 1911, he then made an extraordinary discovery. While investigating the resistivity of mercury down to the lowest temperatures, his measurement parameter, which had been steadily decreasing, suddenly vanished [2]. This was not an error. In fact, though it would be many years before theory caught up, the newly discovered phenomenon was a reflection of a macroscopic quantum mechanical state similar to a Bose-Einstein condensate [36, 37] – superconductivity.

Next, two decades after Onnes' work, a second major property of the superconducting state was discovered – perfect diamagnetism. In 1933, German physicists Walther Meissner and Robert Ochsenfeld discovered this property when they observed the expulsion of magnetic flux lines from superconducting tin and lead

[38].

Then, in 1957, nearly half a century after Onnes' discovery, theory finally caught up to experiment when John Bardeen, Leon Cooper and John Schrieffer proposed a microscopic theory of superconductivity (BCS theory), which still provides the theoretical basis for the science of superconductivity to this day [39].

The success of BCS theory was by no means the end of the story, however. Two decades after BCS was proposed, physicists Andres, Graebner and Ott discovered so-called heavy fermion behavior. Measuring linear specific heat capacity in $CeAl_3$, below a certain temperature they began to record enormous values, such as would be expected in a theoretical system with extremely massive electrons [40]. In fact, the heavy fermion systems are strongly correlated materials which have a characteristic temperature above which they behave as normal metals (with a quasi non-interacting Fermi gas) and below which electron interactions begin to dominate the physics of the system. When, a few years later, superconductivity was discovered in the heavy fermion material $CeCu_2Si_2$, by Steglich *et al.*, another small revolution in thinking occured [41]. While investigation of conventional superconductors doped with impurities had previously given the impression that the existence of localized magnetic moments and superconductivity in the same material were always incompatible, this discovery proved otherwise. More recently, the discovery of a quantum critical point and non-Fermi liquid behavior in the phase diagram of heavy fermion compounds by von Löhneysen *et al.* has generated a new wave of interest in these materials [42]. Today, heavy fermion compounds are the object of ongoing experimentation. However, investigation of these materials is technically challenging as extremely low temperatures are required. For this reason, a duplicate of the instrument developed for the present work [10] has been modified for use in a dilution refrigerator [43] and is being used by collegues for parallel experiments.

Getting closer to the present day, the current epoch of superconductivity might be said to have begun in 1986 with the discovery of superconductivity in the layered compound LaBaCuO, by Johannes Bednorz and Karl Müller [3]. Finding superconductivity in a ceramic material was surprising by itself, but even more so with the unprecedented transition temperature of 35K. This T_c was more than 50% higher than that of the previous record holder and its discovery generated possibly unprecedented excitement in the condensed matter physics community. The discovery opened up the field of cuprate superconductivity and led over the subsequent decades to hundreds of thousands of scientific publications [1].

Finally, in 2006, in a search for novel superconductors containing transition metal ions, Hosono and coworkers published the breakthrough discovery of LaOFeP, with a T_c of around 4K [44], and subsequently LaOFeAs, for which it was found that T_c could be increased from below 1.8K [45] up to $\sim$ 26K [46] by substituting F^{1-} for O^{2-} at a small percentage of O^{2-} sites, and then further up to 43K under pressure. Echoing the discovery of the cuprates, and with similar phase diagrams pointing to a similarly unconventional, qualitatively new superconductivity, this was a very exciting development for the community. Most remarkable was perhaps the fact that the new compound family contained iron, which due to its strong association with magnetism had been considered an unintuitive element to look for in a superconductor.

At the present time, groups around the world continue to investigate recently discovered iron-based superconductors with a variety of techniques. Despite significant progress being made towards understanding basic aspects of iron-based superconductivity, such as pairing symmetry [47], the microscopic mechanism or mechanisms underlying iron-based superconductivity are not yet well understood.

3.2 BCS theory

Underlying the phenomenon of superconductivity is the pairing of fermionic, quasi-free electrons into two-electron quasiparticles with bosonic character. In 1956, Cooper showed that pair formation can occur in the presence of any arbitrarily small attractive potential [48] – which in the case of conventional superconductors is provided by electron-phonon interactions. Most superconductors are spin-singlet, meaning that paired electrons must have opposite spin and momentum and that each resulting Cooper pair has a total spin and momentum equal to zero. In the BCS ground state, all free electrons are paired and the electronic character of the system has effectively changed from fermionic to bosonic; the Fermi sea has undergone a phase transition analogous to Bose-Einstein condensation [36, 37].

In tunneling experiments, a superconductor will show a gap in the LDOS, the size of which represents the energy which must be expended to break up each Cooper pair, or, in other words, double the amount by which pair formation is energetically favorable; if pairing gains each electron an energy Δ then a gap of size 2Δ will be visible in the LDOS, centered at the Fermi energy.

For a BCS superconductor, the transition temperature (T_c) is related to the gap size at zero temperature ($\Delta_{T=0}$) by the following equation:

$$2\Delta_{T=0} = 3.52 k_B T_c. \tag{3.1}$$

A more general equation, which allows the calculation of T_c from the gap size at a finite temperature, is the following [49, 50]:

$$2\Delta(T) = 2\Delta_{T=0} \tanh\left(\frac{\pi}{2}\sqrt{T_c/T - 1}\right). \tag{3.2}$$

The single particle density of states in the superconducting state ($\rho_{sc}(\epsilon)$) is related to the normalconducting density of states ($\rho_{nc}(\epsilon)$) in a straightforward way; for $\epsilon < \Delta$, $\rho_{sc}(\epsilon) = 0$. For $\epsilon \geq \Delta$,

$$\rho_{sc}(\epsilon) = \rho_{nc}(\epsilon)\frac{\epsilon}{\sqrt{\epsilon^2 - \Delta^2}}. \tag{3.3}$$

In other words, inside the gap the density of single particle states is zero, while at the gap energy ($\pm\Delta$) the density of states diverges.

In BCS superconductors, pair formation is mediated by phonons, which are quantized lattice vibrations described, e.g., in the Debye model [51]. In terms of the Debye model, T_c can be expressed in relation to the Debye cut-off energy (E_D), the density of states at the Fermi level (ρ_F), and the pairing potential (V), by the following equation:

$$k_B T_c = 1.14 E_D e^{-1/\rho_F V}, \tag{3.4}$$

where $\rho_F V$ is a material-dependent parameter which describes the electron-phonon coupling. The regime where this parameter is small ($\rho_F V \ll 1$) is called the weak coupling limit and outside this limit the original BCS theory is no longer applicable. However, in 1960 Éliashberg developed a more general description of superconductivity where electron-phonon coupling of arbitrary strength is permitted [52, 53].

The isotope effect, i.e. that for a given superconducting material the critical temperature is inversely proportional to the mass of the isotope in the material, was successfully predicted by BCS theory. The effect was experimentally verified by Maxwell in 1950 [54] and independently by Reynolds *et al.* [55] around the same time. The Debye cut-off energy (E_D) for different isotopes of the same element was expected to be proportional to $m^{-\alpha}$, where $\alpha = 0.5$ and m is the isotope mass – and eq. 3.4 accurately reproduces the isotope effect as observed in experiments.

The coherence length (ξ) and mean free path (l) are useful parameters for describing the behavior of superconductors. The coherence length is a measure of the spatial extent of the pairing wavefunction. Application of the uncertainly principle to the total pairing energy 2Δ allows us to give an approximate value for ξ [56]:

$$\xi \sim \frac{E_F}{k_F \Delta}, \tag{3.5}$$

where k_F is the Fermi momentum. According to this approximation, pure metal superconductors such as mercury and aluminum would be expected to have coherence lengths on the order of $\xi \sim 10^2 - 10^3$nm. Unconventional superconductors, including the iron-based superconductors, typically have coherence lengths which are orders of magnitude smaller.

The mean free path decribes how far the average electron can travel without being scattered, e.g. due to impurities, lattice defects, or temperature effects. The mean free path is given by $l = \tau v_F$, where τ is the average time between scattering events and v_F is the Fermi velocity. A superconductor in which $l > \xi$ is said to be in the clean limit while a superconductor in which $l < \xi$ is said to be in the "dirty" limit, due to the increased scattering.

3.3 Cuprates

In the previous section I have introduced superconductivity with a focus on BCS theory. In the following, I will introduce the so-called unconventional superconductors – those which cannot be described by BCS theory – beginning with the cuprates.

As a class, unconventional superconductors differ from classical superconductors on several points. The most basic difference is that in the unconventional superconductors pair formation is mediated primarily by something other than electron-phonon coupling. The heavy fermions were the first class of unconventional superconductors to be discovered but several others have been discovered since, notably the cuprates.

The cuprate superconductors are layered materials characterized by a copper-oxide plane sandwiched between a number of supporting layers. In the absense of doping, cuprates have a half-filled 3d valence shell which leads to a splitting of the main band into upper and lower Hubbard bands and results in a material which is an antiferromagnetic Mott insulator. However, as can be seen in the phase diagram in fig. 3.1, antiferromagnetism can be suppressed via charge doping, allowing the emergence of the superconducting state.

The discovery of the cuprates represented a major turn in the history of the science of superconductivity. First, the cuprates proved BCS expectations of maximum T_c to be false. For example, $HgBa_2Ca_2Cu_3O_{8+\delta}$, the current record holder, has a T_c at ambient pressure of 135K [58], well above both the predictions of BCS theory and the theoretical limit for phonon-mediated pairing. Second, successful BCS predictions such as the isotope effect and the relation of gap size to T_c given in eq. 3.1 do not hold for these materials, even when allowing for later refinements to the theory. For example, in the cuprates, gap size to T_c relations of up to $2\Delta/k_BT_c = 5$ have been observed [59].

Another departure of the cuprates from BCS superconductors is the symmetry of the pairing wave function (order parameter). Instead of the simple s-wave symmetry, expressed, e.g., in a gap size which is isotropic as a function of momentum, the cuprate order parameter was found to have d-wave character (though there may be exceptions [60, 61]). There are several important consequences of the d-wave

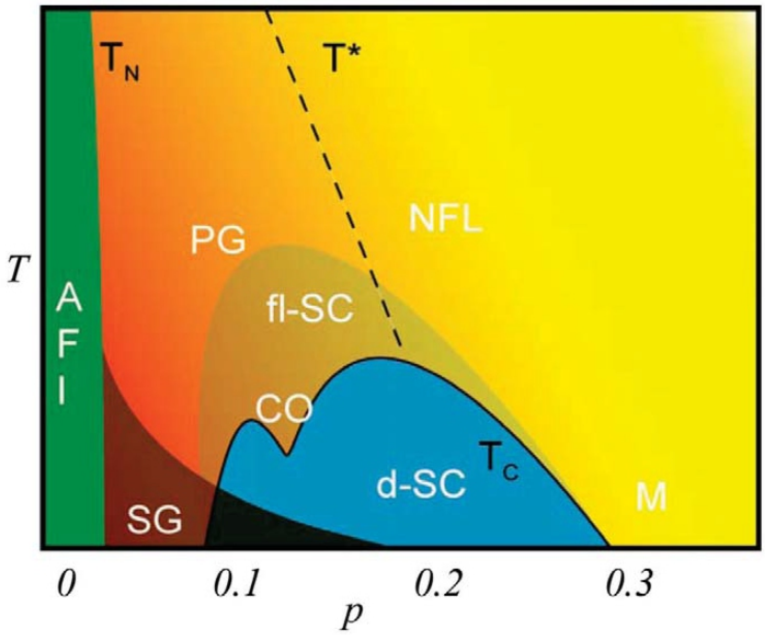

Figure 3.1: [57] Generalized cuprate phase diagram as a function of temperature T and hole doping p. The region labled AFI is antiferromagnetic and insulating, PG is the pseudogap regime, d-SC is the d-wave superconducting state, M is the metallic state, NFL is the non-Fermi liquid state, SG is the spin glass regime, and CO is the charge-ordered state.

pairing symmetry in the cuprates. For example, the d-wave symmetry implies that there are nodes in k-space where the gap vanishes even at zero temperature and where the order parameter changes sign as a function of momentum. When d-wave symmetry is considered within BCS theory, eq. 3.1 becomes $2\Delta/k_BT_c = 4.3$ [62], which is somewhat closer to experimental values. Still, as BCS theory relies on electron-phonon coupling to mediate pair formation it ultimately cannot provide an accurate description of unconventional superconductivity. If BCS theory were extended to include electron-electron interactions due to spin excitations, however, it is possible that the theory could successfully describe unconventional superconductors such as the cuprates and iron-based superconductors.

An unresolved issue is the importance of the pseudogap, a region of the cuprate phase diagram where a depletion of spectral weight at the Fermi level is observed at temperatures far above T_c. The pseudogap region is located between the antiferromagnetic insulating regime and the superconducting dome, and resembles the superconducting state in many respects. Basic questions about the pseudogap remain unanswered, such as whether it is a precursor to superconductivity or

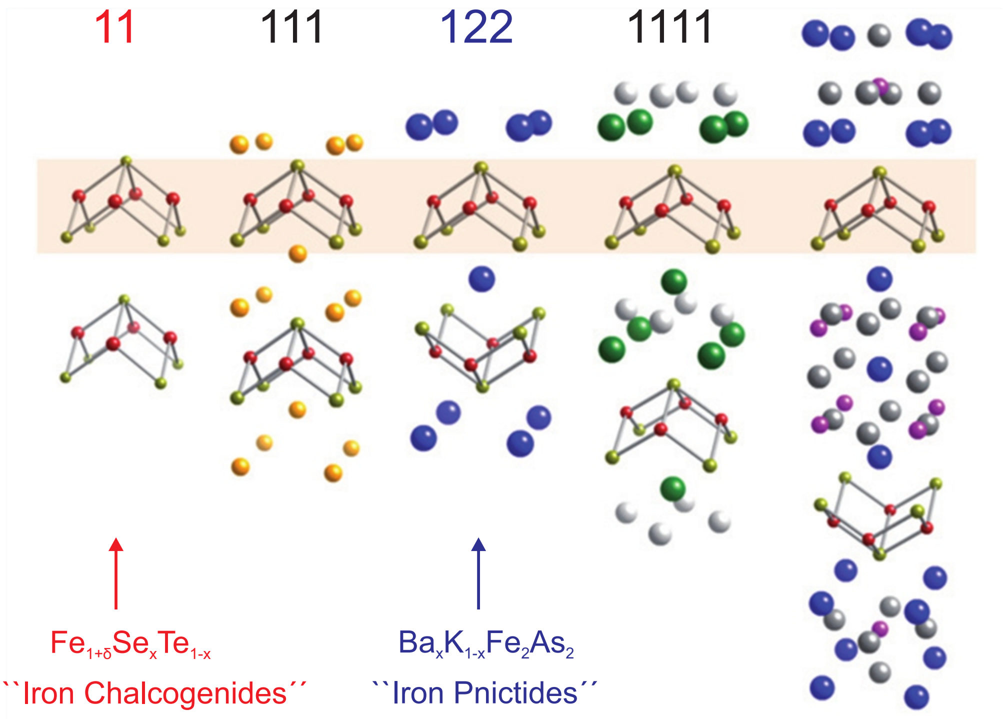

Figure 3.2: [64] Five crystal structures of iron-based superconductors with the common Fe-A layer highlighted, where A (lime green) is typically As, P, Se, or Te, and the Fe (red) spins are arranged anti-ferromagnetically.

rather a competitor [63].

3.4 Iron-based superconductors

In the following, I introduce the iron-based superconductors. For further reading see, e.g., the review by Paglione and Green [64], from which figs. 3.2, 3.4 and 3.5 have been adapted.

Like the cuprates, the iron-based superconductors are layered materials. Instead of Cu-O, the iron-based superconductors contain layers of Fe-A, where A is a pnictogen such as As or P, or a chalcogen such as Se or Te. Five separate crystal structures have been identified and these are illustrated in fig. 3.2. The focus in the body of this work is on the families $Fe_{1+\delta}Se_xTe_{1-x}$ and $Ba_xK_{1-x}Fe_2As_2$, which, for ease of reading, I will refer to as the iron chalcogenides and the iron pnictides, respectively. Please note that these terms will also sometimes be applied to closely related compounds.

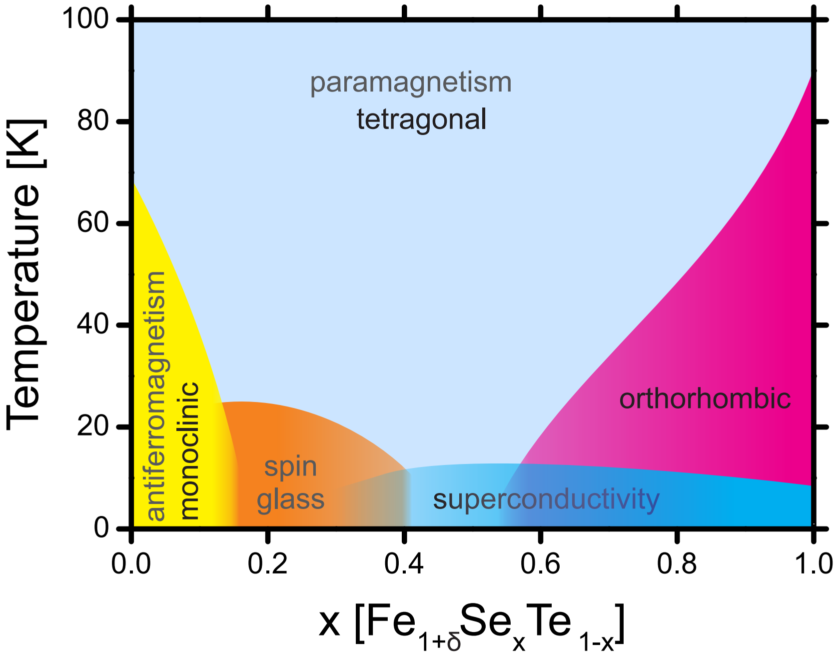

Figure 3.3: Electronic and structural phase diagram of the iron chalcogenides. Superconductivity exists in both the tetragonal and orthorhombic phases. The diagram has been constructed from information drawn from [65–71], and [72].

In fig. 3.3, a structural and electronic phase diagram of the iron chalcogenides is shown. The phase diagram was created using data from several sources, with the most weight given to Katayama *et al.* [65] and Mizuguchi *et al.* [66]. Many iron-based superconductor "parents" (i.e. undoped precurser compounds) must be doped for superconductivity to emerge. For example, from fig. 3.3 we can see that the iron chalcogenides are superconducting between $\sim x = 0.3$ and $x = 1$. While the parent compounds of the cuprates are anti-ferromagnetic Mott insulators, the parent compounds of the iron-based superconductors are metallic. On cooling down, the parent compounds of both material classes undergo a magnetic transition accompanied by a structural phase transition from tetragonal to orthorhombic lattice symmetry. In the case of the iron pnictides, the spin structure of the Fe lattice is anti-ferromagnetic in the out-of-plane direction. The origin of this magnetic order is not clear, but is thought to be at least partially driven by (π, π) nesting of electron-like and hole-like Fermi surface pockets [73, 74].

Parent compounds of iron-based superconductors can be turned superconducting through several routes, including electron doping, hole doping, and isovalent substitution. In the case of the iron chalcogenides, isovalent substitution of Te with Se turns the material superconducting. In the case of the iron pnictides, hole doping via substitution of Ba with K has produced a T_c of 38K [75] – the highest to

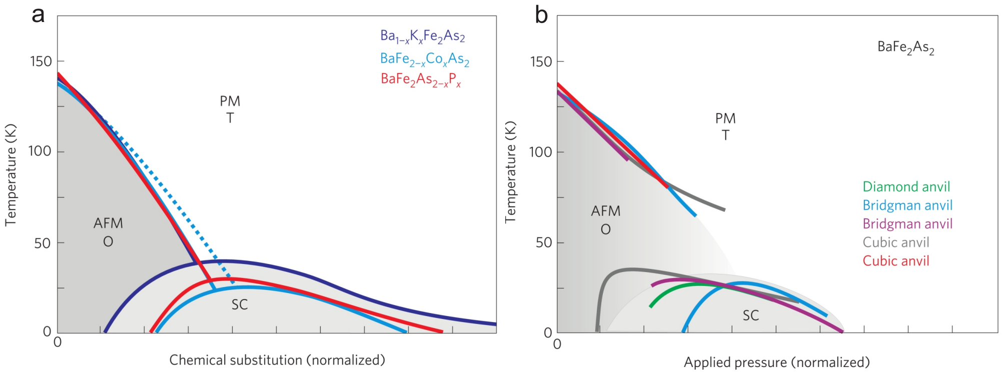

Figure 3.4: [64] (a) The parent compound of the iron pnictides is not superconducting, but superconductivity can be induced via hole-doping, electron-doping, or isovalent substitution. (b) A similar phase diagram can be produced through the application of pressure.

date. Electron doping, such as substitution of Fe with Co or Ni, has so far produced a maximum T_c of 22K [76]. Isovalent substitution of As with P [77] or Fe with Ru [78] has produced maximum T_c's of 30K and 20K, respectively. In fig. 3.4 (a), a schematic representation of hole, electron, and isovalent doping, respectively, is shown, all of which produce similarly sized superconducting domes. In fig. 3.4 (b), pressure is applied to the undoped iron pnictide, producing a somewhat smaller superconducting dome. Whereas superconductivity in the cuprates is extremely sensitive to doping in the Cu-O plane [79, 80] (and superconductivity can easily be destroyed by in-plane doping) the iron-based superconducters do not seem to be particularly sensitive to analogous doping in the Fe-A plane (as illustrated by the above examples).

With the several possibilities to induce superconductivity established – e.g. electron, hole, or isovalent doping, or the application of pressure – the question arises what mechanism / pairing mediator underlies superconductivity in the iron-based superconductors. Similarities in the phase diagrams between the iron-based superconductors, cuprate superconductors, organic superconductors, and heavy fermion superconductors suggest a similarly unconventional superconductivity in each class of material. Although the specific unconventional pairing mediator for the iron-based superconductors has not been definitively proved, the general consensus seems to point towards magnetic spin fluctuations [81, 82].

A detailed picture of the electronic structure of iron-based superconductors emerges through band calculations complimented by experimental verification. In the iron pnictides, the electronic states at the Fermi level are almost exclusively Fe 3d states with a small amount of hybridisation with As 4p states (as determined from hard X-ray photoemission experiments [83]). Crystal field considerations suggest

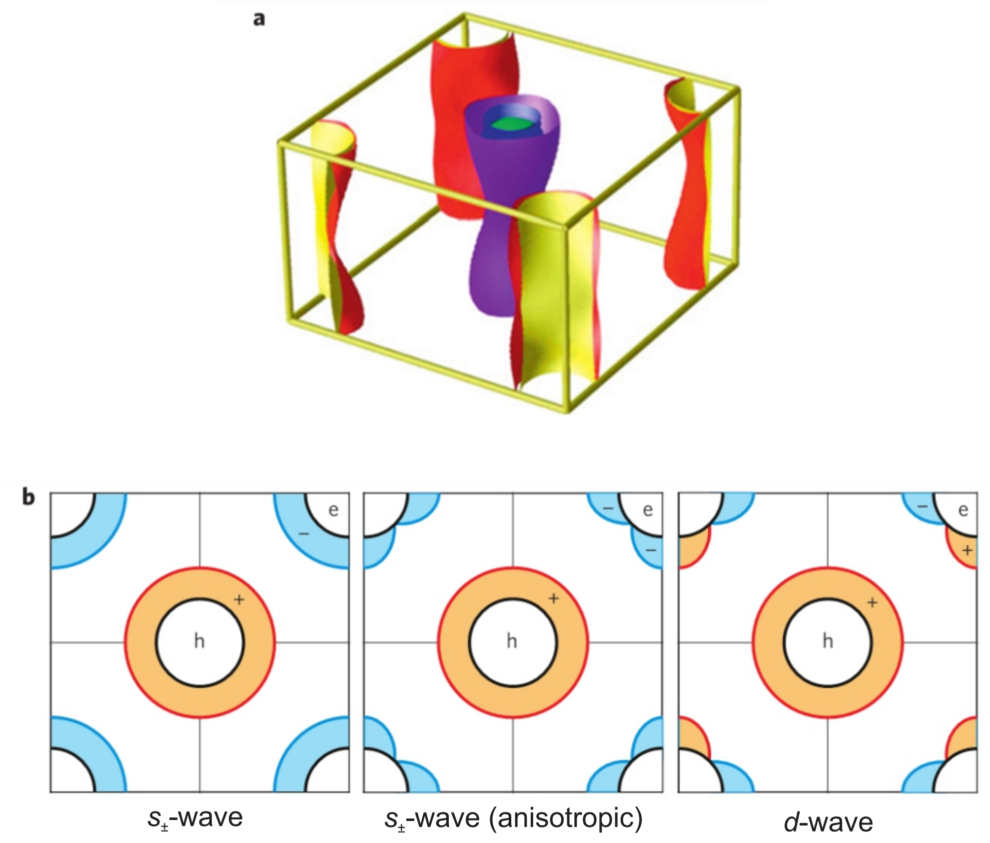

$s_{\pm}$-wave $s_{\pm}$-wave (anisotropic) *d*-wave

Figure 3.5: [64] (a) Schematic representation of the Fermi surface of the iron pnictides, with two or three hole-like pockets around the Γ-point and two electron-like Fermi surface sheets around the M-point. (b) An early schematic representation from the literature of the k-dependence of the superconducting gap on the hole and electron Fermi surfaces for three different pairing scenarios.

that these states have a d^6 configuration and should give rise to at least four hole bands at the Fermi level. Local density approximation (LDA) calculations return a band structure with four or five bands crossing the Fermi level [84].

In fig. 3.5 (a), a schematic representation of the Fermi surface of the iron pnictides is shown, with two or three hole-like pockets around the Γ-point and two electron-like Fermi surface sheets around the M-point. Due to interlayer coupling, the Fermi surface of the iron-based superconductors is not as two dimensional as that of the cuprates. In fig. 3.5 (b), schematic representations from the literature of the k-dependence of the superconducting gap on the hole and electron Fermi surfaces are shown for the most likely pairing symmetries: s-wave, anisotropic $s_{\pm}$-wave, and d-wave. All three scenarios show a sign change of the order parameter between the electron and hole bands, which would be unavoidable in the case of a spin fluctuation mediated superconductivity [82].

Questions remain, however, as to the role of electron-phonon coupling and other pairing mediators in iron-based superconductors. In particular, it has been suggested that large orbital fluctuations could be induced by relatively small electron-phonon coupling, which could dominate pairing mediation in materials such as the iron pnictides [85]. The existence of this additional mechanism would go some ways towards explaining the diversity of gap structure among iron-based superconductors, and clear up some inconsistencies in the spin fluctuation mediated picture. In the case of orbital fluctuation mediated superconductivity one would expect not an $s_{\pm}$-wave but rather a more conventional "s_{++}-wave" order parameter.

The role played by impurity scattering differs between conventional and unconventional superconductors, but is certainly important in the iron-based superconductors [63]. In conventional s-wave superconductors, the presence of non-magnetic impurities causes an initial sharp drop to the transition temperature and gap size (compared to the impurity-free superconductor) but the drop will quickly level off for higher concentrations of impurities [86]. If magnetic impurities are added then the initial drop will be equally sharp but will increase with increasing concentration until superconductivity is destroyed [87].

Anderson [88, 89], Abrikosov and Gor'kov [90], and later contributors [91–93] have explained these observations using symmetry arguments. Assuming purely elastic scattering, a scattering event that preserves the time-reversal invariance of the BCS ground state, such as scattering off a non-magnetic impurity potential, will barely affect gap size or T_c. Except for an initial drop due to the reduction of the length of the mean free path, marginal addition of non-magnetic impurities will not have any large effect. In the case of a magnetic impurity, however, time-reversal symmetry is broken and scattering will break the time-reversal invariance of the Cooper pair, destroying it. As each marginal magnetic impurity acts as an additional pair-breaker, a small amount will suffice to completely suppress superconductivity. A material with pair-breaking scattering centers will also support quasiparticle excitations within the superconducting gap [94].

In the case of unconventional superconductors, magnetic and non-magnetic scatterers are no longer clearly differentiated in their effects. In general, magnetic impurities will act as strong pair-breakers for all spin-singlet superconductors, including, e.g., for both s-wave and d-wave. However, in a d-wave superconductor the order parameter changes sign as a function of momentum, with nodes at the points where the sign changes. Because of this, potential scattering centers can induce scattering between k-space locations of different order parameter sign while not affecting the spin of the electron, breaking time-reversal symmetry. Thus, non-

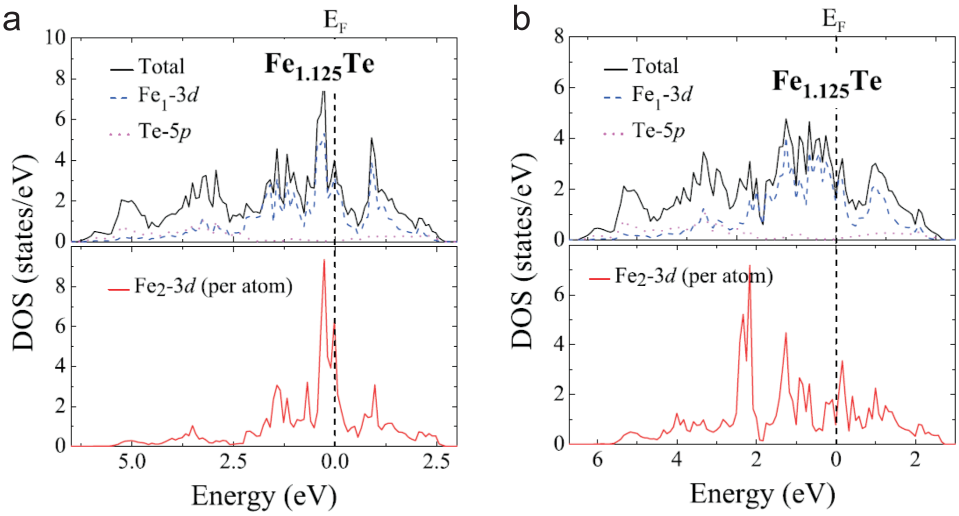

Figure 3.6: [96] Calculated partial and total electronic DOS for (a) nonmagnetic and (b) magnetic impurities (Fe_2), in parent iron chalcogenide $Fe_{1.125}Te$.

magnetic impurities in a d-wave superconductor will act as pair-breakers. In contrast, a magnetic impurity in the same situation will induce a second sign change, thereby preserving time-reversal symmetry. In general then, a scattering path for which a magnetic scatterer would be pair-breaking will not be pair-breaking for a non-magnetic scatterer and vice versa [82].

In addition to the foregoing considerations (which apply to single-band superconductors) we must also take into account the multi-band nature of unconventional superconductivity in iron-based superconductors. In multi-band superconductors, not only intraband but also interband scattering must be considered. Studies of multi-band superconductor MgB_2 suggest that (at least in this material) both interband pairing interactions and scattering are small [95]. In MgB_2, non-magnetic impurities appear to suppress superconductivity in the same way that magnetic impurities do in single-band superconductors, and only interband scattering seems to have pair-breaking character.

In the iron pnictides, the bands at the Fermi level all have d-orbital character [97], and it is believed that the pairing interaction is primarily interband, and that intraband pairing is weak [82]. Furthermore, the most likely pairing symmetry is believed to be one with a sign change of the order parameter occuring for scattering between bands, but not within bands, i.e. $s_{\pm}$-wave.

Impurity states are expected to vary depending on the superconducting order parameter and whether the impurities are magnetic or nonmagnetic [96]. Theoretical calculations of the DOS contributions from magnetic and nonmagnetic Fe impurities in a parent iron chalcogenide are reproduced in fig. 3.6. We can see that while nonmagnetic impurities tend to add states close to the Fermi energy, the states contributed by magnetic impurities are mainly situated well inside the valence band. In the iron pnictides, highly anisotropic quasiparticle scattering on spatially extended impurity states has been found to produce an electronic nematicity [98]. In general, the effect of impurities, whether magnetic or non-magnetic, on the transition temperature is strongly dependent on the strength of the impurity potential. In the weak scattering limit, non-magnetic impurities can lead to pair-breaking only via interband scattering (as this scattering does not break time-reversal symmetry). In the weak limit, high concentrations of impurities will drastically reduce T_c. However, in the strong scattering limit it has been argued that large concentrations of non-magnetic impurities will not affect T_c, as time-reversal symmetry is preserved [99, 100]. Only when the intraband and interband scattering potentials are equal will T_c be strongly suppressed, as the interband pair-breaking effect is amplified by the corresponding intraband effect. On the other hand, magnetic impurities in the weak scattering limit have been found to be pair-breaking for intraband scattering, while being pair-preserving for interband scattering, which is the opposite of what has been found for non-magnetic impurities [101].

3.4.1 Iron chalcogenides

In 2008, a superconducting transition was found (first in α-phase [102], later also β-phase [71, 103]) of the well-characterized [104, 105] iron chalcogenide FeSe, with a T_c^{onset} of 13K and T_c^{zero} of 8.5K. α-FeSe has a layered, tetragonal, PbO-type structure which supports a quasi-2D superconductivity.

The iron chalcogenides are well suited for STM investigation due to their well-defined and weakly-bound cleavage plane which allows for *in-situ* sample preparation in cryogenic vacuum. The cleaved surface is atomically flat and unpolar, and neither LEED [106, 107] nor ARPES [107] experiments have found any indication of surface reconstruction or the formation of surface states.

The phase diagram of the iron chalcogenide family has been studied extensively [108], and maximum overall transition temperatures of $T_c^{onset} \sim 36.7$K and $T_c^{zero} \sim 21$K have been achieved, in β-$Fe_{0.01}Se$, through application of high pressure ($\sim$ 8.9GPa). Between $\sim$ 8.9Gpa and $\sim$ 38GPa the crystal structure undergoes a partial phase transition to hexagonal lattice symmetry and T_c decreases with increasing pressure. Above $\sim$ 38GPa the space between the Fe_2Se_2 layers collapses and the system undergoes a first order phase transition to a semiconducting, non-magnetic hexagonal lattice [71]. In the absense of external mechanical pressure, substitution of around half of the Se content with Te seems to yield the highest T_c. With this composition ($FeSe_{0.5}Te_{0.5}$), a maximum T_c of $\sim$ 14K has been achieved, with relatively little difference between onset and zero resistivity transition temperatures.

Pure iron chalcogenide crystals can be difficult to grow, and as-grown samples often contain interstitial excess Fe. In the following, I will summarize some of the recent literature on the consequences of excess Fe and other impurities for the properties of iron chalcogenides. In particular, findings from several recent theoretical [96, 109] and experimental [103, 110–113] publications will be briefly reviewed.

Supercell density functional theory (DFT) calculations of α-$Fe_{1.125}Te$ suggest that excess Fe atoms donate charge to the FeTe layers with a valence close to Fe^{+}, i.e. each excess Fe atom donates one electron [96]. The excess Fe appear to have a strong tendency towards magnetism and should act as pair breaking centers in the superconducting state. The results of these calculations indicate further that the excess Fe 3d DOS contribution at the Fermi level easily exceeds the Stoner criterion ($\rho(E_F)I > 1$, where $\rho(E_F)$ is the DOS per atom and spin at the Fermi level and I is the Stoner parameter, which for Fe is typically between 0.7 and 0.9eV). The DOS contribution of excess Fe atoms at the Fermi level was calculated to 6.2 states per eV and spin-integrated atom, and it was found that when allowing the excess Fe (but not the stoichiometric Fe) to spin polarize the total energy would be reduced by 48.9meV and a pseudogap would open up with its minimum near the Fermi level. In this case, the DOS at the Fermi level is reduced to 0.8 states per eV and excess Fe atom. The magnetic moment of an excess Fe atom is calculated to be $2.5\mu_B$.

Early DFT calculations of FeSe and FeTe showed that the iron chalcogenide Fermi surface (FS) is similar to those of other known iron-based superconductors [114]. This was later confirmed by photoemission experiments [115]. As is the case with other iron-based superconductors, superconductivity in the iron chalcogenides is very sensitive to stoichiometry [103] and cannot be understood in the standard electron-phonon picture [114, 116, 117]. The observation of spin resonance below T_c and the enhancement of spin fluctuations in the proximity of the transition temperature suggest that the superconducting pairing mechanism is mediated by spin fluctuations [118, 119]. While undoped parent FeSe becomes superconducting at low temperatures, FeTe does not and instead undergoes a structural and magnetic phase transition to antiferromagnetism (AFM). It has been found that in FeTe the AFM wave vector can be tuned through the addition of excess Fe, resulting beyond $\delta = 0.076$ in a transition from a commensurate to an incommensurate AFM order [120]. On the basis of this and other evidence it has been surmised that the mechanism producing magnetism in the $Fe_{1+\delta}Te$ system is different from the Fermi surface nesting which produces spin density wave (SDW) order in the iron pnictide parent compounds [110]. In fact, in the $Fe_{1+\delta}Te$ system no FS nesting or SDW gap has as yet been observed [115, 121]. Several models proposing to explain the unusual magnetic order in the $Fe_{1+\delta}Te$ system have recently been put forward [122–125]. Liu *et al.* [110] have suggested that the effects of excess Fe in the iron chalcogenides are key to understanding the superconducting pairing mechanism in iron-based superconductors. In a wide ranging study including resistivity, Hall coefficient, magnetic susceptibility, and specific heat measurements, they conclude that, in the iron chalcogenides, excess Fe leads both to a suppression of superconductivity and to a weak charge-carrier localization due to magnetic coupling between the excess Fe and the stoichiometric Fe sheets, which favors short-range magnetic order. In non-superconducting $Fe_{1+\delta}Te$, an elevated level of excess Fe is found to cause an electronic evolution from a Fermi liquid to a weakly localized state [110]. In an electrical transport and magnetism study of $Fe_{1+\delta}Se_{0.5}Te_{0.5}$, Rößler *et al.* [111] come to similar conclusions. Their findings are consistent with a suppression of superconductivity and electronic localization due to magnetic coupling between interstitial excess Fe and stoichiometric Fe. In particular, their resistivity data shows a transition from a metal-like behavior to an insulator-like behavior, characterized by a $\rho \propto \log \frac{1}{T}$ divergence, when the excess Fe content is increased from $\delta = 0.04$ to $\delta = 0.09$. Both Rößler and Liu cite this insulator-like divergence in support of a magnetic impurity and / or disorder-driven electronic localization interpretation of system behavior. Nonlinear AC susceptibility measurements provide evidence for the existence of a magnetic / superconducting phase separation at high concentrations of excess Fe [111].

The LDOS consequences of magnetic and non-magnetic impurities in a generalized iron-based superconductor were recently investigated with a tight-binding model (the two-orbital exchange-coupling model [126]) by Tsai *et al.* [109]. They note that in conventional, nodeless superconductors pair-breaking magnetic impurities have long been known to induce in-gap bound states which are localized near the impurity and to have the potential, once magnetic interactions become stronger than the condensation energy, to strongly influence the ground state properties of the system [127]. In their study, the iron-based superconductors are assumed to have either a standard s-wave pairing symmetry or the so-called sign changing s-wave ($s_{\pm}$) symmetry, where the relative sign of the superconducting order parameter changes between the hole and electron pockets on the Fermi surface. Based on their calculations, Tsai *et al.* come to the conclusion that $s_{\pm}$ symmetry is more likely. In the case of a non-magnetic impurity in an $s_{\pm}$-wave iron-based superconductor, they predict the existence of two separate in-gap bound states, which are created due to the sign-reversal effect. Magnetic impurities, which break time-reversal symmetry, are predicted to support only a single in-gap bound state. Under an increasing large magnetic moment, their model predicts that the ground state of the system should eventually undergo a quantum phase transition from a spin-unpolarized to a spin-polarized state.

3.4.2 Iron pnictides

Bulk-superconducting $Ba_xK_{1-x}Fe_2As_2$ was first synthesized in 2008 [75], and has since been characterized with a variety of techniques, including ARPES, neutron scattering, μSR and magnetic force microscopy [128–131]. The T_c of this material has been reported to be $\sim$ 32K in the underdoped regime, and up to $\sim$ 37K at optimal doping [131]. A mesoscopic phase separation into magnetically ordered (antiferromagnetic) and non-magnetic (normal, then superconducting) regions of several tens of nanometers in size has been observed below about 70K and suggested to be an intrinsic property of the material [129, 131, 132]. Anisotropy in magnetic penetration depth (λ) and in the upper critical field (H_{c2}, which is reported to be about 75T in $Ba_{0.6}K_{0.4}Fe_2As_2$ [133]), defined as $\gamma_\lambda = \lambda_c/\lambda_{ab}$ and $\gamma_{H_{c2}} = H_{c2}^c/H_{c2}^{ab}$, shows opposite evolution in temperature below T_c [132]. Specifically, γ_λ is found to increase with decreasing temperature while $\gamma_{H_{c2}}$ is found to decrease [134, 135]. Based on these findings and on the existence of an inflection point in the temperature evolution of in-plane magnetic penetration depth ($\lambda_{ab}(T)$) at $T \sim$ 7K, Khasanov *et al.* draw a comparison with double-gapped MgB_2 and contend that underdoped $Ba_xK_{1-x}Fe_2As_2$ also has two superconducting gaps [132, 136]. Based on their observations, they infer the existence of two gaps of size $\Delta_1 = 9.1$meV and $\Delta_2 = 1.5$meV, respectively.

Another μSR study, conducted by Takeshita and Kadono [136], likewise shows evidence for the existence of two superconducting gaps in $Ba_xK_{1-x}Fe_2As_2$. Partially on the basis of large observed gap parameters ($\frac{2\Delta}{k_BT_c} \gg 3.53$), the authors contend that superconductivity in this material is characterized by a stronger coupling of pairing bosons to the relevant d electron bands than that found in some other iron-based superconductors, as expressed in the larger anisotropy of the superconducting order parameter. The hole-doping in this material is contrasted with the electron-doping in materials such as $LaFeAsO_{1-x}F_x$ and $CaFe_{1-x}Co_xAsF$, and suggested as a possible cause of the stronger coupling.

3.5 Samples

3.5.1 $Fe_{1.04}Se_{0.28}Te_{0.72}$

In this work, one iron chalcogenide crystal with a significant amount of excess Fe has been investigated, $Fe_{1.04}Se_{0.28}Te_{0.72}$. The crystal was grown with the Bridgman method from high purity (4N) Fe pieces, Te lump, and Se shot, by T. J. Liu in the group of C. T. Lin [137]. SQUID measurements show a T_c of around 14K, but the crystal is reported to have a superconducting volume fraction of only ~ 1%. In fig. 3.7 (a), a scanning electron microscopy (SEM) image of the crystal is shown, along with the results of an energy dispersive X-ray spectroscopy (EDX) chemical composition characterization.

3.5.2 $Fe_{1.00}Se_{0.4}Te_{0.6}$

The second iron chalcogenide sample investigated in this work, $Fe_{1.00}Se_{0.4}Te_{0.6}$, has very little excess Fe and a much higher superconducting volume fraction than the $Fe_{1.04}Se_{0.28}Te_{0.72}$ sample. Single crystal $Fe_{1.00}Se_{0.4}Te_{0.6}$ samples were grown in self-flux from high purity components: %99.99 Fe, %99.999 Se and %99.999 Te. Se and Te were further treated by zone melting to reduce the number of oxide impurities. The growth of single crystals was performed in evacuated double quartz ampoules at temperatures between 1000 and 1100°C. In a final step, the samples were treated at 410°C for 100 hours followed by quenching in ice water. The crystal was grown by V. Tsurkan [138]. An SEM image of the crystal is shown in fig. 3.7 (b). The composition of the finished samples was characterized with EDX. The phase content of the samples was analyzed via X-ray powder diffraction (CuK_α radiation, $\lambda = 1.540560$Å) on crushed single crystals using a STADI-P powder diffractometer (STOE & CIE) with a position-sensitive detector. The composition is close to optimal doping and the crystal has a T_c of about 14K.

3.5.3 $\mathbf{Ba_{0.68}K_{0.32}Fe_2As_2}$

An optimally doped iron pnictide crystal, $Ba_{0.68}K_{0.32}Fe_2As_2$, has also been investigated. The crystal was grown in Sn-flux in an Al_2O_3 crucible, from pure elements Ba, K, Fe, and As. The crucible was placed under flowing Ar and heated at a rate of 5°C/min to a maximum of 1100°C. After 2-4 hours, the temperature was decreased by 5°C/h down to 550°C, which was then maintained for another 2 hours before cooling down to room temperature. The crystal was grown in the group of C. T. Lin and was characterized by G. L. Sun, *et al.* [139, 140]. Electrical resistivity data show a sharp superconducting transition temperature at $T_c \sim 38.5$K. An SEM image of the crystal is shown in fig. 3.7 (c). The material consists of alternating layers of Ba_xK_{1-x} and Fe_2As_2. Unlike the iron chalcogenides, it has no natural cleavage plane, and cleaving results in a half layer of Ba_xK_{1-x} being left at the surface. Because of this, this material was more difficult to characterize in STM than the iron chalcogenide samples.

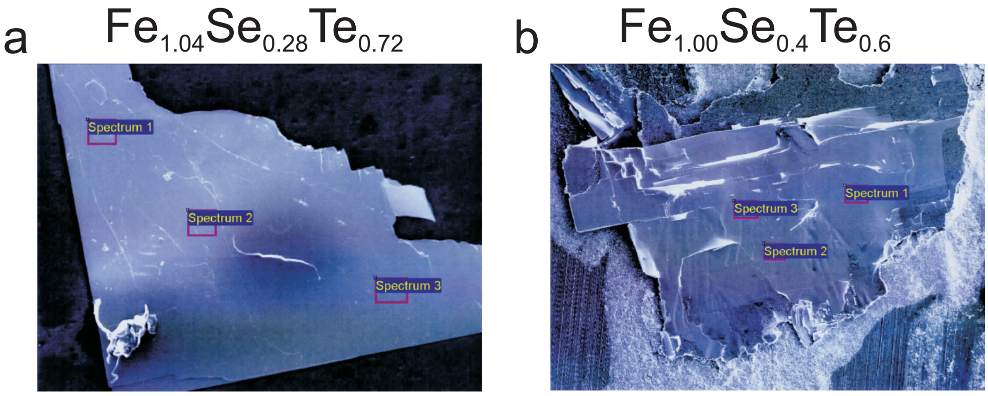

Spectrum	In stats.	Fe	Se	Te
Spectrum 1	Yes	52.40	13.69	33.91
Spectrum 2	Yes	52.08	13.73	34.19
Spectrum 3	Yes	51.89	13.69	34.42
Mean		52.12	13.70	34.17
Std. deviation		0.26	0.02	0.25
Max.		52.40	13.73	34.42
Min.		51.89	13.69	33.91

Spectrum	In stats.	Fe	Se	Te
Spectrum 1	Yes	49.73	20.55	29.72
Spectrum 2	Yes	49.63	19.85	30.52
Spectrum 3	Yes	49.60	19.38	31.02
Mean		49.66	19.93	30.42
Std. deviation		0.07	0.59	0.66
Max.		49.73	20.55	31.02
Min.		49.60	19.38	29.72

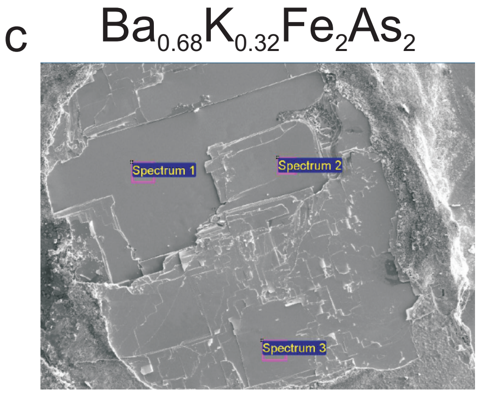

Spectrum	In stats.	K	Fe	As	Ba
Spectrum 1	Yes	6.70	38.64	41.18	13.48
Spectrum 2	Yes	6.49	39.38	40.82	13.30
Spectrum 3	Yes	6.42	39.65	40.54	13.38
Mean		6.54	39.22	40.85	13.39
Std. deviation		0.15	0.53	0.32	0.09
Max.		6.70	39.65	41.18	13.48
Min.		6.42	38.64	40.54	13.30

Figure 3.7: SEM images of (a) $Fe_{1.04}Se_{0.28}Te_{0.72}$, (b) $Fe_{1.00}Se_{0.4}Te_{0.6}$, and (c) $Ba_{0.68}K_{0.32}Fe_2As_2$, along with the results of EDX characterizations performed on each crystal.

Chapter 4

Scattering on Monoatomic Impurities

In which I investigate the role of impurities in the iron chalcogenides, with a focus on the relationship between impurities, electronic structure, and superconductivity.

4.1 Introduction

In general, the properties of the iron chalcogenides are known to be sensitive to the presence of impurities, in particular excess Fe [103]. It has even been suggested that understanding the interplay between impurities and superconductivity in this material is key to better understanding the underlying mechanism of iron-based superconductivity [110]. In the following, I present a comparitive SI-STM study performed on two crystals, one with many impurities, $Fe_{1.04}Se_{0.28}Te_{0.72}$, and one with few impurities, $Fe_{1.00}Se_{0.4}Te_{0.6}$.

4.2 Location

In fig. 4.1 (a), a side view of the iron chalcogenide crystal structure is shown with its natural cleavage plane. In an STM image, after cleaving, one would expect to see an image of the atomic lattice illustrated in fig. 4.1 (b). In fig. 4.1 (c), an actual STM image of $Fe_{1.04}Se_{0.28}Te_{0.72}$ taken at -50mV is shown. In areas clear of impurities one can see a quadratic lattice, representing the top-most layer of chalcogens. The chalcogen surface is believed by us to be atomically flat and consist entirely of the elements selenium and tellurium, which appear darker

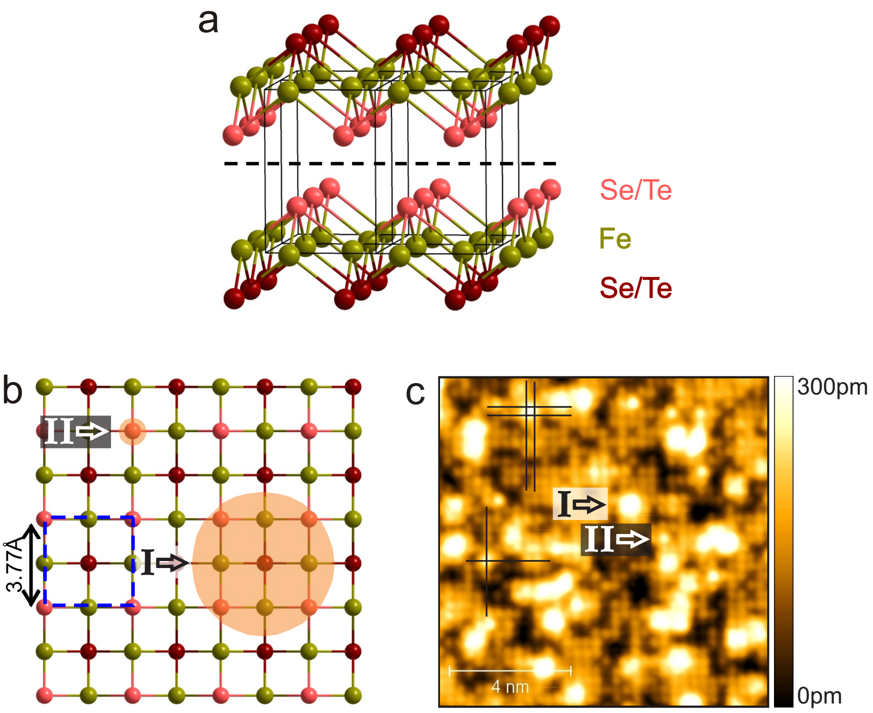

Figure 4.1: (a) Sideview of the atomic lattice, showing the natural cleavage plane of the iron chalcogenide crystal structure. (b) Schematic representation of the crystal structure, as viewed from above. Green dots represent the first Fe sheet, while chalcogen atoms are represented in pink or red, according to their position above or below the Fe sheet, respectively. The apparent impurity sizes and positions are represented with orange circles. (c) Topographic image of $Fe_{1.04}Se_{0.28}Te_{0.72}$, taken with bias $V = -50$mV and current $I = 0.8$nA, with two impurity types indicated, as well as the impurities' lattice positions relative to the surface chalcogens.

and brighter, respectively, due to their differing ionic radii [141]. STM analysis of several different iron chalcogenide compositions and comparison with energy dispersive X-ray spectroscopy (EDX) data supports this interpretation.

In fig. 4.1 (c), impurities are visible on the surface chalcogen lattice which will be considered in the following analysis. The impurities, which appear higher than their surroundings in the image, are easily placed into two catagories based on size and lattice position, which I will call type I and type II. In fig. 4.1 (b), the size and lattice position of the two impurity types are indicated in relation to the crystal lattice. The type I impurities appear to occupy a lattice position in the center of four surface chalcogens and to take up space in the image comparable to all four of its neighbors. The type II impurities, in contrast, appear to occupy the same lattice position as the surface chalcogens and to be of roughly comparable size to their neighbors, albeit significantly higher / brighter.

The position of the type I impurities in this analysis, situated between (and slightly above) four surface chalcogens, is consistent with previous reports [96, 110]. This position also coincides with the vertical axis along which the chalcogen atoms at the bottom of the first layer reside. The chalcogens at the surface are represented in pink while the chalcogens at the bottom of the first layer are represented in red. In the STM image in fig. 4.1 (c) only surface chalcogens are expected to be visible, but the type I impurites appear at the expected position of a subsurface chalcogen while type II impurities appear at the expected position of a surface chalcogen. Due to their position and large size in the image it is more or less clear that the type I impurities are located on top of the sample surface. However, for the type II impurities, due to the symmetry of the crystal structure multiple geometric interpretations of lattice position(s) are possible. A straightforward interpretation is that the type II impurities substitute for a surface chalcogen. Another interpretation is that the type II impurities occupy the same position as the type I impurities, but on the opposite side of the layer. In the latter interpretation, the type II impurities would only appear to occupy the position of a surface chalcogen because they are positioned along the same vertical axis.

4.3 Concentration

The foregoing considerations have been made with reference to an STM image taken at negative bias. If the bias is positive, however, the image looks significantly different. In fig. 4.2 (a), an STM image taken at +50mV is shown. In this image, of the two types of impurities, only type I can easily be seen. If a second image is taken over the same area with negative bias, as shown in fig. 4.2 (b), the apparent height of the type II impurities increases significantly. On the other hand, the apparent height of the type I impurities and surface chalcogens remains virtually unchanged. In fig. 4.2 (c), the negative bias image is subtracted from the positive bias image and the color scale is adjusted in order to accentuate the difference between the two. In the resulting image, several type II impurities are plainly visible. However, close inspection of the input images reveals that some type II impurities were obscured under type I impurities, and therefore are faintly visible but not plainly visible in the subtracted image.

Based on the foregoing analysis, a best estimate of the total number of defects in the 25×25nm field of view is about 195 type I impurities and 53 plainly visible type II impurities, along with an unknown quantity of type II impurities which are obscured from view. A roughly equal number of type I and type II impurities

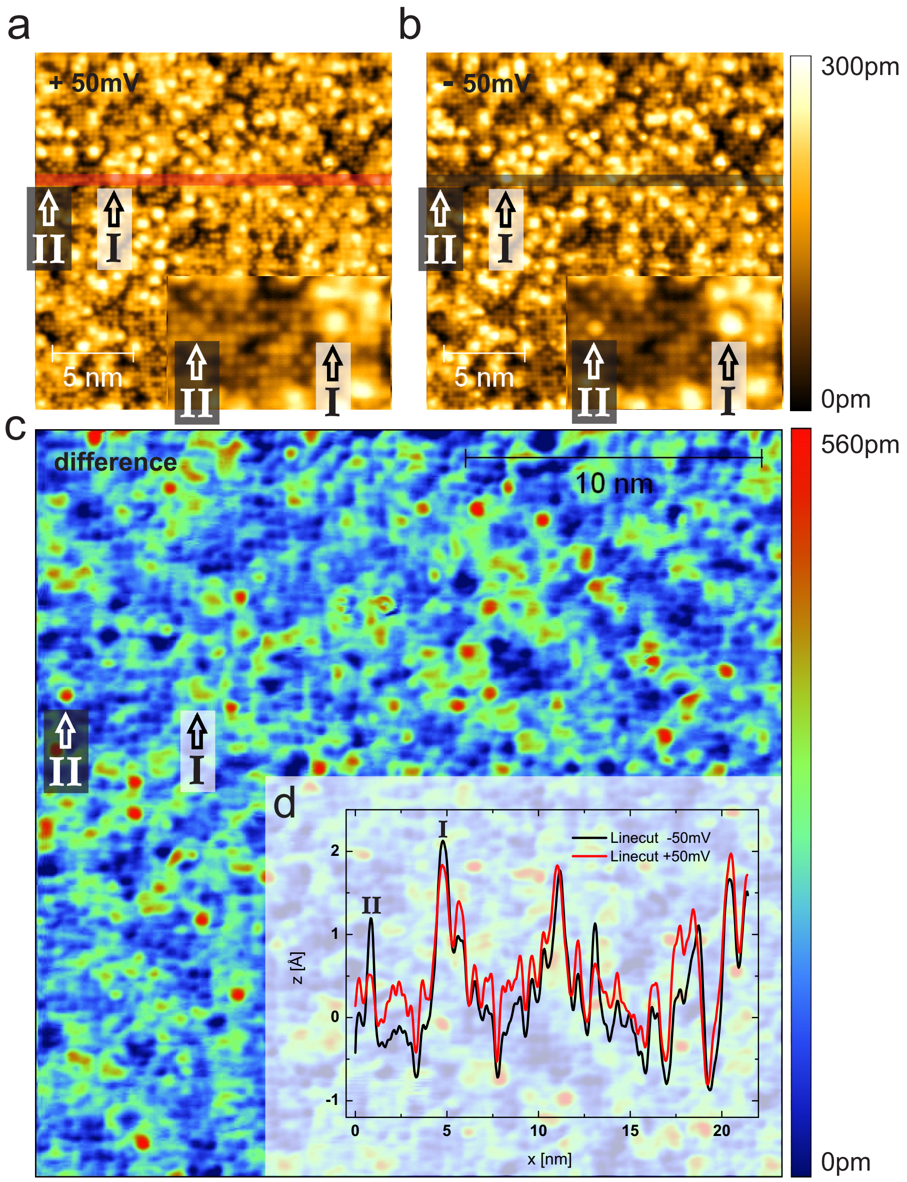

Figure 4.2: (a) 25×25nm topographic image of $Fe_{1.04}Se_{0.28}Te_{0.72}$, taken with bias $V = +50\text{mV}$ and current $I = 0.8\text{nA}$. (b) Topographic image of the same area with bias $V = -50\text{mV}$ and current $I = 0.8\text{nA}$. (c) Image of the difference between the two topographies, accentuated via adjustment of the color scale. (d) The line cuts taken at the positions indicated in (a) and (b) show the relative apparent height of type I and type II impurities for positive and negative bias, respectively.

in the field of view would be supportive of the second proposed identity of the type II impurities, namely that they occupy the same location as the type I impurities but on the reverse side of the layer. If the observed impurities are excess Fe atoms, further evidence supporting this interpretation would be the estimated ratio of excess Fe to stoichiometric Fe. According to EDX measurements, the sample contains around 4% excess Fe. Taking the unit cell size of 0.377nm and dividing it into the image size (25×25nm) gives us 66.3 rows and 66.3 columns, or 4397 surface chalcogen atoms, which correspond to 8795 stoichiometric Fe atoms. The estimated number of type I impurities in the same image is 195, or about 2.2% of the expected 8795 stoichiometric Fe atoms in the same field of view. The same amount of interstital excess Fe would be expected to exist on the reverse face of the first layer, yielding a total of 4.4% excess Fe, accounting for all of the EDX-detected excess Fe. If the observed impurities are indeed the excess Fe then we can conclude that there is likely little or no excess Fe clustering and that all of the excess Fe is likely located in the same lattice position, on either side of the Fe-A layer. EDX measurements of the examined samples have found only Fe, Se, and Te in detectable amounts, strengthening the interpretation that both impurity types are indeed excess Fe.

The change in relative apparent height with respect to the bias polarity indicates that the DOS of the type II impurities are asymmetric around the Fermi level, contributing a higher occupied DOS than unoccupied DOS, while the DOS contribution of the type I impurities appears to be roughly symmetric around the Fermi level. In terms of size, the type II impurities appear significantly larger in the image than do type I. In addition, the type II impurities appear slightly larger than the surrounding surface chalcogens, as revealed by close inspection of the positive-bias image. In fig. 4.2 (d), linecuts taken at the positions indicated in the topographies in fig. 4.2 (a) and (b) show the extent to which the bisected type II impurity is larger than the neighboring surface chalcogens, and also show the relative changes in apparent height between the two images.

4.4 Scattering

4.4.1 Dirty limit

Now that a topographic description of impurity species has been presented, it may be interesting to examine the consequences for local electronic structure in more detail. A spatial analysis of LDOS may also provide a more precise way to estimate the concentration of impurities, especially those type II impurities which were partially obscured by type I impurities in the topographic data. In fig. 4.3 (a), a topographic image of a 25×25nm map taken on $Fe_{1.04}Se_{0.28}Te_{0.72}$ is

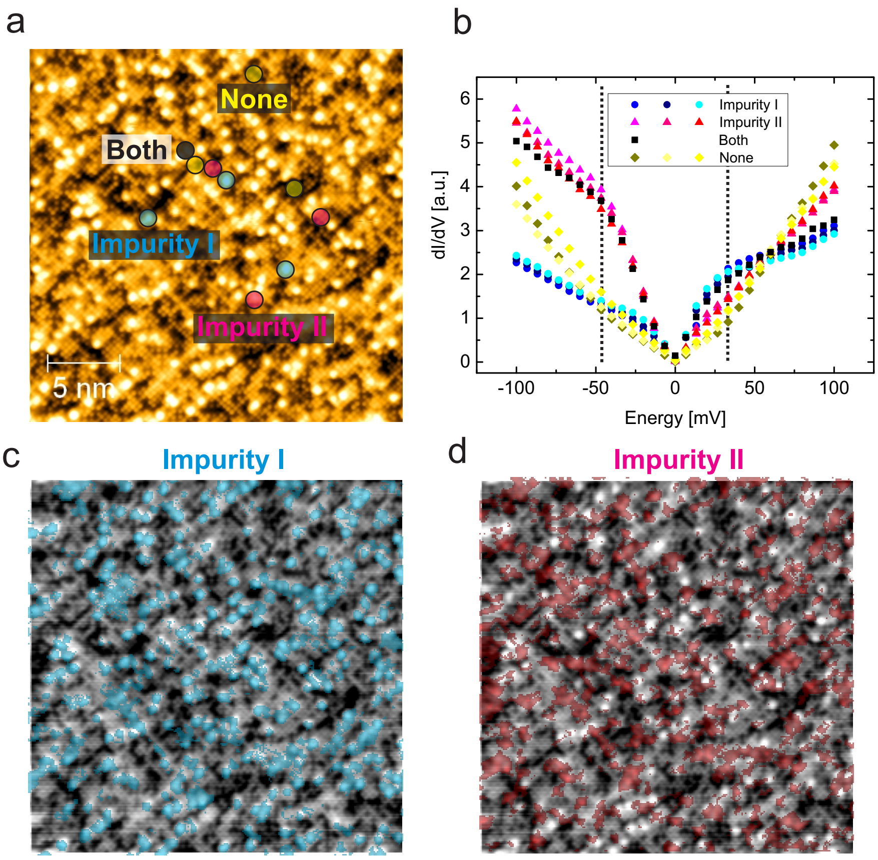

Figure 4.3: (a) Topographic image of a 25×25nm map taken on Fe$_{1.04}$Se$_{0.28}$Te$_{0.72}$, taken with bias $V = +50$mV and current $I = 0.8$nA.. The locations of characteristic spectra differing substantially from the mean, suspected to be influenced by nearby defects, are indicated. The spectra, averaged over an area with a 2pxl radius, are plotted in (b). The data was analyzed to map the locations of the defects based on the identification of characteristic spectral features, namely increased DOS around $+33.3$mV and -46.7mV for type I (blue) and type II (red) impurities, respectively. The results are plotted onto the map topography in (c) and (d), respectively.

shown. Several markers denote locations near only type I impurities (blue), only type II impurities (red), both types of impurities (black), or locations far from any impurities (yellow). Spectra averaged over an area with a 2pxl radius from each of the nine locations are plotted in fig. 4.3 (b). The most prominent spectral features which appear to be associated with type I and type II impurities are a raised LDOS centered around +30mV and −50mV, respectively, as indicated in the figure. In addition, the raised LDOS leads to a generally convex spectral form on both sides of the Fermi energy, which contrasts to the concave LDOS of the impurity-free areas. The largely non-overlapping LDOS contributions of type I and type II impurities on either side of the Fermi energy allow us to unambiguously identify their locations at each point of the map, even when overlapping. In fig. 4.3 (c) and (d), the elevated LDOS at the aforementioned energies are used to map the positions of the impurities in the map topography. This method of identifying the impurities also provides support for the interpretation that there are only two impurity types in the field of view. These maps suggest that the concentration of type II impurities is approximately equal to the concentration of type I, supporting the conclusions from the previous section.

4.4.2 Clean limit

In the following I compare a study done on an iron chalcogenide composition with few impurities, $Fe_{1.00}Se_{0.4}Te_{0.6}$, to the previous study. In contrast to the sample of composition $Fe_{1.04}Se_{0.28}Te_{0.72}$, this sample shows a large superconducting volume fraction and a clean superconducting gap. For this sample, I have conducted a similar analysis to that of the previous composition, with the difference that the energy scale has been significantly lowered in order to show details of the superconducting gap. The field of view selected for the $g(\mathbf{r}, E)$ map in this study did not have any obvious surface impurities. This means that only subsurface or otherwise inconspicuous impurities might have been captured in the measurement. In fig. 4.4 (a), a topographic image of a 50×50nm map taken on $Fe_{1.00}Se_{0.4}Te_{0.6}$ is shown. In the topography, several positions of suspected impurities (red) and impurity-free areas (yellow) are marked. The suspected impurities were identified by looking at the energy cut at the Fermi level. In fig. 4.4 (b), spectra averaged over an area with a 2pxl radius near the indicated locations are plotted. The most significant differences of the spectra from the suspected impurities to those taken at impurity-free areas at this energy scale are an increase in LDOS at the Fermi level, from zero to a finite value, and a slight increase in the LDOS on the occupied states side of the Fermi energy. Since the type II impurities in the previous study caused a similar increase in LDOS on the occupied states side of the Fermi energy (albeit at a much larger energy scale) it is tempting to suggest that the observed anomalous LDOS regions are being influenced by type II impurities, which I pre-

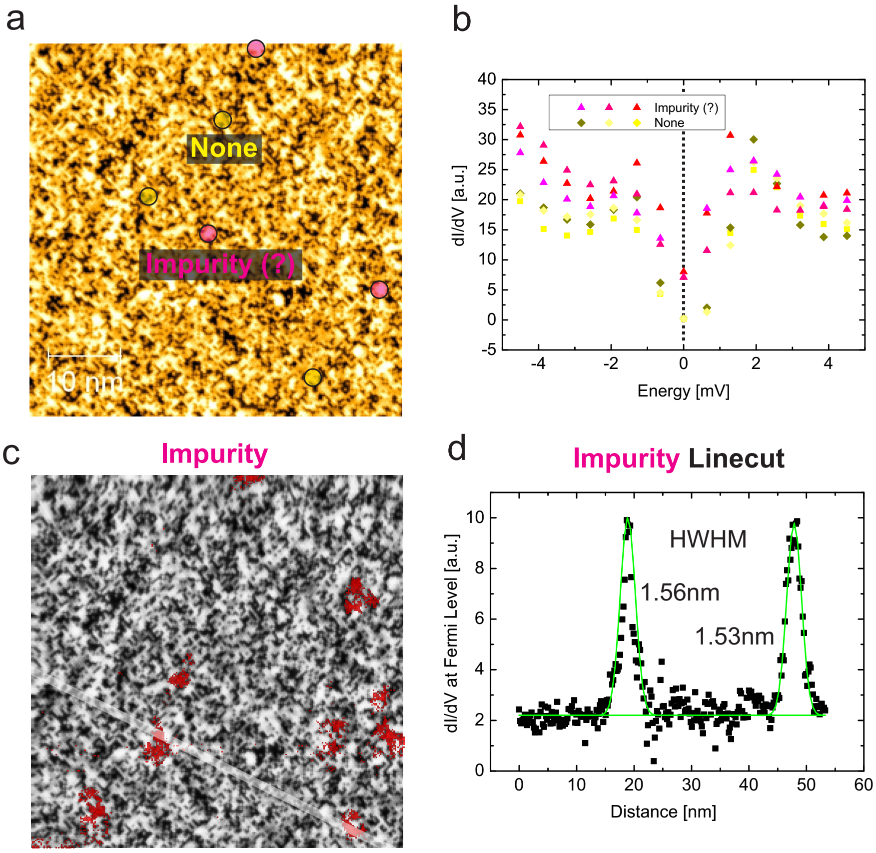

Figure 4.4: (a) Topographic image of a 50×50nm map taken on $Fe_{1.00}Se_{0.4}Te_{0.6}$, taken with bias $V = +50$mV and current $I = 0.8$nA.. Characteristic spectra near suspected impurities, as well as from apparently impurity-free regions, are plotted in (b). Based on the identification of the characteristic defect spectra, which was done using the energy cut at the Fermi level, the positions of suspected impurities, i.e. areas with elevated LDOS (red), are plotted onto the map topography in (c). In (d), a linecut across the Fermi level layer of the map is plotted, corresponding to the position indicated in (c), and showing the spatial extent of the elevated LDOS near the suspected impurities.

viously suggested were monoatomic subsurface excess Fe. In fig. 4.4 (c), areas of elevated LDOS at the Fermi energy are plotted over the map topography, showing their approximate location and extent. Although the area of this $g(\mathbf{r}, E)$ map is four times as large as that used for the previous sample, i.e. 50×50nm as opposed to 25×25nm, only around 9 suspected impurities are identified. If we assume that the suspected impurities are subsurface excess Fe, and, since an impurity-free field of view was intentionally chosen, if we assume an additional 9 surface impurities in a randomly selected field of view, then, with about 35180 (8795×4, see section 4.3) stoichiometric Fe atoms in the same field of view, we can estimate the level of excess Fe to about 0.05%, or about two orders of magnitude lower than the amount of excess Fe in the $Fe_{1.04}Se_{0.28}Te_{0.72}$ sample. EDX measurements were unable to detect any excess Fe in this composition, and would not have been able to detect this concentration of impurities. In fig. 4.4 (d), a linecut is taken across the Fermi energy layer of the map at the position indicated in fig. 4.4 (c). The spatial extent of the LDOS contribution of two spectroscopic anomalies is captured in the plot. The two impurities' LDOS signatures have HWHM values (determined by fitting with a Gaussian) of 1.53nm and 1.56nm, respectively, which is larger than the LDOS signatures of the type II impurities characterized in the previous section, about 0.5nm HWHM. This could indicate that the observed impurities are not, in fact, type II subsurface Fe impurities, but rather Fe impurities from lower layers.

4.5 Conclusion

In this SI-STM study the effects of impurities such as excess Fe content on the electronic properties of the iron chalcogenides have been examined. As it is currently understood, excess Fe atoms at low concentrations represent magnetic pair-breaking centers which locally disrupt superconductivity. Magnetic coupling between the excess Fe and stoichiometric Fe sheets likely favors short range magnetic order and leads to a weak charge-carrier localization. Higher concentrations of excess Fe lead eventually to a phase separation into magnetic and superconducting phases and finally to full magnetisation under total suppression of superconductivity. In this study, I have identified two species of excess Fe which can be differentiated according to their contribution to LDOS. The two LDOS signatures are unambiguous over a wide range of energies and, based on that finding, I have shown that the concentration of each species appears to be approximately equal. Furthermore, based on a comparison between STM and EDX data and theoretical models in the literature, I conclude that virtually all of the observed excess Fe is interstitial rather than substitutional. Excess Fe atoms are found to be located both on the obverse and on the reverse of each constituant iron chalcogenide layer, with the two spectroscopic signatures corresponding to the obverse and reverse Fe, respectively, of the top-most layer. The origin of the LDOS contributions of the two species on either side of the Fermi level, however, remains unclear.

Chapter 5

Nanoscale Inhomogeneity

In which I investigate spatial inhomogeneity of the superconducting gap in the iron chalcogenides and iron pnictides.

5.1 Introduction

Significant evidence suggests that spin fluctuations play an important role in iron-based superconductivity, including, e.g., the observation by neutron scattering of magnetic resonance modes at the nesting vectors between Fermi surface sheets [81, 118, 142]. However, despite experimental and theoretical successes which have lead to a better understanding of the pairing mechanism, a number of questions remain unresolved. For example, the symmetry of the superconducting order parameter remains ambiguous and there is still no predictive theory. One difficulty is that the band structures of these materials are complicated, with up to five bands derived from Fe-3d orbitals crossing the Fermi level [143]. In the iron chalcogenides, it appears that the superconducting gap near optimal doping is nodeless [144], albeit with some anisotropy, whereas in MBE-grown parent FeSe films nodes have been observed [145].

In another iron-based superconductor, LiFeAs, an anisotropic order parameter has been observed by angle resolved photoemission (ARPES) [146] and scanning tunneling microscopy (STM) [147], leading to speculation that superconductivity in the material may be spin-triplet [148]. In the case of the iron chalcogenides, results from ARPES experiments have been inconclusive. Miao *et al.* have reported isotropic gaps for both the hole-like and electron-like sheets of the Fermi surface, albeit of different magnitude [149], while in a laser ARPES study Okazaki *et al.* report anisotropic gaps [150]. The latter interpretation is supported by angle-resolved specific heat measurements, which are also consistent with an anisotropic gap [151]. A QPI study indicates that the order parameter reverses sign between different sheets of the Fermi surface, supporting an interpretation in terms of an order parameter with $s_\pm$ symmetry [144].

In the iron pnictides (with "122" chemical formula), the superconducting gap has been found to be spatially inhomogeneous [133, 152]. However, cleaving of most iron pnictides creates a disordered surface, so it is not clear whether the observed inhomogeneity is representative of the bulk.

In the following I present an SI-STM study of spatial inhomogeneity of the superconducting gap in $\mathrm{Fe_{1.00}Se_{0.4}Te_{0.6}}$ and $\mathrm{Ba_{0.68}K_{0.32}Fe_2As_2}$ and discuss the findings in light of predictions for pairing symmetry.

5.2 Surface characterization

In fig. 5.1 (a), an STM topography of the cleaved crystal can be seen. The topography is atomically resolved, with the majority of the atoms appearing to be higher / brighter while a minority appear to be relatively lower / darker. Analysis of the image with a counting algorithm indicates that the higher atoms represent 60% of the total while the lower atoms represent 40%. This finding is consistent with EDX measurements. In fig. 5.1 (b) the peaks representing the two chalcogen species are clearly visible. Excess surface Fe is not seen. Tunneling spectra, shown in fig. 5.1 (c) as a function of temperature, reveal a similar gap structure and evolution to that reported by Hanaguri *et al.* on the same composition [144]. In the spectra, coherence peaks appear around ±2.5mV while another, weaker pair of features are visible around ±5.2mV. Somewhere between 12K and 16K the gap closes completely, consistent with the known T_c of about 14K.

5.3 Gap anisotropy

In order to investigate the superconducting gap in $\mathrm{Fe_{1.00}Se_{0.4}Te_{0.6}}$, several $g(\mathbf{r}, E)$ maps were taken at temperatures of 2.1K, 4.2K, 8K, 12K, and 16K, with a spatial resolution of 64×64pxl in a 20nm × 20nm field of view. (Averaged spectra from the maps are shown in fig. 5.1 (c).) From the data, maps of gap size as a function of position ($\Delta(\mathbf{r})$) were obtained by fitting with the Dynes gap equation (eq. 2.13). In fig. 5.2 (a), the gap map at 2.1K is shown. From the $\Delta(\mathbf{r})$ data, the size of the superconducting gap was found to be spatially inhomogeneous with a characteristic length scale of $\sim$ 3.0nm. From the histogram in fig. 5.2 (b), it can be seen that $\Delta(\mathbf{r})$ varies between about 0.25meV and 2.2meV. In fig. 5.2 (c), a spectra linecut is shown which was obtained along the indicated position from the 2.1K data. The

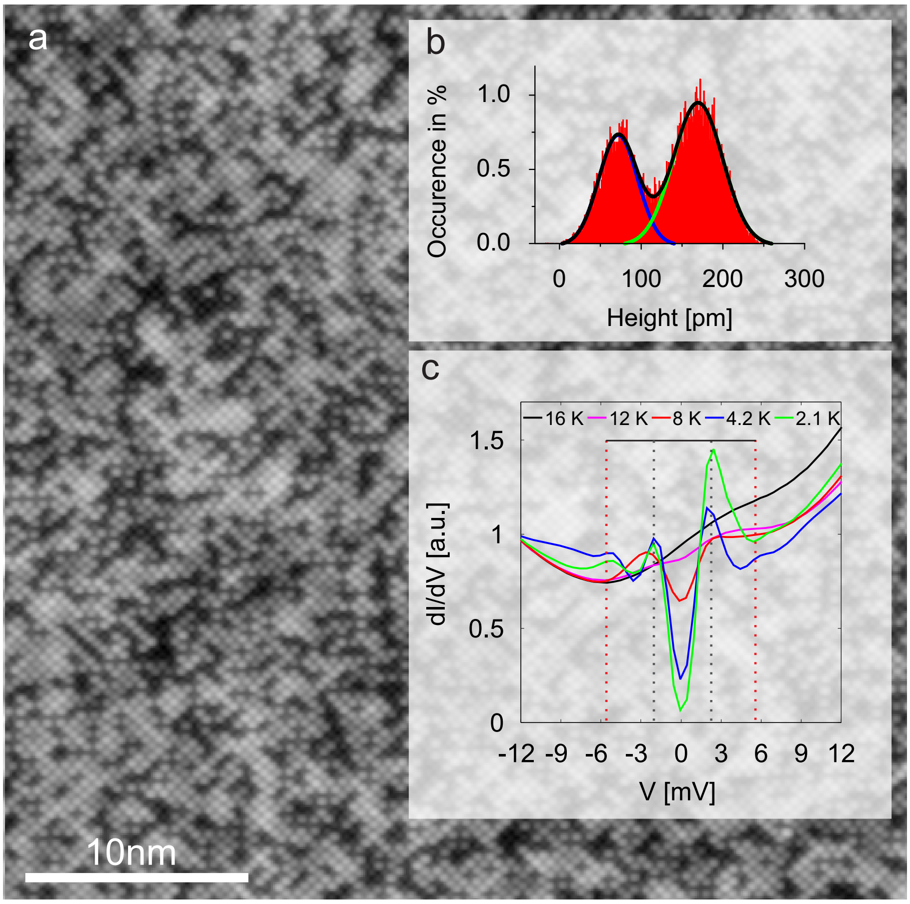

Figure 5.1: Composition analysis. (a) STM topography of an *in situ* cleaved iron chalcogenide crystal, measured at 2.1K with $V = -50\text{mV}$ and $I = 0.8\text{nA}$. (b) Histogram of the height profile of the topography, after processing. Gaussians have been fitted to the two chalcogen peaks and the results confirm the composition results returned by EDX, namely $\text{Fe}_{1.00}\text{Se}_{0.4}\text{Te}_{0.6}$. (c) dI/dV as a function of temperature, averaged from 4096 single spectra taken over an area of size 20nm × 20nm.

coherence peaks at ±2.1meV can be seen to decrease with the size of the gap until the gap fully disappears and only a relative depletion in dI/dV remains.

We can use the inhomogeneity of the gap size in order to estimate the superconducting coherence length. In fig. 5.2 (d), the autocorrelation of a gap map with a 38×38nm field of view is shown. In fig. 5.2 (e), line cuts bisecting the autocorrelation along the horizontal (green) and vertical (cyan) axes are shown, as well as and an azimuthally averaged radial profile (blue). The solid line (red) is a fit of the radial line cut. By fitting an exponential decay function to the line profile we find a decay length of $\xi = 1.7\text{nm}$, which is in good agreement with a measure of

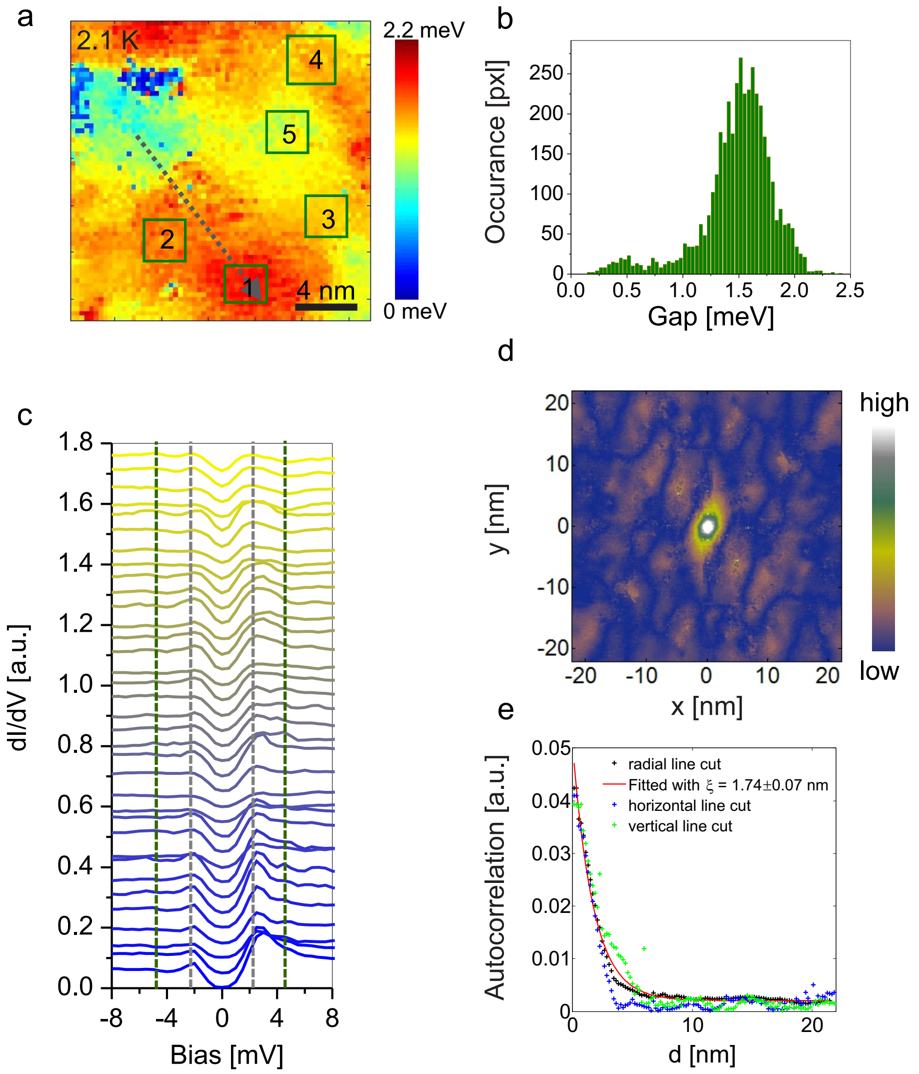

Figure 5.2: (a) Gap map ($\Delta(\mathbf{r})$) of $Fe_{1.00}Se_{0.4}Te_{0.6}$ obtained from a 20nm × 20nm $g(\mathbf{r}, E)$ map. Maps were taken at 2.1K, 4.2K, 8K, 12K, and 16K, with a spatial resolution of 64×64pxl. (b) Histogram of the gap distribution. (c) Spectra line cut from the 2.1K map, along the indicated path. (d) Autocorrelation of a $\Delta(\mathbf{r})$ map with a 38×38nm field of view. (e) Line cuts bisecting the autocorrelation along the horizontal (green) and vertical (blue) axes, and an azimuthally averaged radial profile (black). The solid line (red) is a fit of the radial line cut.

the coherence length obtained from H_{c2}, 1.5nm [153].
We believe that the main source of inhomogeneity in $\mathrm{Fe_{1.00}Se_{0.4}Te_{0.6}}$ is likely to be disorder of the chalcogen atoms at the sample surface. This would parallel the situation in the cuprates, where spatial inhomogeneity has been shown to arise due to disorder of the dopant atoms [154, 155]. However, while the cuprates are charge-doped, the substitution of Se by Te in $\mathrm{Fe_{1.00}Se_{0.4}Te_{0.6}}$ is isoelectronic. For this reason, the mechanism linking the dopant inhomogeneity to the local variation in the size of the superconducting gap has to be different.

5.4 Order parameter

In order to investigate the superconducting order parameter in $\mathrm{Fe_{1.00}Se_{0.4}Te_{0.6}}$, I will compare a symmetrized and normalized spectrum to fits calculated for different order parameters. In order to obtain the fits, different angular-dependent order parameters $\Delta(\theta)$ were introduced into eq. 2.13. Cases of pure s-wave ($\Delta(\theta) = \Delta_0$), anisotropic s-wave ($\Delta(\theta) = \Delta_0 + \Delta_1 \cos 4\theta$), and d-wave ($\Delta(\theta) = \Delta_0 \cos 4\theta$) order parameters have been considered. Furthermore, to accurately describe the temperature dependence of the spectra, the thermal broadening of the Fermi function has been accounted for.
While the differential conductance signal (as previously mentioned) is proportional to the local density of states, the proportionality constant depends on additional variables such as the tip height and details of the tip apex [7, 156]. In order to eliminate these effects, as well as contributions from the normal state DOS, the spectra taken below T_c have been divided by spectra acquired with the same tunneling parameters at $T > T_c$.
In fig. 5.3, a spectrum averaged over a 20nm × 20nm, 64×64pxl map, taken at 2.1K, is plotted. The spectrum has been symmetrized around zero bias and normalized by dividing with a spectrum taken above T_c. The colored lines show fits with the Dynes equation for s-wave, anisotropic s-wave, and d-wave order parameters. The best fit is obtained in the anisotropic s-wave scenario, while the s-wave and d-wave scenarios do not give the same level of agreement. The extracted gap size is $\Delta_0 = 1.417$meV, which is close to the results obtained from an STM study showing coherence peaks in the tunneling spectra at ±1.7meV [144], as well as from ARPES [149] and optical spectroscopy [157] studies. For the anisotropy, a value of $\Delta_1 = 0.599$meV is obtained. I would like to stress that while we consider a $\cos 4\theta$ term in our fits, it cannot be excluded that the anisotropy is governed, e.g., by a $\cos 2\theta$ term, because the result remains the same for any integer multiple of θ.
The anisotropy we observe is about 40% of the gap magnitude. This is consis-

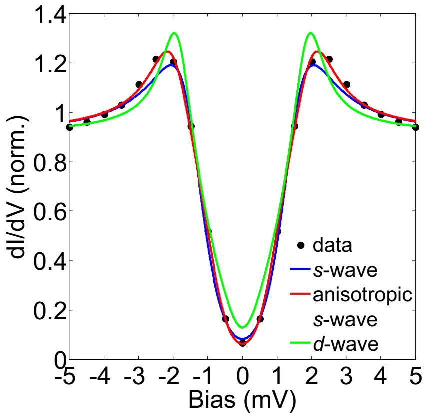

Figure 5.3: The plotted spectrum (black circles) has been averaged over a 20nm × 20nm, 64×64pxl map taken at 2.1K. The spectrum has been symmetrized and normalized by dividing with an averaged spectrum taken above T_c. The blue, red, and green lines are fits with eq. 2.13 modified for *s*-wave, anisotropic *s*-wave, and *d*-wave, with $\Delta(\theta) = \Delta_0$, $\Delta_0 + \Delta_1 \cos\theta$, and $\Delta_0 \cos\theta$, respectively.

tent with angle-resolved specific heat experiments on crystals of slightly different composition (i.e. $FeSe_{0.45}Te_{0.55}$) [151]. Recently, an anisotropy of around 25% has been observed in laser ARPES experiments, along with a superconducting gap of $\Delta_0 = 1.63$meV [150]. These values are consistent with our findings.

5.5 Temperature evolution

In order to explore the temperature evolution of the superconducting gap, spectra have been averaged over 3nm × 3nm regions of the $g(\mathbf{r}, E)$ map for each temperature. The results are plotted in fig. 5.4 (a) and (b) for regions with large gap and small gap, respectively. The temperature evolution of the spectra reveals that the superconducing gap disappears at different temperatures in different regions of the sample. For example, spectra taken at 12K in a region with a large superconducting gap (fig. 5.4 (a)) show a slight dip near zero bias which is absent in spectra taken in the region with small local gap size (fig. 5.4 (b)).

5.6 T_c inhomogeneity

Local variations in transition temperature have been determined by examining the temperature evolution of gap size at the five different locations indicated in fig. 5.2 (a). At each location and temperature, the gap size has been determined by fitting

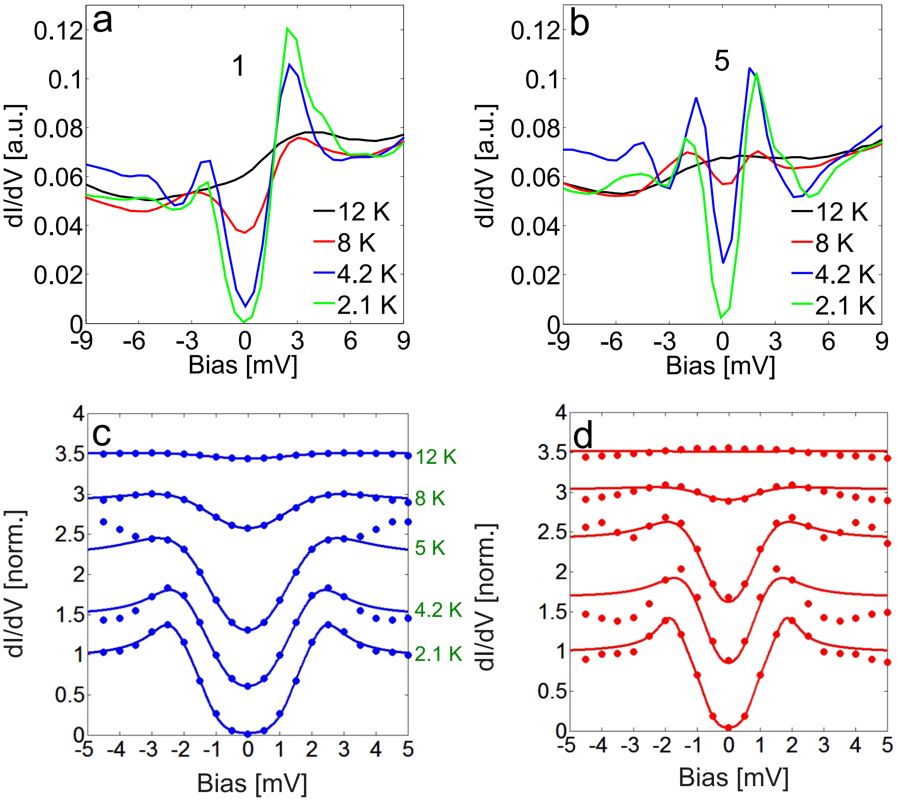

Figure 5.4: (a),(b) Temperature dependence of spectra, averaged over two different areas of size 3nm × 3nm each, in regions with large (position 1 in fig. 5.2 (a)) and small (position 5 in fig. 5.2 (a)) local gap size, respectively. (c),(d) Spectra taken at different temperatures in regions of large and small gap size, respectively, have been fitted with eq. 2.13 for an anisotropic *s*-wave order parameter. Spectra are symmetrized around zero bias and normalized by background data taken at 16K. Thermal broadening has been accounted for.

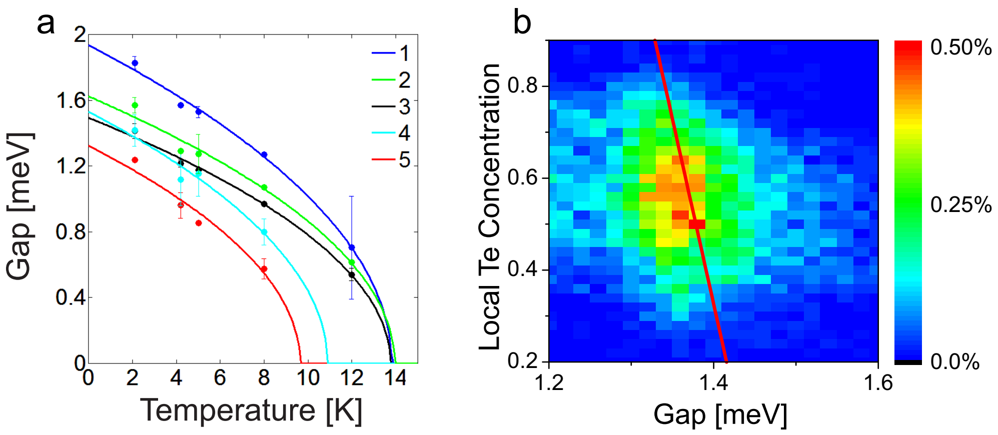

Figure 5.5: (a) Plot of gap size as a function of temperature for the five different regions marked in fig. 5.2 (a), showing local differences in the temperature at which the gap is completely closed. The colored lines are fits with the gap size temperature dependence predicted in BCS theory. (b) 2D correlation between the local gap size and the local height in the STM topography. Regions near impurities, identified by an increased differential conductance at zero bias, are excluded from the correlation.

with eq. 2.13 for an anisotropic s-wave order parameter. In fig. 5.4 (c) and (d), symmetrized and normalized spectra taken at different temperatures from regions with large and small local gap size are shown. At high temperatures, the fits become less accurate, partially because of the increased differential conductance near zero bias. The values obtained from the fits show a monotonic decrease with increasing temperature, which can be seen in fig. 5.5 (a). Fitting the temperature dependence of the gap size ($\Delta(T) = \Delta_0\sqrt{1 - T/T_c}$) [158] yields good agreement over the whole temperature range, which is surprising because this functional form should only be valid as $T \rightarrow T_\mathrm{c}$. At temperatures $T < T_c$, the extracted gap size shows a stronger temperature dependence than would be expected from BCS theory. For the ratio $2\Delta_0/k_\mathrm{B}T_c$, the fits yield values in a range from 2.5 to 3.2, which is close to the value obtained for weak coupling ($2\Delta = 3.52k_\mathrm{B}T_c$). The critical temperatures obtained from regions of different gap size are in the range of 10K to 14K. Thus, it is effectively the superconducting transition temperature which is inhomogeneous in $\mathrm{Fe}_{1.00}\mathrm{Se}_{0.4}\mathrm{Te}_{0.6}$.

5.7 Universal curve

We have found that, in the field of view in which the $g(\mathbf{r}, E)$ data was taken, the local superconducting gap size can be correlated with the anion height. In fig. 5.5 (b), a two-dimensional histogram of local anion height as a function of gap size is shown. A weak anticorrelation of -0.2 between local height and gap size was calculated. This is consistent with what we would expect to find due to the proposed universal curve of T_c as a function of anion height, and also what has been found from the pressure dependence of T_c [66]. We see two possible explanations for why only weak anti-correlation between the two quantities is observed. First, if the surface layer were superconducting only due to the proximity effect then no clear correlation between gap size and anion height would be expected. Second, the T_c in the surface layer could be influenced by adjacent layers due to interlayer coupling.

5.8 Gap localization

An SI-STM study of spatial inhomogeneity of the superconducting gap was also performed in the optimally doped iron pnictide $Ba_{0.68}K_{0.32}Fe_2As_2$, which has a T_c of $\sim$ 38K. Since the doping in this compound is charge (hole) doping, rather than isoelectronic, variation in gap size based on the positions of dopant atoms would not necessarily be surprising. In addition, in contrast to the iron chalcogenides this compound has no natural cleavage plane and is therefore expected to have a rough surface on cleaving. Specifically, cleaving is expected to occur along the $Ba_{0.68}K_{0.32}$ plane, one half of which would remain at the sample surface. In general, this property reduces the usefulness of an STM study, because of differences between surface properties and the bulk, and also because of problems caused by the irregular surface. Nevertheless, we have been able to investigate gap anisotropy at the surface of a $Ba_{0.68}K_{0.32}Fe_2As_2$ crystal, and have found that it is reminiscent of that found in the cuprates, where the inhomogeneity is related to the presence of Zn atoms (and the localized introduction of an extra d electron) [136, 159]. However, while the effect in the cuprates is the local suppression of superconductivity around the dopant atoms, we find in $Ba_{0.68}K_{0.32}Fe_2As_2$ exactly the opposite effect, namely a well-developed gap only in the close vicinity of the dopants, and its suppression elsewhere. This finding suggests that superconductivity at the surface of $Ba_{0.68}K_{0.32}Fe_2As_2$ could be a localized phenomenon.
In fig. 5.6 (a), an STM topography of $Ba_{0.68}K_{0.32}Fe_2As_2$ is shown. The image does not show clear atomic resolution, but the main features are visible. Above the sample surface, which consists of As atoms, many surface impurities can be

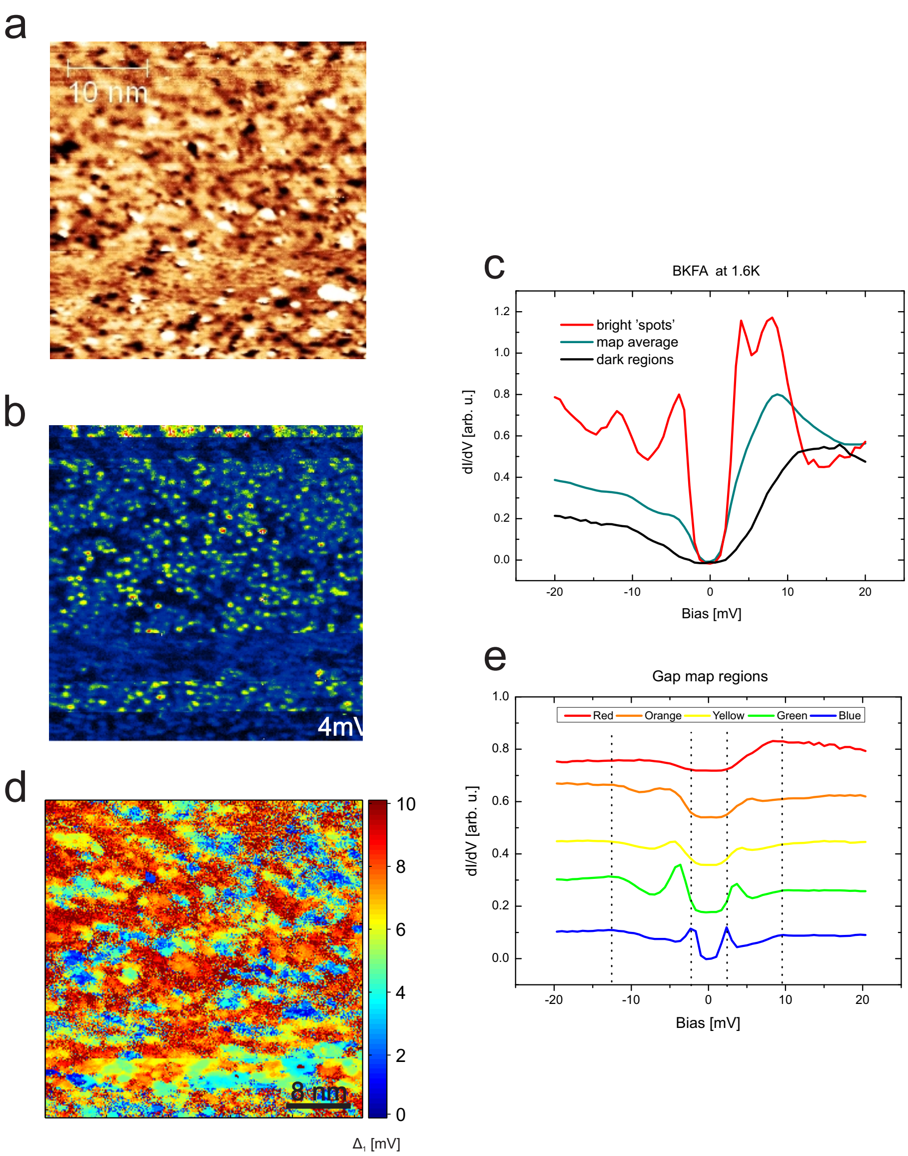

Figure 5.6: (a) Map topography taken on optimally doped iron pnictide superconductor $Ba_{0.68}K_{0.32}Fe_2As_2$. (b) Energy cut at +4mV taken from the $g(\mathbf{r},E)$ map, showing strongly gapped centers (bright) surrounded by a weakly gapped area (dark). (c) Spectra taken from areas with well developed coherence peaks (red) and suppressed coherence peaks (black), as well as the map average spectrum (green). (d) $\Delta(\mathbf{r})$ map obtained by fitting the $g(\mathbf{r},E)$ map with the Dynes equation (eq. 2.13), showing large variations in gap size as a function of position. (e) Spectra taken from different regions of the $\Delta(\mathbf{r})$ map, corresponding to blue, green, yellow, orange, and red areas, showing an increasingly wide gap with suppressed coherence peaks, consistent with the anticipated local effects of hole doping in an optimally doped system.

seen. The impurities are presumed to be Ba and K based on EDX and the expectation of cleaving into the $Ba_{0.68}K_{0.32}$ plane. In spectroscopy data, we find small regions in which spectra exhibit a well pronounced gap of size $\Delta \sim 4$mV, and a wider region in which a strongly suppressed gap is observed. In fig. 5.6 (b), spectra with well pronounced (red) and suppressed (black) coherence peaks are plotted, along with the map average. In figure 5.6 (c), the layer of the $g(\mathbf{r}, E)$ map corresponding to the first positive coherence peak, at +4mV, is shown. At this energy, many bright (pronounced gap) spots are visible, surrounded by a darker (suppressed gap) region.

We note the confirmation of the double-gap electronic structure mentioned in several previous studies [132, 136]. The inferred size of the larger gap, $\Delta_1 = 9.1$meV, is in reasonable agreement with the current findings, while inferred size of the smaller gap, $\Delta_2 = 1.5$meV, is significantly smaller than what we observe.

We find that, while the first gap is approximately symmetric around the Fermi energy, the second gap shows some asymmetry. Specifically, in the second gap, coherence peaks appear at energies of around +8mV and −12mV. The origin of this asymmetry is not clear.

In fig. 5.6 (d), the spectra have been fitted with the Dynes equation [34] and the result has been plotted as a gap map ($\Delta(\mathbf{r})$). The gap map shows more structure than the +4mV energy slice and gives an idea of the spatial extent of the areas with well pronounced coherence peaks (i.e., about 2nm in diameter). Green, yellow and orange dots represent varying gap widths, as determined from the fitting, while the larger region showing a suppressed gap is represented with red and sometimes dark blue (when the spectrum could not be properly fitted). In fig. 5.6 (e), spectra are shown which correspond to each color in the gap map and have been averaged over a single region. The regions colored light blue show a very well developed gap while the regions colored red show a very large gap with strongly suppressed coherence peaks. The colors green, yellow, and orange show regions exhibiting increasing gap size with partially suppressed coherence peaks. While the identity of the small regions showing a well pronounced gap is not immediatedly clear (e.g., from a comparison with the topography), from their number and irregular positioning one possible candidate could be the hole donor, K. With a lattice constant of ∼ 3Å and the Ba / K layer halved due to cleaving we would expect about 8889 Ba / K atoms in the 40×40nm field of view, of which about 2844 would be K. In the map cut at +4mV, something in the vicinity of 752 regions with pronounced superconductivity are counted (estimated), which is less than the expected amount of K. However, given that the superconducting regions are much larger than the individual lattice sites (i.e., ∼ 2nm as opposed to a ∼ 3Å lattice constant) we have probably undercounted the impurities by a substantial amount.

If this interpretation is correct, the explanation for the observed localization of the gap is still not necessarily clear (i.e., that superconductivity only exists near the hole donors). It could be, for example, that the STM tip is only able to couple well to the bulk superconductivity near the K lattice sites. In this case, the observed superconducting regions would not be due to intrinsic material properties but instead would represent a matrix-element effect.

5.9 Conclusion

In conclusion, low temperature SI-STM studies of the superconducting gap have been performed on two iron-based superconductors at close to optimal doping. In the iron chalcogenide, $Fe_{1.00}Se_{0.4}Te_{0.6}$, significant spatial inhomogeneity of the superconducting gap has been observed. The local size of the gap weakly correlates with local height, which is a function of Se / Te concentration. Comparison of measured tunneling spectra with calculated spectra for different superconducting order parameters (s-wave, d-wave, and anisotropic s-wave) shows best agreement for an anisotropic s-wave symmetry. Comparison of gap evolution as a function of temperature for areas exhibiting large and small gap size suggests that it is actually the superconducting transition temperature which is inhomogeneous in this material.

In the iron pnictide, $Ba_{0.68}K_{0.32}Fe_2As_2$, a double gap structure has been observed with the size of the larger gap in reasonable agreement with that found in the literature, while the size of the smaller gap is larger than values in the literature by about a factor of two [132, 136]. The smaller gap is symmetric around the Fermi energy but the larger gap shows a substantial asymmetry. On the crystal surface, a pattern was observed in which small regions showing a well developed superconducting gap are surrounded by a region showing a much larger gap with suppressed coherence peaks. One interpretation is that the smaller regions are centered around K atoms, which are the chemical dopant in the compound. It is not clear whether the observed effect is intrinsic to the material, or a matrix-element effect caused by spatially dependent coupling of the tip to the sample.

Chapter 6

Electronic Symmetry Breaking

In which I investigate electronic states which appear to break the tetragonal (C_4) symmetry of the iron chalcogenides in the absence of a corresponding structural distortion.

6.1 Introduction

The existence of electronic symmetry breaking from tetragonal (C_4) to C_2 in the parent compounds of iron-based superconductors has been widely discussed in the literature [161–167]. Electronic nematicity can occur in these materials due to orbital [47] or magnetic ordering, which tight-binding calculations have indicated would lead to a reconstruction of the Fermi surface. In fig. 6.1 (a) and (b), the concept of orbital and spin density wave (SDW) order, respectively, is represented along with corresponding calculations for the Fermi surface in the case of a generalized iron-based superconductor [160].

In many iron-based superconductors, orthorhombic distortion of the crystal lattice accompanies electronic symmetry breaking. In an orthorhombically distorted lattice, it is not surprising that the electronic states break tetragonal symmetry. The question then becomes whether the lattice lowers its symmetry as a consequence of nematic ordering in the electronic states, or rather vice versa. In some cases, however, observed asymmetry is much larger than could reasonably be explained by orthorhombic lattice distortion [47, 145, 168], so that independent electronic states with nematic character are suggested [145, 168–170]. Experimental characterization of these nematic states has already been performed with a wide variety of techniques, including STM [168], ARPES [171], optical spectroscopy [172], and transport [173]. In many cases, electronic nematicity has been found in systems exhibiting quantum critical behavior, hinting at a possible intimate relation-

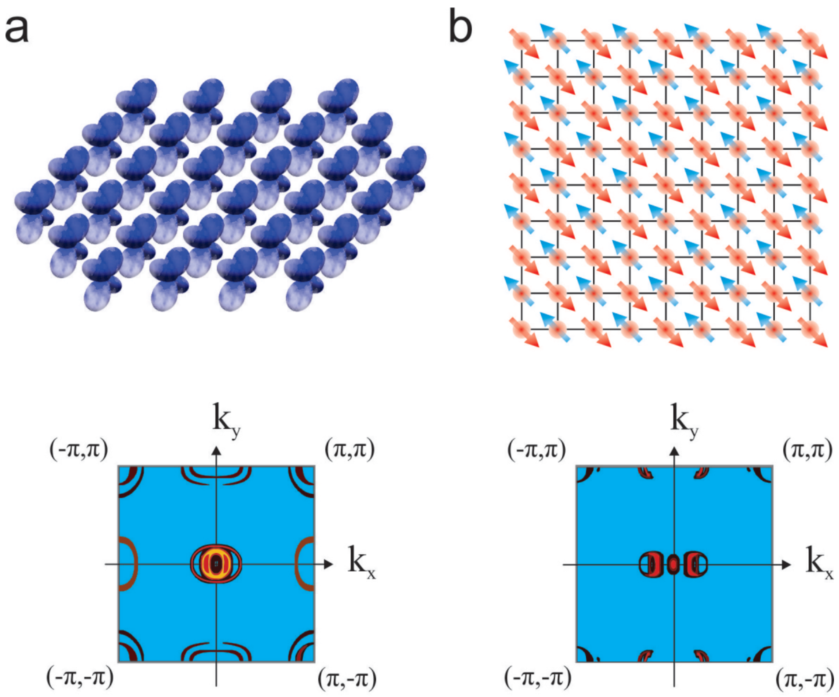

Figure 6.1: Conceptual representation of symmetry breaking order in the iron-based superconductors. (a) Graphical representation of orbital ordering and corresponding anisotropic Fermi surface. (b) Graphical representation of spin density wave (SDW) order and corresponding anisotropic Fermi surface. Both Fermi surfaces were calculated for a generalized iron-based superconductor and are adapted from [160].

ship between the two.

Experimental evidence from an SI-STM study will be presented which supports the existence of electronic nematicity in nominally tetragonal $Fe_{1.00}Se_{0.4}Te_{0.6}$. The nematic states will be shown to persist both above and below T_c, and I will investigate whether these states coexist with, or rather compete with superconductivity. X-ray diffraction experiments performed on crystals of the investigated composition indicate that the lattice structure is tetragonal throughout the full temperature range, in both normal and superconducting states [120], and does not undergo an orthorhombic transition. However, since an orthorhombic transition is observed in samples with slightly higher doping (e.g. $Fe_{1+\delta}Se_{0.57}Te_{0.43}$ [174]), it may not be prudent to entirely rule out the possibility of orthorhomic distortion in the crystal lattice of the investigated compound.

6.2 QPI

In order to investigate the nematic states, we have taken a 15 layer, 50×50nm $g(\mathbf{r}, E)$ map from -4.5mV to $+4.5mV$, at 2.1K. The map is sufficiently large to image quasiparticle interference (QPI) patterns, from which we can extract the dominant scattering vectors by analyzing the Fourier transforms of map cuts at constant energy. So that we can investigate a possible relationship between the nematic states and superconductivity we have also taken a map at 16K, which is above T_c. In fig. 6.2 (a)-(d), nematic electronic states from the low temperature map are shown in real space at -4.5mV, -2mV, +2mV, and +4.5mV, respectively. In fig. 6.2 (e)-(h), the same data set is shown in Fourier space. The scattering patterns in the two directions parallel to the Fe-Fe bonds, marked h and v, are clearly different, which is unexpected given the tetragonal symmetry of the crystal lattice. In fig. 6.2 (i) and (j), the symmetry breaking states are plotted along h and v, respectively, as a function of energy. In fig. 6.2 (k) and (l), the same is done for the map taken above T_c. In fig. 6.2 (m) we can see that the wave vector increases slightly with decreasing energy. In addition, we can see that the tetragonal symmetry remains broken above T_c, with a similar level of splitting as seen in the 2.1K data. However, while the dominant scattering vector is gapped at the Fermi energy in the data below T_c, above T_c the gap disappears and the vector becomes fully traceable across E_F.

6.3 Fermi surface calculations

In order to better understand the observed asymmetry of the scattering vector, we will consider a tight-binding model – the five band model by Graser *et al.* [175] – with appropriate renormalizations of the bands to maintain consistency with ARPES measurements [107]. Orbital splitting is included by imposing different occupations for the d_{xz} and d_{yz} orbitals, which leads to a ferro-orbital ordering [162]. Magnetic ordering has not been included in the calculations because there is no evidence for static magnetic order in the iron chalcogenides through most of the phase diagram. Only in the non-superconducting parent compound FeTe has a double stripe order been observed, albeit with an ordering vector rotated by 45° with respect to the Fe-Fe bond direction [120]. In fig. 6.3 (a) and (b), a Fermi surface and its associated quasiparticle interference pattern, respectively, are shown. These have been obtained by calculating the joint density of states (JDOS) of the tight-binding model with tetragonal symmetry.

Lifting the orbital degeneracy of d_{xz} and d_{yz} by including an orbital splitting in the model leads to a distortion of the Fermi surface, shown in fig. 6.3 (c), and conse-

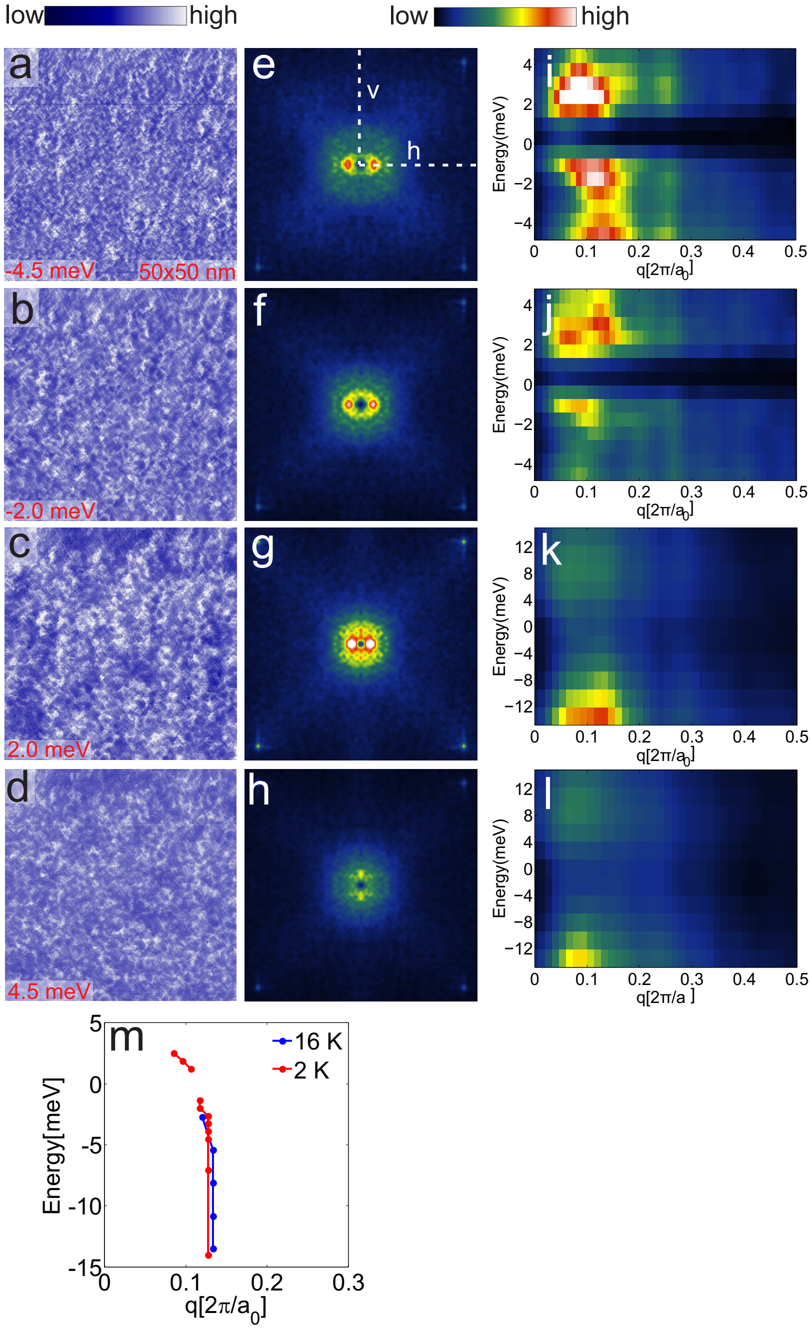

Figure 6.2: $g(\mathbf{r}, E)$ map of $Fe_{1.00}Se_{0.4}Te_{0.6}$, taken at 2.1K and 16K, from −4.5mV to $+4.5mV$ with 15 layers. (a)-(d) Symmetry breaking states in real space at selected energy cuts. (e)-(h) The same data set in Fourier space, showing clear asymmetry in the h and v directions. (i),(j) Symmetry breaking states plotted along the vectors h and v, from the map taken at 2.1K. (k),(l) Symmetry breaking states plotted along the vectors h and v, from the map taken at 16K. (m) Energy dependence of the dominant scattering vector.

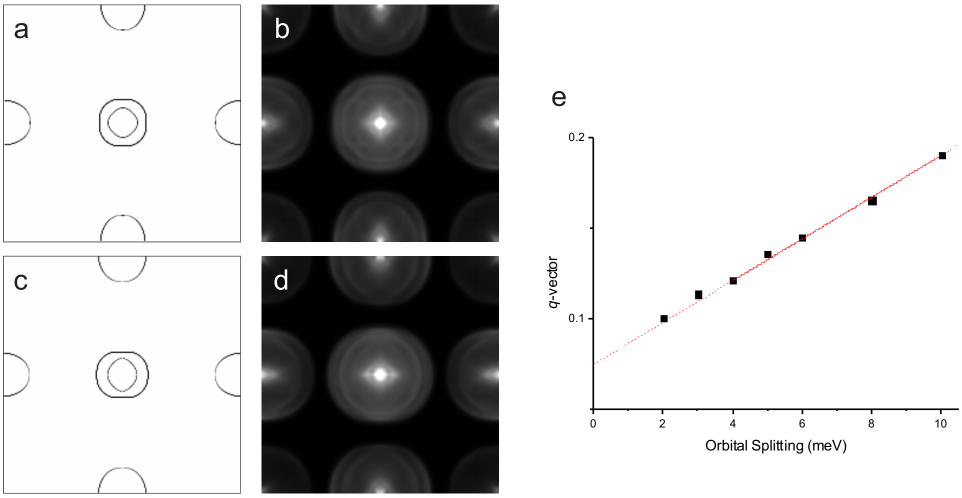

Figure 6.3: Electronic structure of Fe$_{1.00}$Se$_{0.4}$Te$_{0.6}$, as calculated with a five band tight-binding model [175], with band renormalizations by comparison with ARPES data. (a),(b) Fermi surface and corresponding quasiparticle interference pattern, without orbital splitting. (c),(d) Fermi surface and corresponding quasiparticle interference pattern, with orbital splitting. (e) Estimate of orbital splitting magnitude via comparison of observed q-vector with the model. In the final analysis, we estimate there to be ~4meV of splitting present.

quently to anisotropic QPI scattering, shown in fig. 6.3 (d). Including orbital splitting, the dominant scattering vectors are the two pronounced maxima near $Q = 0$. The magnitude of this vector depends sensitively on the magnitude of introduced orbital splitting, although the vector exhibits only weak dispersion. This vector can therefore be used to estimate the expected amount of orbital splitting, which is shown in fig. 6.3 (e). A comparison with the q-vector of the observed symmetry breaking states indicates the presence of an orbital splitting of approximately 4meV in magnitude, corresponding to a temperature scale of around 50K. This amount of splitting, which we have just calculated for the iron chalcogendies, appears significantly smaller than the 60meV of splitting which has been reported for the iron pnictides [171]. The dominant scattering vectors appear likewise smaller than those reported from STM studies on the iron pnictides. This could be explained by the smaller orthorhombic distortion, if any, in this material.

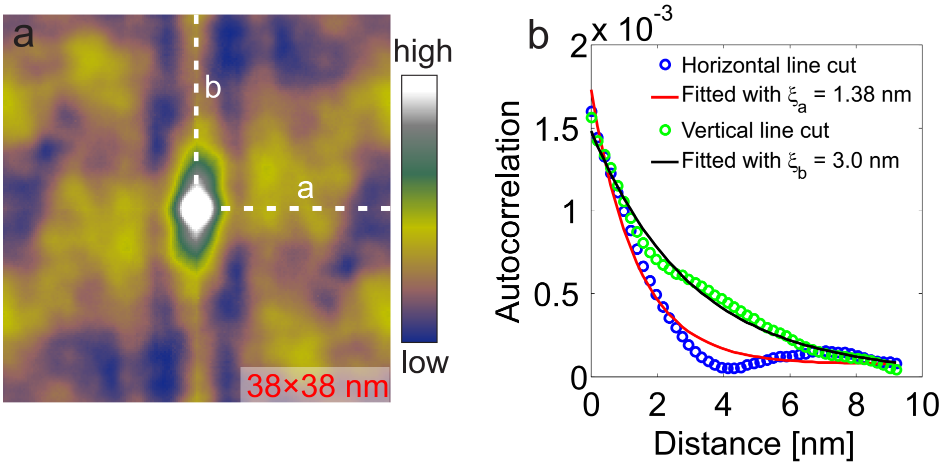

Figure 6.4: Estimate of coherence length (ξ) in $\mathrm{Fe}_{1.00}\mathrm{Se}_{0.4}\mathrm{Te}_{0.6}$, via autocorrelation analysis. (a) Autocorrelation of a gapmap of size 38×38nm. (b) Exponential decay fitting of linecuts parallel and perpendicular to the electronic anisotropy. Values of $\xi_h = 1.38$nm and $\xi_v = 3.0$nm are obtained.

6.4 Autocorrelation

To gain further insight into the nematic states I next present an autocorrelation analysis of a gap map of size 38×38nm. The autocorrelation is shown in fig. 6.4 (a), with the h and v directions indicated. The elongated structure in the v axis is indicative of electronic anisotropy. In fig. 6.4 (b), the superconducting coherence length (ξ) in the h and v directions is estimated by fitting an exponential decay function to corresponding linecuts made from the center of the autocorrelation. From the fits, values of the coherence length of $\xi_h = 1.38$nm and $\xi_v = 3.0$nm, respectively, have been obtained.

ARPES experiments on the iron chalcogenides have thus far not reported the anisotropy seen in this study. A possible explanation for this is that the relevant experiments were not performed on detwinned crystals.

6.5 Gap size

An important question raised by the foregoing observations is the nature of the relationship between symmetry breaking phenomena and pair formation in iron-based superconductors. We can imagine several scenarios. First, a competing order such as spin density wave order could act to suppress pair formation [176,

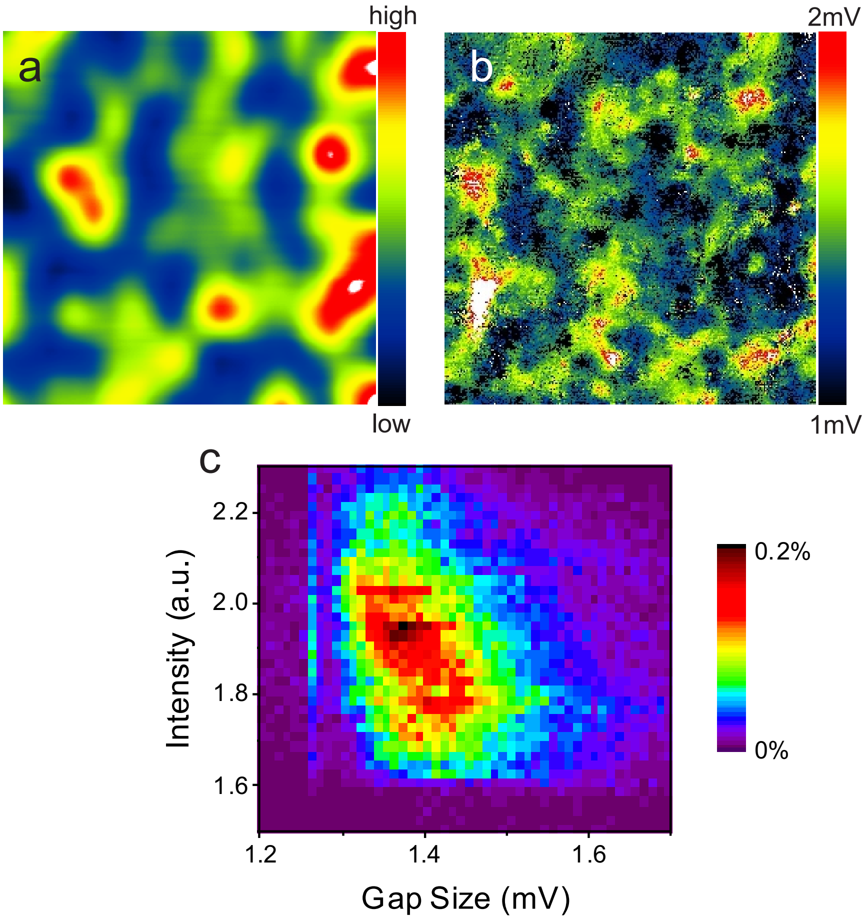

Figure 6.5: Nematic states and correlation with local gap size in $Fe_{1.00}Se_{0.4}Te_{0.6}$. (a) Nematic states at the lowest recorded energy, −5meV. (b) Local gap size over the same area. (c) 2D correlation of the nematic electronic states and local gap size, suggesting a negative relation between the nematic states and superconductivity.

177]. Second, an unknown alternative symmetry breaking state could be imagined to promote pair formation [178]. Third, there may be uncorrelated coexistence. To address this question, the nematic states observed in this study have been analyzed with respect to their real-space intensity distribution for possible correlation with local gap size. A real-space image of the nematic states is shown in fig. 6.5 (a), which was obtained from the raw data through Fourier filtering, whereby only the extended (symmetry broken) peaks in Fourier space (see, e.g., fig. 6.2) were allowed to pass. In fig. 6.5 (b), the local gap size is shown over the same area (as determined by fitting with the Dynes equation). Plotting the two values in relation to one another, as shown in fig. 6.5 (c), reveals a clear negative correlation. In this material, the presence of nematic states appears to correlate with weaker gap size, and vice versa. This is indicative of a competitive relationship between symmetry breaking and superconductivity.

6.6 Conclusion

The undoped iron chalcogenide parent compound, FeTe, does exhibit both a magnetic and structural phase transition. However, the ordering wave vector associated with the magnetic order is not the same as that of the nematic states described here. Thus, the symmetry breaking does not directly derive from the magneto-structural phase transition of the parent compound. On the other side of the phase diagram, undoped FeSe undergoes an orthorhombic phase transition and shows anisotropic scattering patterns similar to those observed in $Fe_{1.00}Se_{0.4}Te_{0.6}$ [145]. Even under suppression of the orthorhombic phase transition, which is reportedly achieved in the iron chalcogenides for x~0.5, results indicate that the electronic structure remains unstable against a reduction in symmetry from C_4 to C_2. The structural phase transition is driven by a susceptibility of the electronic structure towards a C_4 symmetry breaking due to orbital ordering, which is initially accompanied by only a tiny lattice distortion. The negative correlation observed between the strength of the symmetry breaking states and the size of the superconducting gap suggests a competitive relationship exists between the two phenomena. In contrast to the iron pnictides, in which a similar anisotropy has been found in a number of observables, no spin density wave order has been reported in $FeSe_xTe_{1-x}$ for $x > 0.2$. The absence of SDW order supports an interpretation in terms of ferro-orbital ordering. Comparing the observed relationship between the local gap size and the intensity of the symmetry breaking states to the physics of conventional phonon-driven superconductors may be suggestive. In the case of conventional superconductors, electron-phonon coupling is of course essential for the emergence of superconductivity. However, if it grows too strong such coupling will result in the formation of a Peierls instability in the crystal lattice, opening up a charge density wave (CDW) gap that will negatively impact superconductivity. In the unconventional superconductors, there appears to exist an analogous situation where magnetic and possibly orbital fluctuations play a central role in the emergence of superconductivity, but too much of these can result in a magneto-structural phase transition which ultimately suppresses the phenomenon.

In sum, nematic electronic states have been observed in the iron chalcogenide superconductor $Fe_{1.00}Se_{0.4}Te_{0.6}$, which persist above T_c and the immediate origin of which is interpreted here to be orbital ordering. The intensity of the nematic states is found to correlate negatively with the local size of the superconducting gap, suggesting a competitive relationship.

Chapter 7

Abrikosov Vortices

In which I investigate Abrikosov vortices and Andreev bound states in an iron chalcogenide superconductor.

7.1 Introduction

The Abrikosov vortex, named after the Nobel-prize winning Soviet physicist [179], is a location where a magnetic flux quantum penetrates a superconductor (in violation of the Meissner effect [38]). From the time of Abrikosov's pioneering work on the subject, superconductors have been divided into two categories depending on the value of the parameter χ, which is the relation between a superconductor's London penetration depth (λ_L) and superconducting coherence length (ξ). If $\chi (= \frac{\lambda}{\xi})$ is between 0 and $\frac{1}{\sqrt{2}} (\approx 0.7)$, then the superconductor is considered to be of type I. If χ is greater than $\frac{1}{\sqrt{2}}$, then the superconductor is considered to be of type II. The numerical value $\frac{1}{\sqrt{2}}$ is an important dividing line for the properties of a superconducting material because having a χ above this value will mean that the Cooper pair condensate has a negative surface energy, whereas having a χ below this value will mean that its surface energy is positive [179]. Superconductors of type I, such as most elemental superconductors (with the exceptions of Nb, Tc, and Vd), tend to have very small values of χ (such that $\chi \ll \frac{1}{\sqrt{2}}$). Phenomenologically, the most prominant difference between superconductors of type I and type II is their respective behavior under application of a magnetic field. If the magnetic field is increased above a material-specific critical field H_c, Type I superconductors will undergo a first order phase transition and revert to the non-superconducting state, while in the case of type II superconductors the same transition is much less sharp and takes place between two critical fields. It is in type II superconductors that Abriskosov vortices can exist, between the first and second critical magnetic fields ($H_{c1} < H < H_{c2}$). For additional information on the theory of Abrikosov vortices, see for example Kopnin [180].

Abrikosov vortices are interesting both from a theoretical and technological point of view. For theory, they represent a tool for probing the validity of the BCS theory of superconductivity [181], and for the investigation of quantum-limit phenomena [182]. Direct technological applications include quantum memory devices [183]. Research into vortex pinning is also directly applicable to superconducting magnets, since vortex movement can lead to a magnet quench. Recently, efforts have also been focused on the investigation of so-called giant or multiquantum vortices, which have a more complicated physics than the monoquantum vortex [184–186].

7.2 Density

In a type II superconductor, if we start with zero applied magnetic field and increase the strength up to the first critical field H_{c1}, at first all magnetic field lines will be expelled from the material due to the Meissner effect. Then, increasing the field above H_{c1} and continuing up to the second critital field H_{c2}, Abrikosov vortices will come into existence as magnetic field lines begin to penetrate the superconductor. The vortices will order themselves into regular patterns characteristic of the material and increase in number up to H_{c2}. Finally, above H_{c2}, superconductivity breaks down. The vortices are destroyed in the resulting transition to the normal state.

The value of H_{c2} in the iron-based superconductors is typically extremely high, e.g. between 51 and 126T in $Fe_{1.00}Se_{0.4}Te_{0.6}$ (extrapolated to 0K, as estimated by Yadav and Paulose [187]). In the same crystal, H_{c1} was found to be approximately 10mT in the $||ab$ direction and around 40mT in the $||c$ direction.

The number of monoquantum vortices N we expect to find in a given area A on the surface of a type-II superconductor is given by:

$$N = \frac{B \cdot A}{\Phi_0}, \tag{7.1}$$

where $\Phi_0 (= 2.068 \cdot 10^{-15} \mathrm{Tm}^2)$ is the magnetic flux quantum and B is the magnetic flux density. We can see that since N is linear in B, and the range between the two critical fields is large (3-4 orders of magnitude), an equally large variation in vortex lattice density is possible. If we insert values for $H_{c1}(\leq 40\mathrm{mT})$ and $H_{c2}(\geq 51\mathrm{T})$, as given above, and normalize to a reasonable (i.e., for STM) surface area of 50nm×50nm, then we can estimate the extreme limits of vortex density to between 0.05 and 62 cores per $2500\mathrm{nm}^2$ field of view. In our experiment, we are limited by the strength of our magnet, which is $\leq$16T, to a maximum of around 19.5 cores per $2500\mathrm{nm}^2$. In the following, I will focus on the effects of individual vortices on the electronic properties and on superconductivity in an $Fe_{1.00}Se_{0.4}Te_{0.6}$ crystal. Therefore, in this study a moderate magnetic field of 5T strength was applied, corresponding to an estimated vortex density of around 6 cores per 2500nm^2.

7.3 Bound states

Inside a vortex, a series of discrete bound states exists (Andreev bound states), which are separated by energies of around $\frac{\Delta^2}{E_F}$, where Δ is the size of the superconducting gap and E_F is the Fermi energy [188]. In conventional type II superconductors, the Fermi energy is typically so much larger than the gap size that the excitation spectrum in the vortex can be regarded as continuous (see also ref. [189]). However, there may also exist superconductors where the lifetime broadening of the bound states is less than their energy separation ($\frac{\hbar}{\tau} < \frac{\Delta^2}{E_F}$), in which case the excitation spectrum must be regarded as quantized. In this "quantum limit" regime, new vortex properties are expected such as strong particle-hole asymmetry, which would be visible in the LDOS at the vortex center, and the existence of a Friedel-like oscillation around the vortex core [182]. Though no conventional, phonon-mediated superconductors have been found with quantum limit properties, there is reason to believe that some iron-based superconductors may be close to the quantum limit. One reason for this expectation is the relatively large gap size in these materials.

The scattering of quasiparticles in a vortex is an important physical process for SI-STM experimental methodology. Depending on the average quasiparticle lifetime τ, vortex scattering centers can be classified into one of two regimes. The clean regime exists where lifetime broadening is less than the size of the superconducting gap ($\frac{\hbar}{\tau} < \Delta$) - or, stated differently, where the mean free path is greater than the superconducting coherence length ($l > \xi$). In this regime, quasiparticles can travel from one side of a vortex to the other without being scattered. In the so-called dirty regime, on the other hand, where $\frac{\hbar}{\tau} > \Delta$ and $l < \xi$, quasiparticles are frequently scattered in the core of the vortex, which can then be approximated to a normal metal in its properties. A characteristic feature of a clean vortex is an energy peak in its local density of states near the Fermi energy. This energy peak is caused by the localization of low energy bound states at the vortex core, and was first observed by Hess *et al.* in $NbSe_2$ [190]. The bound state peak is formed due to multiple Andreev reflection [191, 192] and is predicted to change dramatically with the addition of each additional flux quantum to the vortex [193]. Subsequent theoretical work has suggested that the shape of the peak is determined not only by the normal state band structure but also by the dimensions of the supercon-

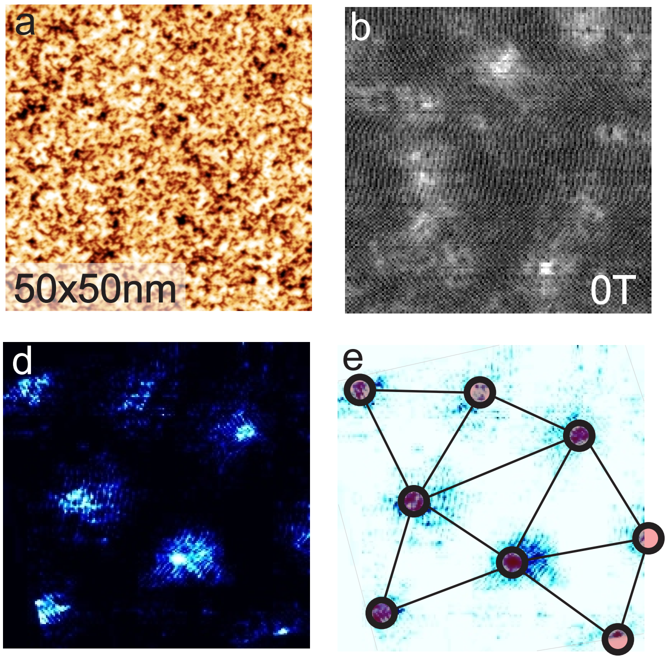

Figure 7.1: (a) Topographic image of a 50×50nm region of $Fe_{1.00}Se_{0.4}Te_{0.6}$. (b),(c) Fermi level layers from maps taken at 0T and 5T, respectively. (d) The vortex lattice has been isolated through subtraction of the 0T Fermi level layer from the 5T Fermi level layer. (d) The vortex lattice has been marked and lines have been drawn connecting each vortex to its nearest neighbors. (f) Two-dimensional autocorrelation function calculated from the vortex lattice.

ducting gap [194–197]. In this study, bound states are observed in the vortices in $Fe_{1.00}Se_{0.4}Te_{0.6}$, suggesting that this material can be classified as a “clean” vortex scatterer.

To date, spectroscopic imaging investigations of Abrikosov vortices have been published for several iron-based superconductors, including $BaFe_{1.8}Co_{0.2}As_2$ [152], $Ba_{0.6}K_{0.4}Fe_2As_2$ [133], FeSe [145], and LiFeAs [189]. In addition, the peak near the Fermi energy which is associated with bound states has been detected in several of these [133, 145, 189]. Still, in the iron-based superconductors the interactions between quasiparticles, vortices, and the superconducting gap have not been fully characterized and remain the object of ongoing research.

7.4 Imaging the vortex lattice

The Abrikosov vortex can be imagined as a gapless, non-superconducting potential well surrounded by a gapped, superconducting region. States can exist inside the vortex which can be measured with SI-STM, and which contain information about superconductivity in the material. In the case of the iron-based superconductors, characteristic features such as relatively high T_c, multiband electronic structure, small carrier density, and possible sign reversal in the superconducting order parameter, could result in the formation of unusual quasiparticle states in and around the vortices [189], possibly into the quantum-limit [182].

In this study, Abrikosov vortices were imaged with SI-STM on the iron chalcogenide superconductor $\mathrm{Fe_{1.00}Se_{0.4}Te_{0.6}}$. First, a $g(\mathbf{r}, E)$ map was taken at 5T over a 50×50nm, impurity-free region, which is shown in fig. 7.1 (a). Based on eq. 7.1, at 5T we expect to find around 6 cores in a region of this size. Next, the magnetic field was turned off and the same region was mapped at 0T. After acquiring the two $g(\mathbf{r}, E)$ maps in the same field of view we can isolate any vortices by subtracting the 0T map from the 5T map. The layers taken at the Fermi level in the 0T and 5T maps are shown in fig. 7.1 (b) and (c), respectively. In these images, the bright spots mark places with an elevated DOS at the Fermi level, which could be due to impurities or defects, but will in the 5T map also mark the positions of vortices. In fig. 7.1 (d), the result of subtracting the 0T Fermi level map layer from the corresponding 5T layer is shown, revealing several vortices. In fig. 7.1 (e), I have marked the vortices and drawn lines connecting each vortex with its nearest neighbors. A total of 8 vortices are found, two of which are only partially visible, arranged in what appears to be a rough hexagonal lattice. The two-dimensional autocorrelation function of the vortex lattice, which shows that the dominant lattice symmetry is indeed hexagonal, can be seen in fig. 7.1 (f). Previous work on the geometric configuration of vortex lattices in iron-based superconductors (see, e.g., [189]) has suggested a relatively loose hexagonal structure with under and over-coordinated vortices, resulting in the inclusion of pentagon, heptagon, and other coordinations in the larger-scale pattern. The density of non-hexagonal coordinations does not seem to depend strongly on the strength of the magnetic field, apart from at the extremes.

7.5 Energy evolution

Now that we have identified and roughly characterized the 5T vortex lattice on a 50×50nm region of $\mathrm{Fe_{1.00}Se_{0.4}Te_{0.6}}$, I will examine an individual vortex core. Previous observations of Abrikosov vortices in different materials have revealed material specific, spatially extended shapes which evolve as a function of energy. For

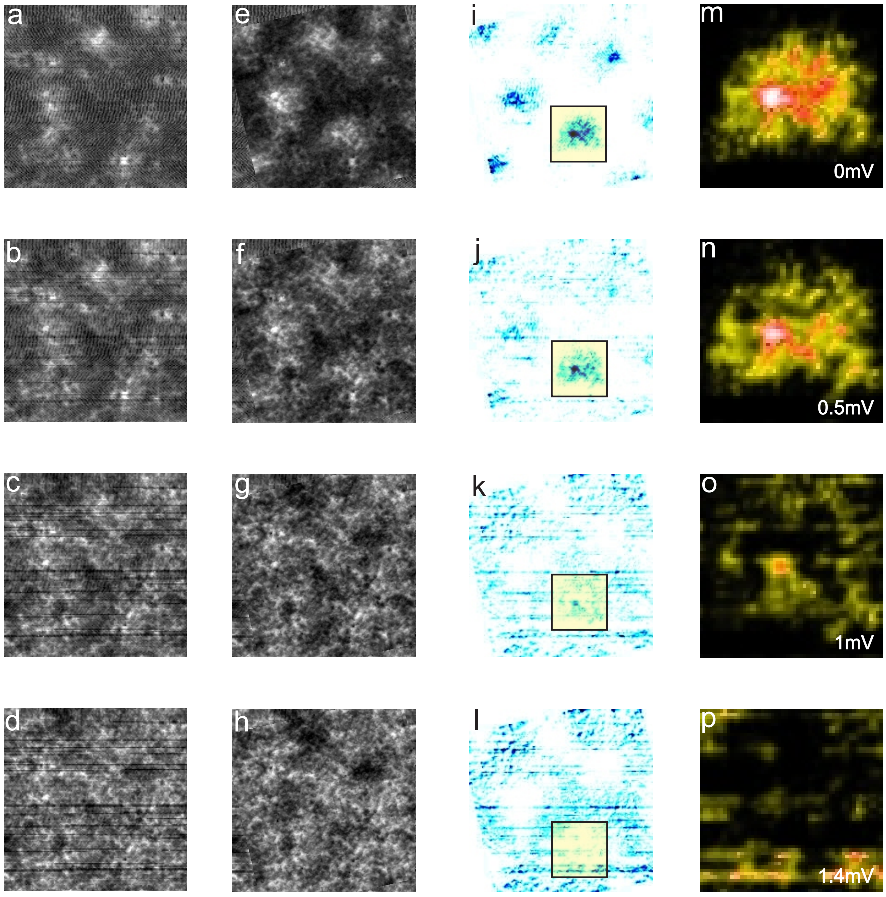

Figure 7.2: The spatial evolution of a single vortex core as a function of energy. (a)-(d) Energy cuts at 0mV, 0.5mV, 1mV, and 1.4mV, respectively, from the $g(\mathbf{r}, E)$ map taken at 0T. (e)-(h) The same energy cuts from the map taken at 5T. (i)-(l) The vortex lattice in the 50×50nm region, isolated by subtracting each 0T map layer from the corresponding 5T map layer. (m)-(p) Evolution of a single vortex as a function of energy.

example, early $g(\mathbf{r}, E)$ maps taken on $NbSe_2$ revealed 6-fold symmetric, star-like shapes [190]. More recent work on the stoichiometric iron-based superconductor LiFeAs has revealed 4-fold symmetric shapes around the vortex cores [189]. Moving away from the Fermi energy, both the 6-fold and 4-fold symmetry shapes undergo a spatial expansion before eventually disappearing. Theoretical origins for these shapes have been proposed on the basis of the vortex lattice [194, 195], the superconducting gap [196, 197], and the Fermi surface [194, 195, 198].

In order to show the evolution of the vortex lattice as a function of energy, we have performed the same analysis as in the previous section for several energies. In fig. 7.2 (a)-(d) and (e)-(h), the 0mV, 0.5mV, 1mV, and 1.4mV layers from the $g(\mathbf{r},E)$ maps taken at 0T and 5T, respectively, are shown. In fig. 7.2 (i)-(l) and (m)-(p), the evolution of the whole vortex lattice and of a single vortex, respectively, are shown. The single vortex has been enhanced in size and color saturation for clarity. The vortices are clearly visible at the Fermi level, much weaker at 0.5mV, and all but absent at energies greater than 1mV. In this data, the increase in size and concomitant weakening of the signal reported in the literature [189, 190] are observed, but the shape and symmetry of the vortices remain unclear.

7.6 Coherence length

In the foregoing I have examined the formation of the vortex lattice and the evolution of an individual vortex core as a function of energy. I will now characterize the size of the vortices, which will also give us a measure of the superconducting coherence length. To do this, I again take the Fermi level layer of the 5T $g(\mathbf{r},E)$ map. In addition, I will examine the evolution of the LDOS as a function of distance from the vortex core. As we move from a region far from any vortex core we expect to find an open superconducting gap which gradually narrows with increasing vortex proximity until it closes completely near the center of the core. However, differences may exist between different materials with respect to vortex size, the evolution of the gap as a function of distance, and especially in the spectral signature associated with the cores. For example, some recent studies of iron-based superconductors have detected bound states near the center of vortex cores [133, 145, 189]. Bound states are generally associated with a large peak in the LDOS near the Fermi energy, a flattening of coherence peaks, and a destruction of gap features at all energies inside the core. Lost gap features in the LDOS reappear as a function of distance from the core.

To estimate the size of the vortices, I have taken linecuts from the Fermi energy layer and fitted the LDOS peaks with a Gaussian. The resulting half-width-at-half-maximum (HWHM) values will be a useful measure of the vortex radius. In fig. 7.3 (a), the Fermi level layer from the 5T $g(\mathbf{r},E)$ map is shown, with vertical and horizontal linecuts across 4 vortex cores indicated. In fig. 7.3 (b), the autocorrelation of the vortex lattice is shown, also bisected with linecuts. In fig. 7.3 (c),(d), and (e), the four horizontal and four vertical vortex linecuts, respectively, as well as the two autocorrelation linecuts, are shown. The linecuts in fig. 7.3 (c) and (d) have been fitted with a Gaussian. The linecuts in fig. 7.3 (e) has been fitted with the following equation [199]:

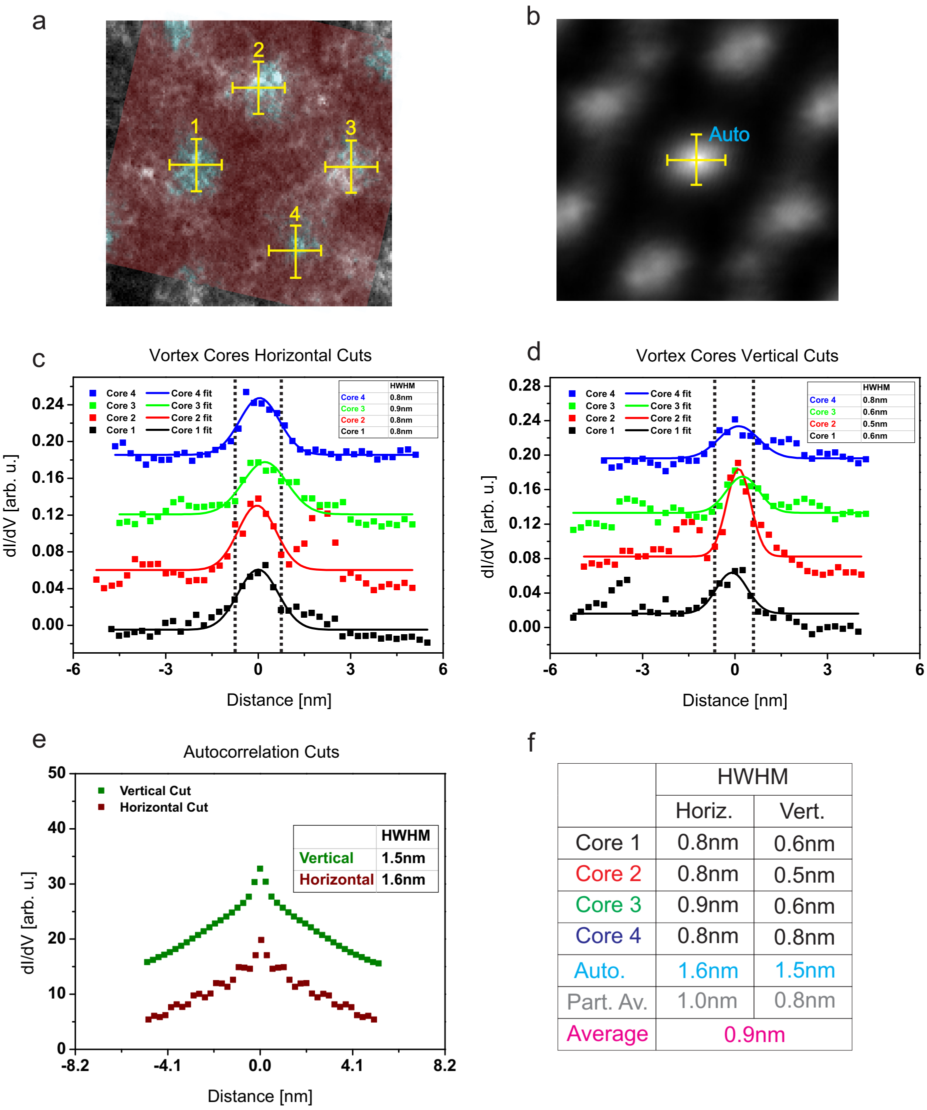

	HWHM	
	Horiz.	Vert.
Core 1	0.8nm	0.6nm
Core 2	0.8nm	0.5nm
Core 3	0.9nm	0.6nm
Core 4	0.8nm	0.8nm
Auto.	1.6nm	1.5nm
Part. Av.	1.0nm	0.8nm
Average	0.9nm	

Figure 7.3: The vortex radius is estimated by measuring several half-width-at-half-maximum (HWHM) values. The HWHM values are taken from Gaussian fits of dI/dV linecuts, which have been taken from the 5T Fermi level map layer. The linecuts bisect several vortex cores as well as the 2D autocorrelation function of the isolated vortex lattice. (a) The Fermi level layer of the 50×50nm map taken at 5T, overlaid with the previously identified vortex positions. The positions of horizontal and vertical linecuts across 4 vortices are marked. (b) Two-dimensional autocorrelation function of the underlying Fermi level map layer. The linecuts are marked. (c) Horizontal linecuts of dI/dV values as a function of distance across 4 individual vortex cores. The linecuts are fitted with eq. 7.2 to determine HWHM values. (d) Vertical linecuts across the same vortices. (e) Vertical and horizontal linecuts across the 2D autocorrelation function of the map layer. The linecuts have been fitted with a Gaussian in order to determine their HWHM values. (f) A table summarizing the vortex radius findings. Based on the HWHM values of the fitted linecuts, the vortices appear to have an average size of ≈ 0.9nm.

Material	**Parameters** ξ, V_{HWHM}	Δ_1, Δ_2	Study
$BaFe_{1.8}Co_{0.2}As_2$	2.76nm, **n/s**	6.25meV, **n/a**	Yin [152]
$Ba_{0.6}K_{0.4}Fe_2As_2$	2.1nm, ~2nm	2.2meV, 5.1meV	Shan [133]
FeSe	**n/s**, ~4nm	2.2meV, **n/a**	Song [145]
LiFeAs	4.64nm, 2.8nm	2.9meV, 6.0meV	Hanaguri [189]
$FeSe_{0.4}Te_{0.6}$	1.5-3.0nm, 0.9nm	2.5meV, 5.2meV	White

Table 7.1: Reference values from several vortex studies in the literature, where $\xi(T = 0\text{K})$ is the coherence length, $V_{HWHM}(T = 4.2\text{K})$ is the HWHM value of a Fermi level dI/dV linecut fit, Δ_1 is the first gap (F_E to coherence peak), and Δ_2 is the second gap (if present). The mean free path was given only for $BaFe_{1.8}Co_{0.2}As_2$, $l = 8.1nm$ [152].

$$\sigma(r, 0) = \sigma_0 + (1 - \sigma_0) \times (1 - \tanh(r/(\sqrt{2}\xi))), \tag{7.2}$$

In fig. 7.3 (f), the HWHM result from each linecut has been tabulated. Though there is some significant variation between the linecuts, the HWHM results from the dI/dV data show a relatively consistent vortex size, with an average value of 0.7nm in a range from 0.5 – 0.9nm. If we include the autocorrelation linecuts, of size 1.5 and 1.6nm, the average radius increases to 0.9nm. Either way, these vortices appears significantly smaller than those observed in recent studies on other materials. For comparison, some values from the literature are given in table 7.1.

7.7 Scattering

In order to investigate Andreev bound states, I will now examine the LDOS as a function of distance from the center of a vortex core. In fig. 7.4 (a), the Fermi level layer from the 5T $g(\mathbf{r}, E)$ map is shown. Arrows mark the positions of spectra linecuts. In fig. 7.4 (b), averaged spectra from two positions on the 5T map are plotted in red. An averaged dI/dV spectrum immediately surrounding a vortex core is plotted in the large view, while an average spectrum far from any vortices is plotted in the inset. The spectra corresponding to the same positions in the 0T map are plotted in black. The spectrum taken away from any core shows very little change between 0 and 5T, while the spectrum taken in the proximity of the core shows a large change near the Fermi energy. In order to better visualize the change in LDOS close to the core, the 0T spectrum has been subtracted from the 5T spectrum and the result plotted in purple. A peak at the Fermi energy is clearly visible, suggesting the presence of Andreev bound states. However, we do not observe a significant supression of the coherence peaks in the proximity of the

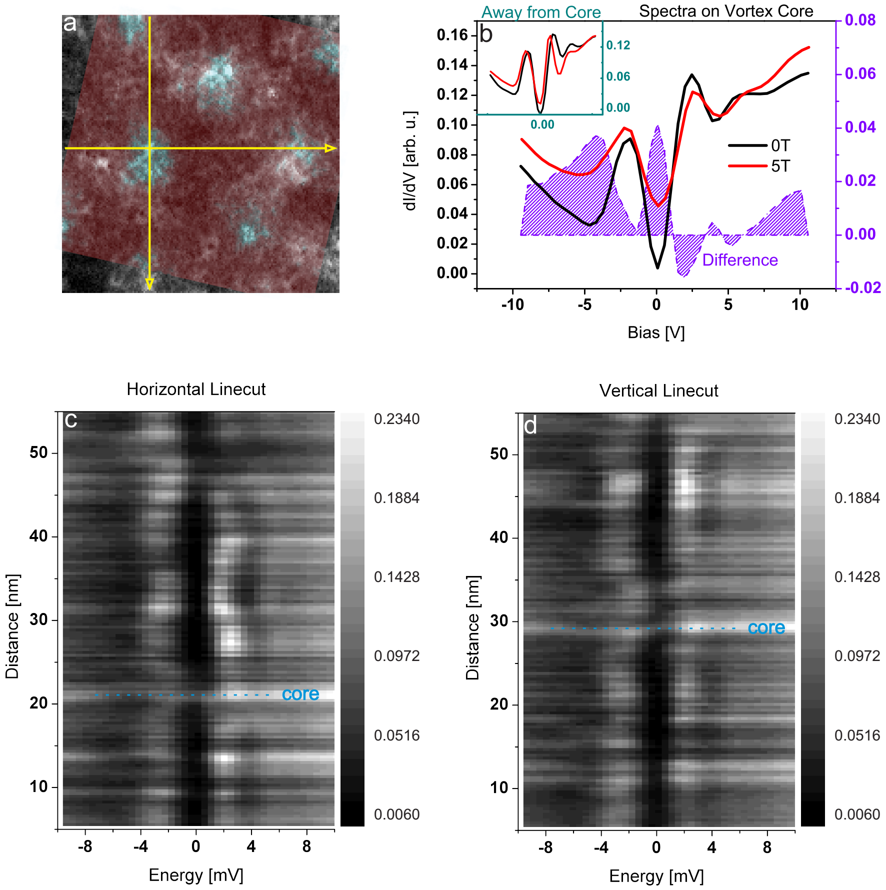

Figure 7.4: Andreev bound states in a vortex core, and LDOS as a function of distance. (a) The Fermi level layer of the 50×50nm map taken at 5T. The positions of one vertical and one horizontal linecut are marked. (b) Comparison of spectra, averaged over ≈ 1nm^2 around the maximum of the marked vortex core at 5T, and at the same position at 0T. In the inset, the same comparison is done for a region away from any vortex core. (c),(d) Spectra linecuts across the marked vortex core, horizontal and vertical.

vortex core. One possible contributing factor is the small size of vortices in this material. In fig. 7.4 (c) and (d), spectra linecuts from the 5T map are plotted as a function of distance from the core. The two cuts bisect (as close as possible given our spatial resolution) the center of the vortex core. In the resulting images, we can see that the gap is never completely suppressed. The spectrum with the highest LDOS at the Fermi level is presumed to be closest to the core and has been identified by a dotted line.

7.8 Conclusion

In conclusion, I have presented a study of Abrikosov vortices in $Fe_{1.00}Se_{0.4}Te_{0.6}$. The vortex size, which is related to the superconducting coherence length, was found to be small in this material compared to what has been reported for other iron-based superconductors. The relatively small vortex size could help explain why full gap supression is not observed in the $g(\mathbf{r}, E)$ data. Andreev bound states have been observed, suggesting that this material can be classified as a "clean" vortex scatterer. Given the small coherence length of around 0.9nm, and the presumably much larger mean free path, this is not surprising.

Chapter 8

Conclusion

In this work, I have used SI-STM to investigate high T_c superconductivity in iron-based materials. Before performing the presented experiments, I helped to design and construct a new STM, which has been optimized for spectroscopic imaging functionality. The instrument includes some new design elements, with the most important innovation being a measurement head made out of sapphire [10]. Other customized instrument components include parts of the cryogenic and vibration isolation systems, the high voltage amplifier, and the spectroscopic imaging measurement software. Test measurements have shown that the overall noise level of the instrument is very low (in the published account less than 1pm in the vertical direction, but at the time of writing the noise level has been reduced to less than 300fm). Instrument operation has been successfully demonstrated at temperatures down to 1.6K, and in magnetic fields of up to 14T. All together, the design and construction process took less than two years, with the actual construction and testing only taking around half a year. Attempting to construct a measurement head out of sapphire was perhaps the most daring part of the construction and, as the contracted company was initially unsure of their ability to machine the material, multiple heads were produced. In the end, there were no significant difficulties and three sapphire heads were delivered, all of which have since been built into new STMs. Given the lack of problems, and considering the superior mechanical and thermal properties of sapphire compared with alternative materials, I would not be surprised if it were to become a standard material for scanning probe instruments with high stability requirements.

Once the new instrument was successfully tested, SI-STM studies were conducted on several iron-based superconductors, the results of which are described in the body of this work. In the final presentation, the main focus was on the iron chalcogenide family, i.e. $Fe_{1+\delta}Se_xTe_{1-x}$, with a secondary focus on the iron pnictide $Ba_{0.68}K_{0.32}Fe_2As_2$. I would like to note that several other correlated electron materials were studied in this work which are not discussed in the text. These materials include the stoichiometric iron pnictide superconductor LiFeAs and the alleged topological superconductor $Cu_xBi_{2-x}Se_3$. I chose not to include the results of these studies in order to keep a more narrow focus. Also, by focusing on the family of iron-based superconductors with the simplest composition (the iron chalcogenides) the intent was to get as close as possible to the basics of iron-based superconductivity without being distracted by the more complicated lattice symmetries found in other families. In other words, instead of examining the properties of several different families of iron-based superconductors, the intent was to examine different aspects of iron-based superconductivity in one material family.

In the presented studies, one aim was to learn about the interplay between impurities and superconductivity in iron-based materials. This question is non-trivial and many others have attempted to address it using both experimental and theoretical approaches. At issue are the effects of magnetic and non-magnetic impurities on time-reversal symmetry, and their relation to the origin of iron-based superconductivity. In the presented study, I measured two iron chalcogenide samples, one of which contained many excess Fe impurities, $Fe_{1.04}Se_{0.28}Te_{0.72}$, and the other of which contained very few, $Fe_{1.00}Se_{0.4}Te_{0.6}$. The data indicate that two impurity species are present which can be differentiated according to their contribution to the local density of states. In fact, the LDOS signature of each impurity type is found to be highly specific over a large range of energies. Based on quantitative observations, it is found that the identities of the two impurity types are likely to be interstitial excess Fe, located on the obverse and reverse side of the first iron chalcogenide layer, respectively. The origin of the characteristic LDOS contributions of the two species, on either side of the Fermi energy, remains unclear. However, one thing which is clear is the devastating effect of excess Fe impurities on superconductivity in this compound. For example, the sample with many impurities had an extremely low superconducting volume fraction while the sample with few impurities showed a well-developed superconducting gap. The balance of evidence from this study suggests that the excess Fe impurities in this compound break time-reversal symmetry. As a consequence of this, the presence of each marginal impurity represents an additional scatterer, and this results in a rapid destruction of superconductivity as a function of increasing excess Fe concentration. In the study, I was unable to directly determine whether the excess Fe impurities are magnetic or non-magnetic scatterers, but neutron scattering and Knight shift data in the literature suggest that they are magnetic. As this question cuts to the heart of the issue, the interplay between magnetic scatterers and superconductivity in iron-based materials would be interesting to revisit in future experiments.

In another study, spatial inhomogeneities of the superconducting gap were considered. In $Fe_{1.00}Se_{0.4}Te_{0.6}$, regions with homogenous gap size on the order of 8nm in diameter were found, while in $Ba_{0.68}K_{0.32}Fe_2As_2$ similar homogenous regions of 1nm in size were found. In the first material, a weak correlation of local gap size with the concentration of surface chalcogens Se and Te, or rather with the height of the surface, is found. Temperature dependent measurements indicate that what is observed is really an inhomogeneity in the superconducting transition temperature. From a comparison of tunneling spectra with calculated spectra for different superconducting order parameters (s-wave, anisotropic s-wave, and d-wave) best agreement is found for an order parameter with anisotropic s-wave symmetry. In the second material, a double gap structure is found, with one gap size in reasonable agreement with literature values [132, 136]. A large asymmetry around the Fermi energy is found in the larger gap. On the surface, a pattern is found in which small regions showing a well-pronounced superconducting gap are surrounded by a larger region showing a gap with suppressed coherence peaks. One interpretation is that the superconducting regions are centered around K atoms, which are the chemical dopant in the material. Another interpretation is that we are observing a matrix-element effect caused by spatially dependent coupling of the tip to superconductivity in the sample. These findings give us some idea of the superconducting coherence lengths in these two materials, while also showing the effects of local impurities in the iron pnictide. While the focus here was on the iron chalcogenide, in the future it would be interesting to spend more time studying the iron pnictide material.

The presence of nematic electronic states in iron chalcogenide superconductors has previously been reported in the literature. In order to substantiate these reports, I have investigated $Fe_{1.00}Se_{0.4}Te_{0.6}$ for signs of electronic nematicity. Temperature dependent measurements confirm the existence of $C_4 \rightarrow C_2$ symmetry-broken states in the superconducting material and reveal that they persist above T_c. Since $Fe_{1.00}Se_{0.4}Te_{0.6}$ is reported to be tetragonal throughout the investigated temperature range, the symmetry-broken states do not appear to coincide with the tetragonal-to-orthorhombic crystal lattice symmetry breaking seen elsewhere in the phase diagram. As a possible origin of these symmetry-broken states, orbital ordering is suggested. The intensity of the nematic states is found to correlate negatively with the local size of the superconducting gap, suggesting a competitive relationship with superconductivity. A better understanding of the origin of the observed electronic nematicity and its relationship with superconductivity could likely help in solving the puzzle of high T_c superconductivity in this material.

The study of Abrikosov vortices allows us to look at an intermediate phase between normal conductivity and the superconducting state. Properties such as size, shape, energy evolution, and lattice symmetry can provide a substantial amount of information about the physics of the system. A final aim in this work was therefore to study Abrikosov vortices in $Fe_{1.00}Se_{0.4}Te_{0.6}$. This was done by measuring the sample under application of a 5T magnetic field and comparing with data taken at zero field. The average vortex size, and therefore the superconducting coherence length, is found to be small in this material, about 0.9nm. A full suppression of the gap inside the vortex cores was not observed. However, a peak was observed at the Fermi energy, indicating the presence of bound states in the vortex core. It is suggested that, given the small size of the vortices, this material likely has a longer mean free path than coherence length and thus lives in the clean scattering regime. It is clear that much more can be learned from the study of Abrikosov vortices in this material, as well as in other iron-based superconductors. However, additional measurements in higher fields and over larger areas would be helpful in forming the basis for further analysis.

Taken together, my findings reaffirm some previous findings in the literature and challenge others, but there are still too many pieces missing to try to put together the entire puzzle of superconductivity in iron-based materials. In general, I see no evidence in my findings to contradict the dominant view in the community, namely that iron-based superconductivity is likely related to magnetism, with spin fluctuations the most likely pairing mechanism. However, it is important to state that this dominant view remains unproven. In fact, not only does the mechanism behind iron-based superconductivity remain inconclusive, but the pairing symmetry remains unknown as well. In various materials, several order parameters have been suggested, including p-wave, d-wave, and $s_{\pm}$-wave. It is even speculated that there may be materials in which combinations of symmetries coexist. Despite the considerable efforts of the theory community, no successful predictive theory for high T_c superconductors yet exists. What is known is that the unconventional pairing mechanism is based on electron-electron interactions, which in the case of the iron-based materials can clearly sustain superconductivity up to much higher temperatures than is possible with electron-phonon coupling (though this may not be the case in other materials). There is also the characteristic layered, quasi 2D structure found in many of the high T_c materials. In contrast, unconventional superconductors which are not layered, such as the heavy fermions, often have very low transition temperatures. Finally, there is the perplexing diversity in pairing symmetry, which is not present in conventional superconductors. For my part, boiling down the most important results of this work, I would like to mention the following points: There was observed a drastic suppression of superconductivity due to an increased concentration of excess Fe impurities in $\mathrm{Fe}_{1+\delta}\mathrm{Se}_x\mathrm{Te}_{1-x}$. The inhomogeneity of the gap size observed in $\mathrm{Fe}_{1.00}\mathrm{Se}_{0.4}\mathrm{Te}_{0.6}$ and $\mathrm{Ba}_{0.68}\mathrm{K}_{0.32}\mathrm{Fe}_2\mathrm{As}_2$ offer further evidence of a strong local dependency on doping, perhaps indicative of localized pairing mediation; it is now clear that gap imhomogeneity must be taken into account in any theoretical description of superconductivity in these materials. The observed negative correlation between nematic electronic states and superconductivity suggests the presence of an exotic pairing symmetry unseen in previous materials, though the precise nature of this remains elusive. The very short superconducting coherence length in $Fe_{1.00}Se_{0.4}Te_{0.6}$ and its apparent identity as a clean regime scatterer also support a strong localization of superconductivity, certainly in the iron chalcogenides and perhaps also in iron-based superconductors generally.

In conclusion, despite the significant progress made in the characterization of these materials over the last few years, much remains to be done. It remains the case that from an experimental and especially technological point of view, in the absense of a predictive theory progress is likely to remain slow. For my own part, I am optimistic that the new SI-STM experiment I have constructed will continue to contribute to the study of correlated electron systems for years to come. SI-STM is an ideal technique for the investigation of these systems as both localized and delocalized electronic states can be addressed simultaneously. The instrument is one of only a handful of its kind in the world, and has been shown capable of producing a high quality of data. In the case of further improvements such as relocation to a dedicated, low-noise laboratory, increase of maximum measurement time via upgrade of the cryostat, or increase of the field strength via upgrade of the magnet, the setup might be made the peer of any other SI-STM experiment world-wide. As for the future of the iron-based superconductors and their possible technological utilization, in my view the example of FeSe is instructive: If an unknown, unconventional type of superconductivity can be stumbled upon, in the 21st century, in a binary compound which has been well-characterized for many years, there is really just no telling what could still be out there. The next major discovery might be just around the corner.

Acknowledgments

At last I would like to thank all those who have contributed in some way to this work and especially those whose essential contributions made it possible in the first place.

- Prof. Dr. Nicolas Grandjean, Prof. Dr. Davor Pavuna, Prof. Dr. Félix Baumberger, and Prof. Dr. Wulf Wulfhekel for graciously agreeing to examine my work.

- Prof. Dr. Klaus Kern for accepting me as a student and supporting me from the beginning to the end.

- Prof. Dr. Peter Lemmens for his large contribution to my undergraduate education.

- Dr. Chengtian Lin and the crystal growth service group for the provision of samples and other contributions.

- Dr. Vladimir Tsurkan and his co-workers in Augsburg for the provision of samples.

- Dr. Joseph Law and Dr. Linas Vilčiauskas for their outstanding general contributions.

- Detlef Wimmer and the low temperature service for their contribution to instrumentation.

- Thomas Frey and the central mechanical workshop for their contribution to instrumentation.

- Past and present members of the AG Peter Wahl, AG Peter Lemmens, Abt. Klaus Kern, MPI-FKF and MPI-IS who are too numerous to mention by name, but who nonetheless deserve acknowlegement for their unique individual contributions.

- Financial support by SPP1458 of the DFG.

Finally, I would like to thank a few of the people who have made the largest and most personal contributions. I would like to thank my wife Nasiba and my son Edwin, who are the lights of my life, for their infinite love and support. I would like to thank my parents, who, growing up, pushed me so far out of my comfort zone in the pursuit of academic achievement that I may never find my way back. Most of all, I would like to thank my mentor Dr. Peter Wahl, whose brilliance and unending patience were critically important for the success of this project, and who has been a great personal inspiration for me.

Publications

H. D. Yan, P. Lemmens, H. Dierke, S. C. White, F. Ludwig and M. Schilling, *Iron/Nickel Nanowire Growth in Anodic Aluminum Oxide Templates: Transfer of Length Scales and Periodicity*, J. Phys. Conf., **145**, 012079 (2009)

S. C. White, U. R. Singh and P. Wahl, *A Stiff Scanning Tunneling Microscopy Head for Measurement at Low Temperatures and in High Magnetic Fields*, Rev. Sci. Instrum., **82**, 113708, (2011)

Z. J. Li, Y. Liu, S. C. White, P. Wahl, X. M. Xie, M. H. Jiang and C. T. Lin, *Single Crystal Growth and Transport Properties of Cu-Doped Topological Insulator* Bi_2Se_3, Phys. Proced. **36**, 638-643, (2012)

U. R. Singh, M. Enayat, S. C. White and P. Wahl, *Construction and Performance of a Dilution-Refrigerator based Spectroscopic-Imaging Scanning Tunneling Microscope*, submitted

S. C. White, U. R. Singh, Y. Liu, C. T. Lin and P. Wahl, *Tunneling Spectroscopy of Excess Fe in* $Fe_{1+y}Se_xTe_{1-x}$, in preparation

U. R. Singh, S. C. White, S. Schmaus, V. Tsurkan, J. Deisenhofer, A. Loidl and P. Wahl, *Spatial Inhomogeneity of the Superconducting Gap in* $FeSe_{0.4}Te_{0.6}$, in preparation

U. R. Singh, S. C. White, S. Schmaus, V. Tsurkan, A. Loidl, J. Deisenhofer and P. Wahl, *Competition between Nematic Electronic States and Superconductivity in* $Fe_{1+y}Se_xTe_{1-x}$, in preparation

Curriculum Vitæ

Name	Seth Cullen White
Date of Birth	02.03.1985
Nationality	USA

2009-2013	Max-Planck-Institute for Solid State Research, Stuttgart, Germany, EU
2003-2008	Technische Universität Braunschweig, Braunschweig, Germany, EU; Dipl. Phys., *sehr gut*
1991-2003	A&M Consolidated High School, College Station ISD, College Station, Texas, USA; diploma, *magna cum laude*; National Merit Scholar

Bibliography

[1] J. E. Hoffman. *A search for alternative electronic order in the high temperature superconductor* $Bi_2Sr_2CaCu_2O_{8+\delta}$ *by scanning tunneling microscopy*. PhD thesis, University of California, Berkeley, 2003.

[2] H. K. Onnes. Communications from the physical laboratory of the university of leiden. 1911.

[3] G. Bednorz and K. A. Müller. Possible high T_c superconductivity in the Ba-La-Cu-O system. *Z. Phys. B*, 64:189, 1986.

[4] G. Binnig, H. Rohrer, C. Gerber, and E. Weibel. Surface studies by scanning tunneling microscopy. *Phys. Rev. Lett.*, 49:5761, 1982.

[5] R. Young, J. Ward, and F. Scire. The topografiner: An instrument for measuring surface microtopography. *Rev. Sci. Instrum.*, 43:999, 1972.

[6] J. A. Stroscio and W. J. Kaiser, editors. *Scanning Tunneling Microscopy*. Academic Press, Inc., 1993.

[7] J. Bardeen. Tunneling from a many-particle point of view. *Phys. Rev. Lett.*, 6:57, 1961.

[8] M. H. Cohen, L. M. Falicov, and J. C. Phillips. Superconductive tunneling. *Phys. Rev. Lett.*, 8:316318, 1962.

[9] N. D. Lang. Resistance of a one-atom contact in the scanning tunneling microscope. *Phys. Rev. B*, 36:8173, 1987.

[10] S. C. White, U. R. Singh, and P. Wahl. A stiff scanning tunneling microscopy head for measurement at low temperatures and in high magnetic fields. *Rev. Sci. Instrum.*, 82:113708, 2011.

[11] Scan piezo tube element #4 from EBL Products Inc.

[12] C. R. Ast, M. Assig, A. Ast, and K. Kern. Design criteria for scanning tunneling microscopes to reduce the response to external mechanical disturbances. *Rev. Sci. Instrum.*, 79:093704, 2008.

[13] S.-H. Pan, E. W. Hudson, and J. C. Davis. 3He refrigerator based very low temperature scanning tunneling microscope. *Rev. Sci. Instrum.*, 70:1459, 1999.

[14] *Data sheet for MACOR*. Corning Incorporated Lighting&Materials, Corning, New York 14831, USA, 2012.

[15] Cocreate modeling v. 16.0.0.712. Internal Database. FEM was done with the Finite Element Modeling Module.

[16] Frank Träger. *Handbook of Lasers and Optics*. Springer, 2007.

[17] J. W. Ekin. *Experimental techniques for low temperature measurements*. Oxford University Press, New York, 2006. The relative difference in thermal conductivity between sapphire and granular Al_2O_3 grows significantly between 300K and cryogenic temperatures, from about 1.5 up to ~100 times higher.

[18] S.-H. Pan. Patent wo 93/19494. Technical report, US Patent Office, 1993.

[19] Chr. Wittneven, R. Dombrowski, S.-H. Pan, and R. Wiesendanger. A low-temperature ultrahigh-vacuum scanning tunneling micropscope with rotatable magnetic field. *Rev. Sci. Instrum.*, 68:3806, 1997.

[20] Piezo stacks P-121.03 from Physik Instrumente Ceramic GmbH.

[21] G. Mariotto, M. D'Angelo, and I. V. Shvets. Dynamic behavior of a piezowalker, inertial and frictional configurations. *Rev. Sci. Instrum.*, 70:3651, 1999.

[22] Cernox 1030SD and 1050SD sensors from LakeShore Cryotronics, Inc.

[23] LakeShore temperature controller 336 from Cryophysics GmbH.

[24] External passive vibration isolation system I-2000-410 from Newport Spectra-Physics GmbH.

[25] SeisMonitor by Oyo Geospace, Houston, TX, USA.

[26] P. Zahl, M. Bierkandt, S. Schröder, and A. Klust. The flexible and modern open source scanning probe microscopy software package GXSM. *Rev. Sci. Instrum.*, 74:1222, 2003.

[27] P. Zahl, T. Wagner, R. Möller, and A. Klust. Open source scanning probe microscopy control software package GXSM. *J. Vac. Sci. Technol. B*, 28:C4E39, 2010.

[28] Soft dB Inc., Québec, Canada (http://www.softdb.com).

[29] Variable gain current amplifier FEMTO Messtechnik GmbH DLPCA-200.

[30] B. Giambattista, A. Johnson, and R. V. Coleman. Charge-density waves observed at 4.2K by scanning-tunneling microscopy. *Phys. Rev. B*, 37:2741, 1988.

[31] H. F. Hess, R. B. Robinson, R. C. Dynes, Jr. J. M. Valles, and J. V. Waszczak. Scanning-tunneling-microscope observation of the Abrikosov flux lattice and the density of states near and inside a fluxoid. *Phys. Rev. Lett.*, 62:215, 1989.

[32] Y. Noat, T. Cren, F. Debontridder, and D. Roditchev. Signatures of multi-gap superconductivity in tunneling spectroscopy. *Phys. Rev. B*, 82:014531, 2010.

[33] I. Guillamon, H. Suderow, F. Guinea, and S. Vieira. Intrinsic atomic-scale modulation of the superconduing gap of 2H-$NbSe_2$. *Phys. Rev. B*, 77:134505, 2008.

[34] R. C. Dynes, V. Narayanamurti, and J. P. Garno. Direct measurement of quasiparticle-lifetime broadening in a strong-coupled superconductor. *Phys. Rev. Lett.*, 41:1509, 1978.

[35] N. D. Lang. Spectroscopy of single atoms in the scanning tunneling microscope. *Phys. Rev. B*, 34:5947, 1986.

[36] F. London. The λ-phenomenon of liquid helium and the Bose-Einstein degeneracy. *Nature*, 141:643, 1938.

[37] F. London. On the Bose-Einstein condensation. *Phys. Rev.*, 54:947, 1938.

[38] W. Meissner and R. Ochsenfeld. Ein neuer Effekt bei Eintritt der Supraleitfähigkeit. *Naturwissenschaften*, 21:787, 1933.

[39] J. Bardeen, L. N. Cooper, and J. R. Schrieffer. Theory of superconductivity. *Phys. Rev.*, 108:1175, 1957.

[40] K. Andres, J. E. Graebner, and H. R. Ott. $4f$-virtual-bound-state formation in $CeAl_3$ at low temperatures. *Phys. Rev. Lett.*, 35:1779, 1975.

[41] F. Steglich, J. Aarts, C. D. Bredl, W. Lieke, D. Meschede, W. Franz, and H. Schäfer. Superconductivity in the presence of strong Pauli paramagnetism: $CeCu_2Si_2$. *Phys. Rev. Lett.*, 43:1892, 1979.

[42] H. v. Löhneysen, T. Pietrus, G. Portisch, H. G. Schlager, A. Schröder, M. Sieck, and T. Trappmann. Non-Fermi-liquid behavior in a heavy-fermion alloy at a magnetic instability. *Phys. Rev. Lett.*, 72:3262, 1994.

[43] U. R. Singh, M. Enayat, S. C. White, and P. Wahl. Construction and performance of a dilution-refrigerator based spectroscopic-imaging scanning tunneling microscope. *Rev. Sci. Instrum.*, 84:013708, 2013.

[44] Y. Kamihara, H. Hiramatsu, M. Hirano, R. Kawamura, H. Yanagi, T. Kamiya, and H. Hosono. Iron-based layered superconductor: LaOFeP. *J. Am. Chem. Soc.*, 128:10012, 2006.

[45] Y. Kamihara, T. Watanabe, M. Hirano, and H. Hosono. Iron-based layered superconductor La[$O_{1-x}F_x$]FeAs ($x = 0.05 - 0.12$) with $T_c = 26$K. *J. Am. Chem. Soc.*, 130:3296, 2008.

[46] H. Takahashi, K. Igawa, K. Arii, Y. Kamihara, M. Hirano, and H. Hosono. Superconductivity at 43K in an iron-based layered compound $La_{1-x}F_xFeAs$. *Nature*, 453:376, 2008.

[47] J. E. Hoffman. Spectroscopic scanning tunneling microscopy insights into Fe-based superconductors. *Reports on progress in physics*, 74:124513, 2011.

[48] L. N. Cooper. Bound electron pairs in a degenerate Fermi gas. *Phys. Rev.*, 104:1189, 1956.

[49] F. Gross, B. S. Chadrasekhar, D. Einzel, K. Andres, P. J. Hirschfeld, H. R. Ott, J. Beuers, Z. Fisk, and J. L. Smith. Anomalous temperature dependence of the magnetic field penetration depth in superconducting UBe_{13}. *Phys. B - Cond. Mat.*, 64:175, 1986.

[50] D. V. Evtushinsky, D. S. Inosov, V. B. Zabolotnyy, M. S. Viazovska, R. Khasanov, A. Amota, H.-H. Klauss, H. Luetkens, C. Niedermayer, G. L. Sun, V. Hinkov, C. T. Lin, A. Varykhalov, A. Koitzsch, M. Knupfer, B. Büchner, A. A. Kordyuk, and S. V. Borisenko. Momentum-resolved superconducting gap in the bulk of $Ba_{1-x}K_xFe_2As_2$ from combined ARPES and μSR measurements. *New J. Phys.*, 11:055069, 2009.

[51] P. Debye. Zur Theorie der spezifischen Wärme. *Annalen der Physik*, 39:789, 1912.

[52] G. M. Éliashberg. Interactions between electrons and lattice vibrations in a superconductor. *Soviet Phys. JETP*, 11:969, 1960.

[53] J. P. Carbotte. Properties of boson-exchange superconductors. *Rev. Mod. Phys.*, 62:1027, 1990.

[54] E. Maxwell. Isotope effect in the superconductivity of mercury. *Phys. Rev. Lett.*, 78:477, 1950.

[55] C. A. Reynolds, B. Serin, W. H. Wright, and L. B. Nesbitt. Superconductivity of isotopes of mercury. *Phys. Rev.*, 78:487, 1950.

[56] H. Ibach and H. Lüth. *Solid-State Physics - An Introduction to Principles of Materials Science*. Springer, New York, 3rd edition edition, 2003.

[57] K. M. Shen and J. C. S. Davis. Cuprate high-T_c superconductors. *Materials Today*, 11:14, 2008.

[58] W. J. Zhu, Y. Z. Huang, L. Q. Chen, C. Dong, B. Yin, and Z. Zhao. Synthesis of the superconductors $HgBa_2CaCu_2O_{6+\delta}$ and $HgBa_2Ca_2Cu_3O_{8+\delta}$. *Physica C*, 218:5, 1993.

[59] S. Hüfner, M. A. Hossain, A. Damascelli, and G. A. Sawatzky. Two gaps make a high-temperature superconductor? *Rev. Mod. Phys.*, 71:062501, 2008.

[60] E. Eremin, E. Tsoncheva, and A. V. Chubukov. Signature of the nonmonotonic d-wave gap in the electron-doped cuprates. *Phys. Rev. B*, 77:024508, 2008.

[61] G.-M. Zhao and J. Wang. Specific heat evidence for bulk s-wave gap symmetry of optimally electron-doped $Pr_{1.85}Ce_{0.15}CuO_{4-y}$ superconductors. *J. Phys. Cond. Mat.*, 22:352202, 2010.

[62] H. Won and K. Maki. d-wave superconductor as a model of high-t_c superconductors. *Phys. Rev. B*, 49:1397, 1994.

[63] F. Massee. *A tunneler's view on correlated oxides and iron based superconductors*. PhD thesis, Universiteit van Amsterdam, Amsterdam, 2011.

[64] J. Paglione and R. L. Green. High-temperature superconductivity in iron-based materials. *Nat. Phys.*, 6:645, 2010.

[65] N. Katayama, S. Ji, D. Louca, S. Lee, M. Fujita, T. J. Sato, J. Wen, Z. Xu, G. Gu, G. Xu, Z. Lin, M. Enoki, S. Chang, K. Yamada, and J. M. Tranquada. Investigation of the spin-glass regime between the antiferromagnetic and superconducting phases in $Fe_{1+y}Se_xTe_{1-x}$. *J. Phys. Soc. Jpn.*, 79:113702, 2010.

[66] Y. Mizuguchi and Y. Takano. Review of Fe chalcogenides as the simplest Fe-based superconductor. *J. Phys. Soc. Jpn.*, 79:102001, 2010.

[67] M. K. Wu, F. C. Hsu, K. W. Yeh, T. W. Huang, J. Y. Luo, M. J. Wang, H. H. Chang, T. K. Chen, S. M. Rao, B. H. Mok, C. L. Chen, Y. L. Huang, C. T. Ke, P. M. Wu, A. M. Chang, C. T. Wu, and T. P. Perng. The development of the superconducting PbO-type β-FeSe and related compounds. *Physica C*, 469:340, 2009.

[68] R. Khasanov, M. Bendele, A. Amato, P. Babkevitch, A. T. Boothroyd, A. Cervellino, K. Conder, S. N. Gvasaliya, H. Keller, H.-H. Klauss, H. Luetkens, V. Pomjakushina, and B. Roessli. Coexistence of incommensurate magnetism and superconductivity in $Fe_{1+y}Se_xTe_{1-x}$. *Phys. Rev. B*, 80:140511, 2009.

[69] C. Dong, H. Wang, Z. Li, J. Chen, H. Q. Yuan, and M. Fang. Revised phase diagram for the $FeTe_{1-x}Se_x$ system with fewer excess fe atoms. *Phys. Rev. B*, 84:224506, 2011.

[70] R. Viennois, E. Giannini, D. van der Marel, and R. Černý. Effect of Fe excess on structural, magnetic and superconducting properties of single-crystalline $Fe_{1+x}Te_{1-y}Se_y$. *J. Sol. State Chem.*, 183:769, 2010.

[71] S. Medvedev, T. M. McQueen, I. A. Troyan, T. Palasyuk, M. I. Eremets, R. J. Cava, S. Naghavi, F. Casper, V. Ksenofontov, G. Wortmann, and

C. Felser. Electronic and magnetic phase diagram of β-$Fe_{1.01}Se$ with superconductivity at 36.7K under pressure. *Nature Mater.*, 8:630, 2009.

[72] A. S. Sefat and D. J. Singh. Chemistry and electronic structure of iron-based superconductors. *MRS Bulletin*, 36:614, 2011.

[73] K. Terashima, Y. Sekiba, J. H. Bowen, K. Nakayama, T. Kawahara, T. Sato, P. Richard, Y.-M. Xu, L. J. Li, G. H. Cao, Z.-A. Xu, H. Ding, and T. Takahashi. Fermi surface nesting induced strong pairing in iron-based superconductors. *Proc. Nat. Acad. Sci.*, 106:7330, 2009.

[74] V. Brouet, M. Marsi, B. Mansart, A. Nicolaou, A. Taleb-Ibrahimi, P. L. Fèvre, F. Bertran, F. Rullier-Albenque, A. Forget, and D. Colson. Nesting between hole and electron pockets in $Ba(Fe_{1-x}Co_x)_2As_2$ ($x = 0 - 0.3$) observed with angle-resolved photoemission. *Phys. Rev. B*, 80:165115, 2009.

[75] M. Rotter, M. Tegel, and D. Johrendt. Superconductivity at 38 K in the iron arsenide $(Ba_{1-x}K_x)Fe_2As_2$. *Phys. Rev. Lett.*, 101:107006, 2008.

[76] A. S. Sefat, R. Jin, M. A. McGuire, B. C. Sales, D. J. Singh, and D. Mandrus. Superconductivity at 22 k in Co-doped $BaFe_2As_2$ crystals. *Phys. Rev. Lett.*, 101:117004, 2008.

[77] Z. Ren, Q. Tao, S. Jiang, C. Feng, C. Wang, J. Dai, G. Cao, and Z. Xu. Superconductivity induced by phosphorus doping and its coexistence with ferromagnetism in $EuFe_2(As_{0.7}P_{0.3})_2$. *Phys. Rev. Lett.*, 102:137002, 2009.

[78] W. Schnelle, A. Leithe-Jasper, R. Gumeniuk, U. Burkhardt, D. Kasinathan, and H. Rosner. Substitution-induced superconductivity in $SrFe_{2-x}Ru_xAs_2$ ($0.0 \leq x \leq 1.0$) and $CaFe_2As_{2-y}P_y$ ($0.0 \leq x \leq 0.3$). *Phys. Rev. B*, 79:214516, 2009.

[79] A. Maeda, T. Yabe, S. Takebayashi, M. Hase, and K. Uchinokura. Substitution of 3d metals for Cu in $Bi_2(Sr_{0.6}Ca_{0.4})_3Cu_2O_y$. *Phys. Rev. B*, 41:4112, 1990.

[80] K. Ishida, Y. Kitaoka, T. Yoshitomi, N. Ogata, T. Kamino, and K. Asayama. Gapless superconductivity in Zn-doped $YBa_2Cu_3O_7$ studied by Cu NMR and NQR. *Physica C*, 179:29, 1991.

[81] I. I. Mazin, D. J. Singh, M. D. Johannes, and M. H. Du. Unconventional superconductivity with a sign reversal in the order parameter of $LaFeAsO_{1-x}F_x$. *Phys. Rev. Lett.*, 101:057003, 2008.

[82] I. Mazin and J. Schmalian. Pairing symmetry and pairing state in ferropnictides, theoretical overview. *Physica C*, 469:614, 2009.

[83] S. de Jong, Y. Huang, R. Huisman, F. Massee, S. Thirupathaiah, M. Gorgoi, F. Schaefers, R. Follath, J. B. Goedkoop, and M. S. Golden. High resolution, hard x-ray photoemission investigation of $BaFe_2As_2$: Moderate influence of the surface and evidence for a low degree of Fe 3d - As 4p hybridization of electronic states near the Fermi energy. *Phy. Rev. B*, 79:115125, 2009.

[84] D. J. Singh. Electronic structure of Fe-based superconductors. *Physica C*, 469:418, 2009.

[85] H. Kontani and S. Onari. Orbital-fluctuation-mediated superconductivity in iron pnictides: Analysis of the five-orbital Hubbard-Holstein model. *Phys. Rev. Lett.*, 104:157001, 2010.

[86] E. A. Lynton, B. Serin, and M. Zucker. The superconducting critical temperature and the electronic specific heat of impure tin. *J. Phys. Chem. Solids*, 3:165, 1957.

[87] B. T. Matthias, H. Suhl, and E. Corenzwit. Spin exchange in superconductors. *Phys. Rev. Lett.*, 1:92, 1958.

[88] P. W. Anderson. Knight shift in superconductors. *Phys. Rev. Lett.*, 3:325, 1959.

[89] P. W. Anderson. Theory of dirty superconductors. *J. Phys. Chem. Solids*, 11:26, 1959.

[90] A. A. Abrikosov and L. P. Gor'kov. Contribution to the theory of superconducting alloys with paramagnetic impurities. *Soviet Phys. JETP*, 12:1243, 1961.

[91] D. Markowitz and L. P. Kadanoff. Effect of impurities upon critical temperature of anisotropic superconductors. *Phys. Rev.*, 131:563, 1963.

[92] F. Reif and M. A. Woolf. Energy gap in superconductors containing paramagnetic impurities. *Phys. Rev. Lett.*, 9:315, 1962.

[93] S. Skalski, O. Betbeder-Matibet, and P. R. Weiss. Properties of superconducting alloys containing paramagnetic impurities. *Phys. Rev.*, 136:1500, 1964.

[94] A. Yazdani, B. A. Jones, C. P. Lutz, M. F. Crommie, and D. M. Eigler. Probing the local effects of magnetic impurities on superconductivity. *Science*, 275:1767, 1997.

[95] I. I. Mazin and V. P. Antropov. Electronic structure, electron-phonon coupling, and multiband effects in MgB_2. *Physica C*, 385:49, 2003.

[96] L. Zhang, D. J. Singh, and M. H. Du. Density functional study of excess Fe in $Fe_{1+x}Te$: Magnetism and doping. *Phys. Rev. B*, 79:012506, 2009.

[97] J. Fink, S. Thirupathaiah, R. Ovsyannikov, H. A. Dürr, R. Follath, Y. Huang, S. de Jong, M. S. Golden, Y.-Z. Zhang, H. O. Jeschke, R. Valentí, C. Felser, S. D. Farahani, M. Rotter, and D. Johrendt. Electronic structure studies of $BaFe_2As_2$ by angle-resolved photoemission spectroscopy. *Phys. Rev. B*, 79:155118, 2009.

[98] M. P. Allan, T.-M. Chuang, F. Massee, Y. Xie, N. Ni, S. L. Bud'ko, G. S. Boebinger, Q. Wang, D. S. Dessau, P. C. Canfield, M. S. Golden, and J. C.

Davis. Anisotropic impurity states, quasiparticle scattering and nematic transport in underdoped Ca(Fe$_{1-x}$Co$_x$)$_2$As$_2$. *Nat. Phys.*, 9:220, 2013.

[99] M. L. Kulić and O. V. Dolgov. Anisotropic impurities in anisotropic superconductors. *Phys. Rev. B*, 60:13062, 1999.

[100] M. L. Kulić, S. L. Drechsler, and O. V. Dolgov. Conventional superconductivity in Fe-based pnictides: The relevance of intra-band electron-boson scattering. *EPL*, 85:47008, 2009.

[101] J. Li and Y. Wang. Magnetic impurities in the two-band $s_\pm$-wave superconductors. *EPL*, 88:17009, 2009.

[102] F.-C. Hsu, J.-Y. Luo, K.-W. Yeh, T.-K. Chen, T.-W. Huang, P. M. Wu, Y.-C. Lee, Y.-L. Huang, Y.-Y. Chu, D.-C. Yan, and M.-K. Wu. Superconductivity in the PbO-type structure α-FeSe. *Proc. Nat. Acad. Sci.*, 105:14262, 2008.

[103] T. M. McQueen, Q. Huang, K. Ksenofontov, C. Felser, Q. Xu, H. Zandbergen, Y. S. Hor, J. Allred, A. J. Williams, D. Qu, J. Checkelsky, N. P. Ong, and R. J. Cava. Extreme sensitivity of superconductivity to stoichiometry in Fe$_{1+\delta}$Se. *Phys. Rev. B*, 79:014522, 2009.

[104] P. Terzieff and K. L. Komarek. The paramagnetic properties of iron selenides with NiAs-type structure. *Monats Chem.*, 109:651, 1978.

[105] W. Schuster, H. Mimer, and K. L. Komarek. Transition metal-chalcogen systems, VII: The iron-selenium phase diagram. *Monats Chem.*, 110:1153, 1979.

[106] F. Massee, S. de Jong, Y. Huang, J. Kaas, E. van Heumen, J. B. Goedkoop, and M. S. Golden. Cleavage surfaces of the BaFe$_{2-x}$CO$_x$As$_2$ and Fe$_y$Se$_{1-x}$Te$_x$ superconductors: A combined STM plus LEED study. *Phys. Rev. B*, 80:140507, 2009.

[107] A. Tamai, A. Y. Ganin, E. Rozbicki, J. Bacsa, W. Meevansana, P. D. C. King, M. Caffio, R. Schaub, S. Margadonna, K. Prassides, M. J. Rossein-

sky, and F. Baumberger. Strong electron correlations in the normal state of the iron-based $FeSe_{0.42}Te_{0.58}$ superconductor observed by angle-resolved photoemission spectroscopy. *Phys. Rev. Lett.*, 104:097002, 2010.

[108] Y. Mizuguchi, Y. Hara, K. Deguchi, S. Tsuda, T. Yamaguchi, K Takeda, H. Kotegawa, H. Tou, and Y. Takano. Anion height dependence of T_c for the Fe-based superconductor. *Supercond. Sci. Technol.*, 23:054013, 2010.

[109] W.-F. Tsai, Y.-Y. Zhang, C. Fang, and J. Hu. Impurity-induced bound states in iron-based superconductors with s-wave $\cos k_x \cdot \cos k_y$ pairing symmetry. *Phys. Rev. B*, 80:064513, 2009.

[110] T. J. Liu, X. Ke, B. Qian, J. Hu, D. Fobes, E. K. Vehstedt, H. Pham, J. H. Yang, M. H. Fang, L. Spinu, P. Schiffer, Y. Liu, and Z. Q. Mao. Charge-carrier localization induced by excess Fe in the superconductor $Fe_{1+y}Te_{1-x}Se_x$. *Phys. Rev. B*, 80:174509, 2009.

[111] S. Rößler, D. Cherian, S. Harikrishnan, H. L. Bhat, S. Elizabeth, J. A. Mydosh, L. H. Tjeng, F. Steglich, and S. Wirth. Disorder-driven electronic localization and phase separation in superconducting $Fe_{1+y}Te_{0.5}Se_{0.5}$ single crystals. *Phys. Rev. B*, 82:144523, 2010.

[112] S. Khim, J. W. Kim, E. S. Choi, Y. Bang, M. Nohara, H. Takagi, and K. H. Kim. Evidence for dominant Pauli paramagnetic effect in the upper critical field of single-crystalline $FeTe_{0.6}Se_{0.4}$. *Phys. Rev. B*, 81:184511, 2010.

[113] Y. Koshika, T. Usui, S. Adachi, T. Watanabe, K. Sakano, S. Simayi, and M. Yoshizawa. Effects of annealing under tellurium vapor for $Fe_{1.03}Te_{0.8}Se_{0.2}$. *J. Phys. Soc. Jpn.*, 82:023703, 2013.

[114] A. Subedi, L. Zhang, D. J. Singh, and M. H. Du. Density functional study of FeS, FeSe, and FeTe: Electronic structure, magnetism, phonons and superconductivity. *Phys. Rev. B*, 78:134514, 2008.

[115] Y. Xia, D. Qian, L. Wray, D. Hsieh, G. F. Chen, J. L. Luo, N. L. Wang, and M. Z. Hasan. Fermi surface topology and low-lying quasiparticle dynamics of parent $Fe_{1+x}Te/Se$ superconductor. *Phys. Rev. Lett.*, 103:037002, 2009.

[116] D. Phelan, J. N. Millican, E. L. Thomas, J. B. Leão, Y. Qiu, and R. Paul. Neutron scattering measurements of the phonon density of states of $FeSe_{1-x}$ superconductors. *Phys. Rev. B*, 79:014519, 2009.

[117] H. Kotegawa, S. Masaki, Y. Awai, H. Tou, Y. Mizuguchi, and Y. Takano. Evidence for unconventional superconductivity in arsenic-free iron-based superconductor FeSe: A ^{7}7Se-NMR study. *J. Phys. Soc. Jpn.*, 77:113703, 2008.

[118] Y. Qiu, W. Bao, Y. Zhao, C. Broholm, V. Stanev, Z. Tesanovic, Y. C. Gasparovic, S. Chang, J. Hu, B. Qian, M. Fang, and Z. Mao. Spin gap and resonance at the nesting wave vector in superconducting $FeSe_{0.4}Te_{0.6}$. *Phys. Rev. Lett.*, 103:067008, 2009.

[119] T. Imai, K. Ahilan, F. L. Ning, T. M. McQueen, and R. J. Cava. Why does undoped FeSe become a high-T_c superconductor under pressure? *Phys. Rev. Lett.*, 102:177005, 2009.

[120] W. Bao, Y. Qiu, Q. Huang, M. A. Green, P. Zajdel, M. R. Fitzsimmons, M. Zhernenkov, S. Chang, M. Fang, B. Qian, E. K. Vehstedt, J. Yang, H. M. Pham, L. Spinu, and Z. Q. Mao. Tunable ($\delta\pi$, $\delta\pi$)-type antiferromagnetic order in α-Fe(Te,Se) superconductors. *Phys. Rev. Lett.*, 102:247001, 2009.

[121] G. F. Chen, Z. G. Chen, J. Dong, W. Z. Hu, G. Li, X. D. Zhang, P. Zheng, J. L. Luo, and N. L. Wang. Electronic properties of single-crystalline $Fe_{1.05}Te$ and $Fe_{1.05}Se_{0.30}Te_{0.70}$. *Phys. Rev. B*, 79:140509, 2009.

[122] M. D. Johannes and I. I. Mazin. Microscopic origin of magnetism and magnetig interactions in ferropnictides. *Phys. Rev. B*, 79:220510, 2009.

[123] A. M. Turner, F. Wang, and A. Vishwanath. Kinetic magnetism and orbital order in iron telluride. *Phys. Rev. B*, 80:224504, 2009.

[124] M. J. Han and S. Y. Savrasov. Doping driven (π,0) nesting and magnetic properties of $Fe_{1+x}Te$ superconductors. *Phys. Rev. Lett.*, 103:067001, 2009.

[125] C. Fang, B. A. Bernevig, and J. Hu. Theory of magnetic order in $Fe_{1+y}Se_{1-x}Te_x$. *EPL*, 86:67005, 2009.

[126] K. Seo, B. A. Bernevig, and J. Hu. Pairing symmetry in a two-orbital exchange coupling model of oxypnictides. *Phys. Rev. Lett.*, 101:206404, 2008.

[127] H. Shiba. Classical spins in superconductors. *Prog. Theor. Phys.*, 40:435, 1968.

[128] D. V. Evtushinsky, A. A. Kordyuk, V. B. Zabolotnyy, D. S. Inosov, T. K. Kim, B. Büchner, H. Luo, Z. Wang, H.-H. Wen, G. Sun, C. T. Lin, and S. V. Borisenko. Propeller-like low temperature Fermi surface of $Ba_{1-x}K_xFe_2As_2$ from magnetotransport and photoemission measurements. *J. Phys. Soc. Jpn.*, 80:023710, 2011.

[129] D. V. Evtushinsky, D. S. Inosov, V. B. Zabolotnyy, A. Koitzsch, M. Knupfer, B. Büchner, M. S. Viazovska, G. L. Sun, V. Hinkov, A. V. Boris, C. T. Lin, B. Keimer, A. Varykhalov, A. A. Kordyuk, and S. V. Borisenko. Momentum dependence of the superconducting gap in $Ba_{1-x}K_xFe_2As_2$. *Phys. Rev. B*, 79:054517, 2009.

[130] V. B. Zabolotnyy, D. S. Inosov, D. V. Evtushinsky, A. Koitzsch, A. A. Kordyuk, G. L. Sun, J. T. Park, D. Haug, V. Hinkov, A. V. Boris, C. T. Lin, M. Knupfer, A. N. Yaresko, B. Büchner A. Varykhalov, R. Follath, and S. V. Borisenko. (π, π) electronic order in iron arsenide superconductors. *Nature*, 457:569, 2009.

[131] J. T. Park, D. S. Inosov, Ch. Niedermayer, G. L. Sun, D. Haug, N. B. Christensen, R. Dinnebier, A. V. Boris, A. J. Drew, L. Schulz, T. Shapoval, U. Wolff, V. Neu, X. Yang, C. T. Lin, B. Keimer, and V. Hinkov. Electronic

phase separation in the slightly underdoped iron pnictide superconductor $Ba_{1-x}K_xFe_2As_2$. *Phys. Rev. Lett.*, 102:117006, 2009.

[132] R. Khasanov, D. V. Evtushinsky, A. Amato, H.-H. Klauss, H. Luetkens, Ch. Niedermayer, B. Büchner, G. L. Sun, C. T. Lin, J. T. Park, D. S. Inosov, and V. Hinkov. Two-gap superconductivity in $ba_{1-x}k_xfe_2as_2$: A complementary study of the magnetic penetration depth by muon-spin rotation and angle-resolved photoemission. *Phys. Rev. Lett.*, 102:187005, 2009.

[133] L. Shan, Y.-L. Wang, B. Shen, B. Zeng, Y. Huang, A. Li, D. Wang, H. Yang, C. Ren, Q.-H. Wang, S. H. Pan, and H.-H. Wen. Observation of ordered vortices with Andreev bound states in $Ba_{0.6}K_{0.4}Fe_2As_2$. *Nat. Phys.*, 7:325, 2011.

[134] H. Q. Yuan, J. Singleton, F. F. Balakirev, S. A. Baily, G. F. Chen, J. L. Luo, and N. L. Wang. Nearly isotropic superconductivity in $(Ba,K)Fe_2As_2$. *Nature*, 457:565, 2009.

[135] M. M. Altarawneh, K. Collar, and C. H. Mielke. Determination of anisotropic H_{c2} up to 60 T in $Ba_{0.55}K_{0.45})Fe_2As_2$. *Phys. Rev. B*, 78:220505, 2008.

[136] S. Takeshita and R. Kadono. Competition/coexistence of magnetism and superconductivity in iron pnictides probed by muon spin rotation. *New J. Phys.*, 11:035006, 2009.

[137] Y. Liu and C. T. Lin. A comparative study of $Fe_{1+\delta}Te_{1-x}Se_x$ single crystals grown by Bridgman and self flux techniques. *ZL50*, 24:183, 2011.

[138] V. Tsurkan, J. Deisenhofer, A. Günter, Ch. Kant, H.-A. Krug von Nidda, F. Schrettle, and A. Loidl. Physical properties of $FeSe_{0.5}Te_{0.5}$ single crystals grown under different conditions. *Euro. Phys. J. B*, 79:289, 2011.

[139] G. L. Sun, D. L. Sun, M. Konuma, P. Popovich, A. Boris, J. B. Peng, K.-Y. Choi, P. Lemmens, and C. T. Lin. Single crystal growth and effect of

doping on structural, transport and magnetic properties of $A_{1-x}K_xFe_2As_2$ (A=Ba,Sr). *J. Supercond. Nov. Magn.*, 24:1773, 2011.

[140] A. Charnukha, O. V. Dolgov, A. A. Golubov, Y. Matiks, D. L. Sun, C. T. Lin, B. Keimer, and A. V. Boris. Eliashberg approach to infrared anomalies induced by the superconducting state of $Ba_{0.68}K_{0.32}Fe_2As_2$ single crystals. *Phys. Rev. B*, 84:174511, 2011.

[141] X. He, G. Li, J. Zhang, A. B. Karki, R. Jin, B. C. Sales, A. S. Sefat, M. A. McGuire, D. Mandrus, and E. W. Plummer. Nanoscale chemical phase separation in $FeTe_{0.55}Se_{0.45}$ as seen via scanning tunneling spectroscopy. *Phys. Rev. B*, 83:220502, 2011.

[142] D. S. Inosov, J. T. Park, P. Bourges, D. L. Sun, Y. Sidis, A. Schneidewind, K. Hradil, D. Haug, C. T. Lin, B. Keimer, and V. Hinkov. Normal-state spin dynamics and temperature-dependent spin-resonance energy in optimally doped $BaFe_{1.85}Co_{0.15}As_2$. *Nat. Phys.*, 6:178, 2010.

[143] P. J. Hirschfeld, M. M. Korshunov, and I. I. Mazin. Gap symmetry and structure of Fe-based superconductors. *Rep. Prog. Phys.*, 74:124508, 2011.

[144] T. Hanaguri, S. Niitaka, K. Kuroki, and H. Takagi. Unconventional s-wave superconductivity in Fe(Se,Te). *Science*, 328:474, 2010.

[145] C.-L. Song, Y.-L. Wang, P. Cheng, Y.-P. Jiang, W. Li, T. Zhang, Z. Li, K. He, L. Wang, J.-F. Jia, H.-H. Hung, C. Wu, X. Ma, X. Chen, and Q.-K. Xue. Direct observation of nodes and twofold symmetry in FeSe superconductor. *Science*, 332:1410, 2011.

[146] K. Umezawa, Y. Li, H. Miao, K. Nakayama, Z.-H. Liu, P. Richard, T. Sato, J. B. He, D.-M. Wang, G. F. Chen, H. Ding, T. Takahashi, and S.-C. Wang. Unconventional anisotropic s-wave superconducting gaps of the LiFeAs iron-pnictide superconductor. *Phys. Rev. Lett.*, 108:037002, 2012.

[147] M. P. Allan, A. W. Rost, A. P. Mackenzie, Yang Xie, J. C. Davis, K. Kihou, C. H. Lee, A. Iyo, H. Eisaki, and T.-M. Chuang. Anisotropic energy gaps

of iron-based superconductivity from intraband quasiparticle interference in LiFeAs. *Science*, 336:563, 2012.

[148] C. Hess, S. Sykora, T. Hänke, R. Schlegel, D. Baumann, V. B. Zabolotnyy, L. Harnagea, S. Wurmehl, J. van den Brink, and B. Büchner. Interband quasiparticle scattering in superconducting LiFeAs reconciles photoemission and tunnling measurements. *Phys. Rev. Lett.*, 110:017006, 2013.

[149] H. Miao, P. Richard, Y. Tanaka, K. Nakayama, T. Qian, K. Umezawa, T. Sato, Y.-M. Xu, Y. B. Shi, N. Xu, X.-P. Wang, P. Zhang, H.-B. Yang, Z.-J. Xu, J. S. Wen, G.-D. Gu, X. Dai, J.-P. Hu, T. Takahashi, and H. Ding. Isotropic superconducting gaps with enhanced pairing on electron Fermi surfaces in $FeTe_{0.55}Se_{0.45}$. *Phys. Rev. B*, 85:094506, 2012.

[150] K. Okazaki, Y. Ito, Y. Ota, Y. Kotani, T. Shimojima, T. Kiss, S. Watanabe, C.-T. Chen, S. Niitaka, T. Hanaguri, H. Takagi, A. Chainani, and S. Shin. Evidence for a $\cos 4\phi$ modulation of the superconducting energy gap of optimally doped $FeTe_{0.6}Se_{0.4}$ single crystals using laser angle-resolved photoemission spectroscopy. *Phys. Rev. Lett.*, 109:237011, 2012.

[151] B. Zeng, G. Mu, H. Q. Luo, T. Xiang, I. I. Mazin, H. Yang, L. Shan, C. Ren, P. C. Dai, and H.-H. Wen. Anisotropic structure of the order parameter in $FeSe_{0.45}Te_{0.55}$ revealed by angle-resolved specific heat. *Nat. Commun.*, 1:112, 2010.

[152] Y. Yin, M. Zech, T. L. Williams, X. F. Wang, G. Wu, X. H. Chen, and J. E. Hoffman. Scanning tunneling spectroscopy and vortex imaging in the iron pnictide superconductor $BaFe_{1.8}Co_{0.2}As_2$. *Phys. Rev. Lett.*, 102:097002, 2009.

[153] T. Klein, D. Braithwaite, A. Demuer, W. Knafo, G. Lapertot, C. Marcenat, P. Rodière, I. Sheikin, P. Strobel, A. Sulpice, and P. Toulemonde. Thermodynamic phase diagram of $Fe(Te_{0.55}Se_{0.45})$ single crystals in fields up to 28 tesla. *Phys. Rev. B*, 82:184506, 2010.

[154] S. H. Pan, J. P. O'Neal, R. L. Badzey, C. Chamon, H. Ding, J. R. Engelbrecht, Z. Wang, H. Eisaki, S. Uchida, A. K. Gupta, K.-W. Ng, E. W. Hudson, K. M. Lang, and J. C. Davis. Microscopic electronic inhomogeneity in the high-T_c superconductor $Bi_2Sr_2CaCu_2O_{8+x}$. *Nature*, 413:282, 2001.

[155] K. M. Lang, V. Madhavan, J. E. Hoffman, E. W. Hudson, H. Eisaki, S. Uchida, and J. C. Davis. Imaging the granular structure of high-T_c superconductivity in underdoped $Bi_2Sr_2CaCu_2O_{8+\delta}$. *Nature*, 415:412, 2002.

[156] C. J. Chen, editor. *Introduction to scanning tunneling microscopy*. Oxford Uni. Press, New York, second edition edition, 2008.

[157] C. C. Homes, A. Akrap, J. S. Wen, Z. J. Xu, Z. W. Lin, Q. Li, and G. D. Gu. Electronic correlations and unusual superconducting response in the optical properties of the iron chalcogenide $FeTe_{0.55}Se_{0.45}$. *Phys. Rev. B*, 81:180508, 2010.

[158] M. Tinkham, editor. *Introduction to superconductivity*. Dover Publications, New York, second edition edition, 2004.

[159] Y. J. Uemura. Superfluid density of high-T_c cuprate systems: Implication on condensation mechanisms, heterogeneity and phase diagram. *Solid State Commun.*, 126:23, 2002.

[160] W. Lv and P. Phillips. Orbitally and magnetically induced anisotropy in iron-based superconductors. *Phys. Rev. B*, 84:174512, 2011.

[161] H. Zhai, F. Wang, and D.-H. Lee. Antiferromagnetically driven electronic correlations in iron pnictides and cuprates. *Phys. Rev. B*, 80:064517, 2009.

[162] W. Lv, J. Wu, and P. Phillips. Orbital ordering induces structural phase transition and the resistivity anomaly in iron pnictides. *Phys. Rev. B*, 80:224506, 2009.

[163] C.-C. Lee, W.-G. Yin, and W. Ku. Ferro-orbital order and strong magnetic anisotropy in the parent compounds of iron-pnictide superconductors. *Phys. Rev. Lett.*, 103:267001, 2009.

[164] C.-C. Chen, J. Maciejko, A. Sorini, B. Moritz, R. Singh, and T. P. Devereaux. Orbital order and spontaneous orthorhombicity in iron pnictides. *Phys. Rev. B*, 82:100504, 2010.

[165] W. Lv and P. Phillips. Orbitally and magnetically induced anisotropy in iron-based superconductors. *Phys. Rev. B*, 84:174512, 2011.

[166] C. Fang, H. Yao, W.-F. Tsai, J. Hu, and S. A. Kivelson. Theory of electron nematic order in LaFeAsO. *Phys. Rev. B*, 77:224509, 2008.

[167] C. Xu, M. Müller, and S. Sachdev. Ising and spin orders in the iron-based superconductors. *Phys. Rev. B*, 78:020501, 2008.

[168] T.-M. Chuang, M. P. Allen, J. Lee, Y. Xie, N. Ni, S. L. Bud'ko, G. S. Boebinger, P. C. Canfield, and J. C. Davis. Nematic electronic structure in the "parent" state of the iron-based superconductor $Ca(Fe_{1-x}Co_x)_2As_2$. *Science*, 327:181, 2010.

[169] S. A. Kivelson, E. Fradkin, and V. J. Emery. Electronic liquid-crystal phases of a doped Mott insulator. *Nature*, 393:550, 1998.

[170] A. I. Goldman, D. N. Argyriou, B. Ouladdiaf, T. Chatterji, A. Kreyssig, S. Nandi, N. Ni, S. L. Bud'ko, P. C. Canfield, and R. J. McQueeney. Lattice and magnetic instabilities in $CaFe_2As_2$: A single-crystal neutron diffraction study. *Phys. Rev. B*, 78:100506, 2008.

[171] M. Yi, L. Dongui, J.-H. Chu, J. G. Analytis, A. P. Sorini, A. F. Kemper, B. Moritz, S.-K. Mo, R. G. Moore, M. Hashimoto, W.-S. Lee, Z. Hussain, T. P. Devereaux, I. R. Fisher, and Z.-X. Shen. Symmetry-breaking orbital anisotropy observed for detwinned $Ba(Fe_{1-x}Co_x)_2As_2$ above the spin density wave transition. *Proc. Nat. Acad. Sci.*, 108:6878, 2011.

[172] M. Nakajima, T. Ljang, S. Ishida, Y. Tomioka, K. Kihou, C. H. Lee, A. Iyo, H. Eisaka, T. Kakeshita, T. Ito, and S. Uchida. Unprecedented anisotropic metallic state in undoped iron arsenide $BaFe_2As_2$ revealed by optical spectroscopy. *Proc. Nat. Acad. Sci.*, 108:12238, 2011.

[173] J.-H. Chu, J. G. Analytis, K. de Greve, P. L. McMahon, Z. Islam, Y. Yamamoto, and I. R. Fisher. In-plane resistivity anisotropy in an underdoped iron arsenide superconductor. *Science*, 329:824, 2010.

[174] N. C. Gresty, Y. Takabayashi, A. Y. Ganin, M. T. McDonald, J. B. Claridge, D. Giap, Y. Mizuguchi, Y. Takano, T. Kagayama, Y. Ohishi, M. Takata, M. J. Rosseinsky, S. Margadonna, and K. Prassides. Structural phase transitions and superconductivity in $Fe_{1+\delta}Se_{0.57}Te_{0.43}$ at ambient and elevated pressures. *J. Am. Chem. Soc.*, 131:16944, 2009.

[175] S. Graser, T. A. Maier, P. J. Hirschfeld, and D. J. Scalapino. Near-degeneracy of several pairing channels in multiorbital models for the Fe pnictides. *New J. Phys.*, 11:025016, 2009.

[176] A. B. Vorontsov, M. G. Vavilov, and A. V. Chubukov. Superconductivity and spin-density waves in multiband metals. *Phys. Rev. B*, 81:174538, 2010.

[177] R. M. Fernandes and J. Schmalian. Competing order and nature of the pairing state in the iron pnictides. *Phys. Rev. B*, 82:014521, 2010.

[178] R. M. Fernandes and J. Schmalian. Manifestations of nematic degrees of freedom in the magnetic, elastic, and superconducting properties of the iron pnictides. *Sci. Technol.*, 25:084005, 2012.

[179] A. A. Abrikosov. On the magnetic properties of superconductors of the second group. *J. Exptl. Theoret. Phys.*, 32:1442, 1957.

[180] N. B. Kopnin. Theory of superconductivity. Aalto University, School of Science and Technology, Department of Applied Physics, 2010.

[181] J. L. Chen and T. J. Yang. Flux flow of Abrikosov vortices in type-II superconductors. *Phys. Rev. B*, 50:319, 1994.

[182] N. Hayashi, T. Isoshima, M. Ichioka, and K. Machida. Low-lying quasiparticle excitations around a vortex core in quantum limit. *Phys. Rev. Lett.*, 80:2921, 1998.

[183] K. Miyahara, K. Mukaida, M. Tokumitsu, S. Kubo, and K. Hohkawa. Abrikosov vortex memory with improved sensitivity and reduced write current levels. *IEEE Trans. Mag.*, 23:875, 1987.

[184] S. M. M. Virtanen and M. M. Salomaa. Multiquantum vortices in superconductors: Electronic and scanning tunneling microscopy spectra. *Phys. Rev. B*, 60:14581, 1999.

[185] K. Tanaka, I. Robel, and B. Jankó. Electronic structure of multiquantum giant vortex states in mesoscopic superconducting disks. *Proc. Nat. Acad. Sci.*, 99:5233, 2002.

[186] T. Yamane, Y. Nagai, K. Tanaka, and N. Hayashi. Impurity scattering effect on the zero-energy peak of the local density of states in a multi-quantum vortex core. arXiv:1301.6445v1, 2013.

[187] C. S. Yadav and P. L. Paulose. Upper critical field, lower critical field and critical current density of $FeTe_{0.60}Se_{0.40}$ single crystal. *New J. Phys.*, 11:103046, 2009.

[188] C. Caroli, P. G. de Gennes, and J. Matricon. Bound fermion states on a vortex line in a type II superconductor. *Phys. Lett.*, 9:307, 1964.

[189] T. Hanaguri, K. Kitagawa, K. Matsubayashi, Y. Mazaki, Y. Uwatoko, and H. Takagi. Scanning tunneling microscopy/spectroscopy of vortices in LiFeAs. *Phys. Rev. B*, 85:214505, 2012.

[190] H. F. Hess, R. B. Robinson, and J. V. Waszczak. Vortex-core structure observed with a scanning tunneling microscope. *Phys. Rev. Lett.*, 64:2711, 1990.

[191] A. F. Andreev. Thermal conductivity of the intermediate state of superconductors. *Zh. Eksp. Teor. Fiz.*, 46:1823, 1964.

[192] Y. Tanaka. Distribution of quasiparticles in the S-N-S junction. *Solid State Commun.*, 79:349, 1991.

[193] Y. Tanaka, A. Hasegawa, and H. Takayanagi. Energy spectrum of the quasiparticle in a quantum dot formed by a superconducting pair potential under a magnetic field. *Solid State Commun.*, 85:321, 1993.

[194] F. Gygi and M. Schlüter. Angular band structure of a vortex line in a type-II superconductor. *Phys. Rev. Lett.*, 65:1820, 1990.

[195] F. Gygi and M. Schlüter. Self-consistant electronic structure of a vortex line in a type-II superconductor. *Phys. Rev. B*, 43:7609, 1991.

[196] N. Hayashi, M. Ichioka, and K. Machida. Star-shaped local density of states around vortices in a type-II superconductor. *Phys. Rev. Lett.*, 77:4074, 1996.

[197] N. Hayashi, M. Ichioka, and K. Machida. Effects of gap anisotropy upon the electronic structure around a superconducting vortex. *Phys. Rev. B*, 56:9052, 1997.

[198] Y.-D. Zhu, F. C. Zhang, and M. Sigrist. Electronic structure of a vortex line in a type-II superconductor: Effect of atomic crystal fields. *Phys. Rev. B*, 51:1105, 1995.

[199] Y. X. Ning, C. L. Song, Y. L. Wang, X. Chen, J. F. Jia, Q. K. Xue, and X. C. Ma. Vortex properties of two-dimensional superconducting Pb films. *J. Phys.: Condens. Matter*, 22:065701, 2010.